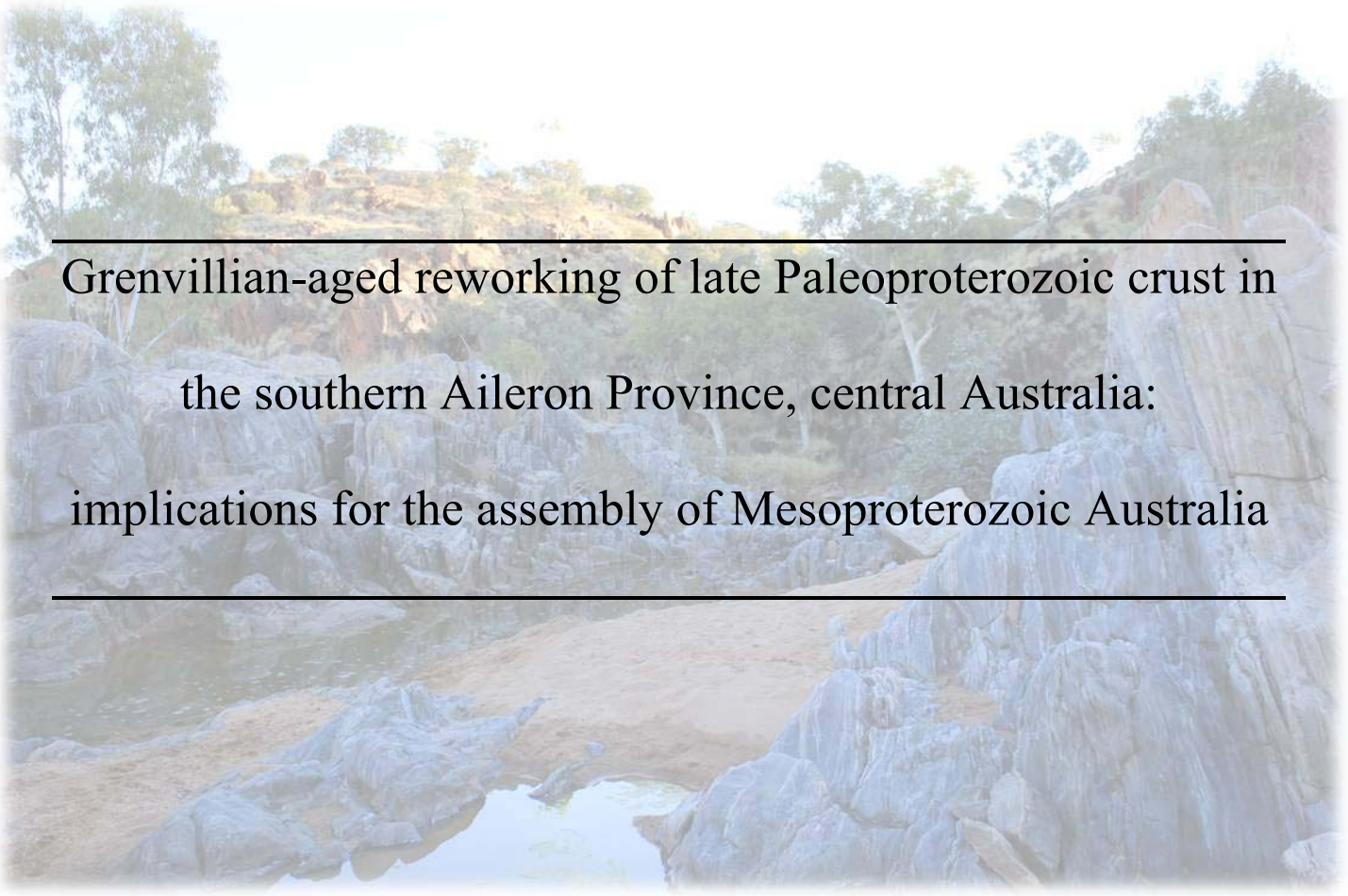

Grenvillian-aged reworking of late Paleoproterozoic crust in the southern Aileron Province, central Australia: implications for the assembly of Mesoproterozoic Australia

Belinda Louise Wong

October 2011

Supervisor: Martin Hand

Centre for Tectonics, Resources and Exploration

School of Earth and Environmental Sciences

The University of Adelaide, South Australia

belinda.wong@student.adelaide.edu.au

TABLE OF CONTENTS

1 ABSTRACT

In situ monazite age dating from granulite facies metapelites along the southern margin of the Aileron Province in the North Australian Craton reveal the presence of a regional-scale Grenvillian (*c.* 1130 Ma) deformation system. Grenvillian-aged deformation has been geochronologically constrained along a strike distance of ~110 km, and includes gneissic rocks within the migmatitic Teapot Complex, which has been previously interpreted to record localised static high-temperature Grenvillian conditions. The Grenvillian ages are identical to recently recognised deformation further south in the southern most Aileron Province and the adjoining eastern Warumpi Province. The deformation produced map-scale E-W trending folds and shear zones, and defines the structural architecture of the interface region between the Aileron and Warumpi Provinces. Folds are generally shallow westerly plunging with deformation associated with partial melting. The structures evolved with time into shear zones and mylonites that record south-side up movement. Phase equlibria modeling on metapelitic assemblages in the central Wigley Block north of Alice Springs indicate that Grenvillian conditions were around 8.5 kbars and 800°C. The development of syn-deformation cordierite-bearing assemblages at the expense of garnet-sillimanite-biotite-bearing associations indicates that decompression accompanied deformation, and is probably a pressure response to the south-up movement recorded in the shear zones. The Grenvillian deformation overprints earlier high-grade metamorphism which occurred at *c.* 1630 Ma, and is recorded by the formation of metamorphic zircon rims in migmatised granitic gneisses, whose protoliths intruded between 1650 and 1630 Ma. The ages of the granites are comparable with those in the Warumpi Province to the south, suggesting that the southern Aileron Province and the Warumpi province may share a magmatic history. This could suggest that the Warumpi Province is not exotic to the North Australian Craton as previously suggested. Metapelites in the Wigley Block also record monazite ages of *c.* 1600 Ma and *c.* 1720 Ma, which could indicate that the Grenvillian event overprinted a complex late Paleoproterozoic metamorphic history. However the complexity in the monazite age data is not easily reconciled with the texturally simple metapelitic assemblages, and potentially these old monazite ages are detrital. Detrital zircons in the metapelites indicate erosion of source regions containing *c.* 1830 Ma and older zircons, but also have a range of concordant ages between *c.* 1590 and 1755 that may represent metamorphically induced partial Pb loss. The Grenvillian deformation belt sits above a lithospheric-scale

structure that that has been imaged dipping southward at ~ 45° to depths of at least 200 km. This feature has previously been interpreted to be a late Paleoproterozoic fossil subduction zone. However the presence of kinematically comparative regional scale Grenvillian deformation in the crust about this feature introduces the possibility that it is a Grenvillian subduction system, with the deformation recording suturing of the North Australian Craton with rocks comprising of the Musgrave Province and the South Australian Craton.

Key words: Grenvillian-aged reworking, Proterozoic Australia, southern Aileron Province, *in situ* monazite geochronology, zircon geochronology, phase equilibra modelling

2 INTRODUCTION

Compared to many other Paleoproterozoic systems, evidence for significant volumes of juvenile crustal addition in Proterozoic Australia is comparatively limited, with felsic rocks generally reflecting variable degrees of recycling (Oliver *et al.* 1991, Wyborn 1992). This has resulted in a significant debate regarding the processes that have shaped Proterozoic Australia, revolving largely around whether its evolution reflects dominantly within-plate (intracratonic) processes (McLaren *et al.* 2005, Oliver *et al.* 1991, Wyborn 1992), or more recently proposed, processes linked to and driven by interactions at hypothesized plate margins (Giles *et al.* 2002, Giles *et al.* 2004, Myers *et al.* 1996, Wade *et al.* 2006). The southern Arunta Region of the North Australian Craton (NAC) is one of the key regions proposed to record the development of a Paleoproterozoic (*c.* 1800-1650 Ma) plate margin (Betts and Giles 2006, Betts *et al.* 2002, Giles *et al.* 2002, Hoatson *et al.* 2005, Maidment *et al.* 2005, Cawood and Korsch 2008), and is therefore a pivotal region in reconciling ideas of Australian Proterozoic crustal growth with Paleoproterozoic tectonic models (Condie 2000, Wade *et al.* 2006).

In many recent tectonic models (eg. Betts *et al.* 2008, Giles *et al.* 2004, Hoatson *et al.* 2005, Maidment *et al.* 2005, Scott *et al.* 2000, Cawood and Korsch 2008), the southern part of the Arunta region in Central Australia is proposed to have been located at or close to an east-west trending, long lived (*c.* 1800-1650 Ma) convergent margin (Betts and Giles 2006, Cawood and Korsch 2008). The southern margin of the NAC can be subdivided into two distinct provinces including the Warumpi and south-eastern Aileron Province (Figure 1, Selway *et al.* 2009, Selway *et al.* 2006). The Warumpi Province is separated from the Aileron Province by a series of E-W trending faults, identified as the surficial expressions of the Central Australian Suture including the Redbank Shear Zone and the Charles River Thrust (Lambeck *et al.* 1988, Scrimgeour *et al.* 2005b, Selway *et al.* 2006, Wright *et al.* 1992). The level of uncertainty regarding the tectonic evolution of central Australia, in particularly the southern Arunta Region has recently been highlighted by Morrissey *et al.* (2011). In that study, *in situ* LA-ICPMS U-Pb monazite geochronology indicates the eastern Warumpi Province has undergone extensive Grenvillian-age (*c.* 1130 Ma) reworking in a region originally thought to be deformed by the *c.* 1590-1570 Ma Chewings Orogeny.

The Wigley Block in the south-eastern Aileron Province (Figure 2), is close to the proposed southern margin of the NAC as well as the apparent junction between the Warumpi Province and Aileron Province (Close *et al.* 2004, Close *et al.* 2003). Thus, its tectonic evolution including timing of sedimentation, age of magmatism, chemistry of magmatism, age of deformation and P-T conditions, should hold important information regarding the tectonic development of the proposed plate margin. However despite the perceived importance of this region in Australian Paleoproterozoic models, relatively little is know about the Wigley Block.

The Wigley Block occupies the area north of the Charles River Thrust and south of the Redbank Shear Zone directly north of Alice Springs (Figure 2), and is interpreted to have been affected by numerous tectonothermal events. The Wigley Block and many other regions in the southern Aileron Province are interpreted to have been reworked by the *c.* 1730-1690 Ma Strangways Orogeny (Shaw *et al.* 1979, Claoué-Long *et al.* 2008), characterised by mid to upper amphibolite facies metamorphism; and the *c.* 1590 Ma Chewings Orogeny (Hand and Buick 2001, Zhao and Bennett 1995), characterised by greenschist to granulite facies, high-T, low-P metamorphism, however conducive data is sparse. The most recent event to affect the Wigley Block is the *c.* 400-300 Ma intracontinental Alice Spring Orogeny. Deformation associated with the Alice Springs orogeny was most intense along the southern margin of the Arunta Region, largely refocusing along older south-vergent thrust faults within the Redbank Shear Zone (Haines *et al.* 2001, Hand and Sandiford 1999, Teyssier 1985)

This study aims to determine the first quantitative constraints on the timing of metamorphism, magmatism and sedimentation in the Wigley Block of the south-eastern Aileron Province. *In situ* U-Pb monazite geochronology was conducted on samples of metapelites to determine the age of metamorphism and deformation. U-Pb zircon geochronology was conducted on igneous rocks to determine the age of magmatism and metamorphism. Metapelites were also used to target detrital zircons to constrain the maximum depositional ages of sedimentary protoliths within the Wigley Block. Lastly, metamorphic constraints were determined though an integration of modelled phase equilibria and diffusion based cooling. The results of this study indicate the dominant structural and metamorphic character of the southern Aileron province is a consequence of *c.* 1130 Ma Grenvillian-aged reworking. Grenvillian-aged deformation overprints an earlier high-grade metamorphic event at *c.* 1630 Ma which is recorded in migmatitic melt veins of granitic protoliths which intruded between 1650 and 1630 Ma.

3 GEOLOGICAL SETTING AND PREVIOUS WORK

3.1 Regional geology

The southern margin of the North Australian Craton is interpreted to preserve a protracted history of interpreted arc related magmatism (Zhao and McCulloch 1995), episodic orogenesis (Collins and Shaw 1995, Scrimgeour *et al.* 2005b) and accretionary tectonism associated with subduction related processes between *c.* 1800-1400 Ma (Betts and Giles 2006, Betts *et al.* 2002, Wade *et al.* 2006, Betts *et al.* 2008, Cawood and Korsch 2008). Numerous authors suggests the assembly of Proterozoic Australia commenced with the collision of the West Australian Craton with the North Australian Craton (*c.* 1790-1700 Ma), subsequent amalgamation of the Gawler Craton with the North Australian Craton (*c.* 1740-1690 Ma), and repeated terrane accretion along the western Gawler Craton and the southern Arunta Inlier (*c.* 1690-1640 Ma) (Betts and Giles 2006, Wade *et al.* 2008b). However, recent models tectonic models propose the West Australian Craton collided with the North Australian Craton during the period c. 1795-1765 Ma (eg. Payne *et al.* 2009).

The Arunta Region exposes approximately 200,000 km^2 of Proterozoic to early Palaeozoic rock (Claoué-Long and Edgoose 2008, Hand and Buick 2001), which preserve an extensive 1500 Myr history of numerous tectonometamorphic events (Wade *et al.* 2008a) between the Stafford Event (*c.* 1810-1800 Ma) to the most recent Alice Springs Orogeny (*c.* 400-300 Ma) (Claoué-Long and Edgoose 2008, Collins and Shaw 1995, Hand and Buick 2001). The Arunta Region has recently been subdivided into three distinct provinces (largely governed by E-W trending faults) as determined by differing protolith ages and tectonometamorphic history (Figure 1, Scrimgeour 2004, Scrimgeour *et al.* 2005b). The Aileron Province is the largest of the three domains and largely possesses rocks with depositional and intrusive ages between 1870-1710 Ma (Claoué-Long *et al.* 2008, Scrimgeour *et al.* 2005b). The Warumpi Province in the south is interpreted to be an exotic terrane with igneous and sediment protolith ages between *c.* 1690-1600 Ma (Scrimgeour *et al.* 2005b). Lastly, the Irindina Province is situated in the east of the region and contains protoliths ranging from Neoproterozoic to Cambrian in age and high-grade Palaeozoic magmatism (Buick *et al.* 2001, Maidment and Hand 2002).

The Wigley Block is located in the southern Aileron Province and occupies the area bounded by a series of east-west trending faults including the Charles River Fault and the Redbank Shear Zone (Figure 2).

Collectively, these faults are interpreted to be the surficial expression of the Central Australia Suture (Close *et al.* 2004, Scrimgeour *et al.* 2005b), a southward dipping crustal scale boundary representing the underthrusting of the North Australia Craton beneath the Warumpi Province (Selway *et al.* 2009, Selway *et al.* 2006), which is thought to have initiated during the ~1640 Ma Liebig Orogeny (Neumann and Fraser 2007, Scrimgeour *et al.* 2005b). The Wigley Block was first defined by Offe and Shaw (1983) based on the recognition of three major lithological groupings termed divisions within the southern Arunta Region. These divisions categorised rock based on their exposure to similar geological processes rather than supergroups in a stratigraphic sense and are interpreted to demonstrate an overall decrease in volcanism and increase in sedimentary reworking up succession (i.e. from divisions 1 to 3, Offe and Shaw 1983). Warren and Shaw (1995) supplemented these divisions and further defined the southern Arunta Region into three major tectonic zones which included the (1) Northern Redbank Thrust Zone characterised by highly mylonitised rock, (2) central Wigley Zone consisting of largely feldspathic migmatitic gneisses and (3) a southern Chewings Zone comprising of metavolcanics overlain by quartzites and schists. Despite extensive geological mapping of the region conducted by the Bureau of Mineral resources (BMR) (Warren and Shaw 1995), excellent outcrop and proximity to Alice Springs, there is little geochronological data and tectonometamorphic evolution information from the Wigley Block.

Although the data is sparse, the Wigley Block is likely to have been affected by numerous tectonothermal events. The earliest event interpreted to have affected Wigley Block and many other regions in the southern Aileron province is the major deformation and high-grade metamorphic *c.* 1730-1690 Ma Strangways Event (Shaw *et al.* 1979, Claoué-Long *et al.* 2008, Maidment *et al.* 2005). The Strangways Event was characterised by lower-amphibolite to granulite facies high-T, low-P metamorphism (Claoué-Long *et al.* 2008, Maidment *et al.* 2005, Shaw *et al.* 1979). It is not clear whether the event was a single Arunta-wide event or a series of short-period, smaller-scale events, which is suggested by multiple structural events involving west to south-west directed thrusting during multiple stages of metamorphism (Collins and Shaw 1995). The Wigley Block lies close to the inferred boundary between the Warumpi Province and the Aileron Province (Figure 1). This boundary is thought to reflect suturing during the 1640 Ma Liebig Orogeny (Scrimgeour *et al.* 2005b). Based on this proximity it seems likely that the Wigley Block should record the effects of the Liebig Orogeny.

The 1590-1570 Ma Chewings Orogeny was a major deformational event, interpreted to have significantly affected the southern Arunta region including the Warumpi Province and the southern Aileron Province as part of a larger scale regional event (Claoué-Long and Edgoose 2008, Rubatto *et al.* 2001, Williams *et al.* 1996, Claoué-Long and Hoatson 2005). However the effects of the Chewings Orogeny in the southern part of the Aileron Province and much of the Warumpi Province are inferred rather than demonstrated. Recent geochronology and phase equilibria modelling conducted by Morrissey *et al.* (2011), shows clear evidence for Grenvillian-aged (*c.* 1130 Ma) reworking within the eastern Warumpi Province adjacent to the Aileron Province, in an area once attributed to *c.* 1590 Ma Chewings Orogeny deformation. U-Pb monazite and Sm-Nd garnet geochronology conducted on metapelites with strong planar and linear fabrics within the Hayes and Iwupataka Metamorphic Complex originally thought to be *c.* 1600 were dated at *c.* 1130 Ma (Morrissey *et al.* 2011). Calculated clockwise P-T evolutions and high geothermal gradients also suggest the Warumpi province was within an extensional regime at *c.* 1130 Ma, which coincides with the later stages of the Musgrave Orogeny in the Musgrave Block further south (Morrissey *et al.* 2011, Wade *et al.* 2008b).

Between 1150-1130 Ma, the Teapot Event thermally reworked the southern Arunta Region through the emplacement of the Teapot Granitoid Complex and associated pegmatites with a subsequent period of migmatisation (Biermeier *et al.* 2003a, Collins and Shaw 1995, Scrimgeour *et al.* 2005b, Shaw and Langworthy 1984, Teyssier *et al.* 1988, Black and Shaw 1995). K-Ar and $^{40}Ar/^{40}Ar$ data from hornblende and micas from the southern Arunta Region suggest the Teapot Event reached temperatures in excess of 500 °C (Biermeier *et al.* 2003a, Shaw *et al.* 1992) and complements the findings of Morrissey *et al.* (2011), placing further emphasis on the regional extent of this tectonothermal event. Shortly following the Teapot Event was the intrusion of the *c.* 1080 Ma doleritic Stuart Dyke Swarm in the southern Arunta Inlier, south of the Redbank Thrust (Collins and Shaw 1995, Zhao and McCulloch 1993). Both the Teapot Event and the intrusion of the Stuart Dykes are contemporaneous with Musgrave aged tectonism and magmatism including the *c.* 1075 Ma Giles Event, however the full extent of Musgrave aged reworking in the southern Arunta still remains unclear (Edgoose *et al.* 2004, Evins *et al.* 2010). The 300-400 Ma Alice Springs Orogeny is the most recent event to have affected the southern Arunta Region, expressed by large scale E-W striking folds and mylonite zones associated with the southward propagation of the Arunta Region and deformation of the

northern fragments of the Centralian Superbasin in a N-S compressional regime (Flöttmann and Hand 1999, Sandiford and Hand 1998, Shaw *et al.* 1992, Teyssier 1985).

3.2 Study area

This study focuses on the central Wigley Block, which is a fault-bounded region between the Charles River Fault and the Redbank Shear Zone in the southern Aileron Province (Figure 2). The region is comprised of an east-west belt of well-exposed Proterozoic crystalline rocks which were subdivided by numerous authors (Offe and Shaw 1983, Warren and Shaw 1995) following the work of Marjoribanks (1975) into three lithologically correlated geological divisions including the Northern Redbank Thrust Zone, central Wigley Block and southern Chewings Zone. The Wigley Block largely consists of quartzofeldspathic migmatitic garnet-biotite gneisses, amphibolites and subordinate aluminous mineral assemblages, and comprises of the early Proterozoic units of the Bond Springs Gneiss, Flint Springs Gneiss, Charles River Gneiss, Randall Peak Metamorphics and unnamed Paleoproterozoic gneisses in the Colyer Creek area (Offe and Shaw 1983, Warren and Shaw 1995). The Bond Springs Gneiss outcrops in the northern-central part of the region and is characterised by leucocratic quartzofeldspathic and garnet-muscovite gneisses with lesser amounts of banded biotite gneisses, amphibolite and muscovite schists (Offe and Shaw 1983). North-northwest of Alice Springs, the Flint Springs Gneiss outcrops as low to moderate height rounded hills and is characterised by abundant porphyroblastic and felsic augen gneisses with minor interrelated amphibolite and garnet-biotite gneisses (Offe and Shaw 1983). The Charles River Gneiss outcrops in the southern part of the region and generally consists of layered quartz-K-feldspar-garnet-biotite-sillimanite gneisses and amphibolite (Offe and Shaw 1983). In the northeast of the region, the Randall Peak Metamorphics outcrop as low hills and ridges comprised of quartzofeldspathic gneisses and amphibolite (Offe and Shaw 1983). Lastly, unnamed Paleoproterozoic gneisses essentially composed of quartz, feldspar ± biotite, garnet, hornblende and muscovite occur as disseminated units throughout the Wigley Block in particularly within the Colyer Creek area and western Wigley Block (Offe and Shaw 1983). The unnamed Paleoproterozoic garnet-biotite gneisses of the central Wigley Block are interpreted to correlate with the adjacent Illyabba Metamorphics unit of the Redbank Thrust Zone (Offe and Shaw 1983, Warren and Shaw 1995). Structurally, the central Wigley Block

is characterised by shallow westerly plunging E-W trending F_1 folds. These folds are overprinted with migmatitic high-strain belts that mechanically involve pervasive south-up mylonite zones coeval with the dominant strike in the region (Figure 3a).

The study also sampled two other regions within the Wigley Block and southern Aileron Province that occur between ~50-110 km to the west and lie within the same structural belt. The first region located approximately 50 km west of the central Wigley Block (Hamilton Creek) structurally demonstrates a kilometre scale low strained megaboudin completely enveloped by an E-W trending high strain fabric within the Redbank Thrust Zone (Figure 3b). The enveloping fabric is comprised of the Illyabba Metamorphics, a largely fault bounded unit in the western Wigley Block which largely consists of migmatitic banded and homogeneous felsic gneisses with small pods of mafic rocks (Warren and Shaw 1995). The boudin is comprised of coarse grained, migmatitic Paleoproterozoic orthogneiss whose protoliths may have intruded the Illyabba Metamorphics (Warren and Shaw 1995). The second region is located approximately 110 km west of the central Wigley Block within the Teapot Complex and is close to the apparent triple junction of the Warumpi Province, Redbank Shear Zone and Charles River Thrust (Figure 1). The Mesoproterozoic Teapot Complex consists of quartzofeldspathic gneiss, ranging from moderately to intensely migmatised in the western outcrops, and a homogeneous granite which may represent an anatectic granitic magma (Warren and Shaw 1995). Zircon U-Pb geochronology conducted on a megacrystic granite near Teapot Yard has dated the Teapot Complex at *c.* 1140 Ma (Black and Shaw 1992).

3.3 Structural description and sample locations

Existing mapping and satellite imagery of the central Wigley Block ~10km due north of Alice Springs, reveals the presence of three distinct structural elements (Figure 3a). The oldest fabric system is parallel to lithological layering and has locally undergone kilometre scale folding with roughly north trending fold axes. These folds have been subsequently overprinted by a pervasive 2km wide E-W trending shear system, producing local dextral displacement (Figure 4c). Within the E-W high strain zone, three generations of mylonite with varying degrees of migmatisation are exhibited. Highly strained migmatitic fabrics with near horizontal westerly plunging mineral lineations are progressively reorientated to a secondary sub vertical

lineation with increased mylonitisation. The second generation of mylonites are partially migmatised and are commonly cross-cut by partial melt veins (Figure 4e), and exhibit south side up kinematics as determined by S-C fabrics (Figure 4b). The system is finally overprinted by a series of pervasive E-W trending fine-grained ultramylonites up to 60m wide with vertical mineral lineations. These ultramylonites provide unequivocal evidence for south side up kinematics through a combination of sigma and delta clasts and S-C fabrics (Figure 4a). Deformation within this E-W trending high strain zone is inferred to be the consequence of a constrained pure shear compressional system, where vertical flattening of the foliation and the development of a lineation are synchronous. E-W trending boudins of partially migmatised mylonite provide evidence for constrained N-S compression within the central Wigley Block (Figure 4d). The central Wigley Block is also structurally characterised by gentle westerly plunging upright E-W trending folds (Figure 3a). These folds are subsequently overprinted by a continuation of the pervasive E-W trending shear system, producing axial planar high strain zones on the steeply dipping limbs of these folds.

Samples used in this study encompass a range of structurally constrained locations widely distributed throughout the Wigley Block and southern Aileron Province in order to provide tight spatial and temporal constraints on tectonometamorphism and deformation within the region. Within the central Wigley Block, numerous samples of migmatitic garnet-biotite-sillimanite metapelites incorporated in granulite facies units, megacrystic augen gneiss, felsic granite and mylonite were selected for analysis. These samples typically possessed sub-vertical foliations with an overall E-W structural trend and low to high angle westerly plunging mineral lineations. Within the Hamilton Creek area, samples were taken from syn-tectonic melt veins from intensely layered migmatites and syn-tectonic pegmatites which envelope migmatitic boudins within the strain shadow of a kilometre scale boudin (Figure 4g). A sample from the southern Aileron Province was taken from an E-W trending garnet-biotite-sillimanite metapelitic layer interleaved within the Teapot Complex and defines the western extent of the study. A summary of the samples used throughout the study, including sample locations and descriptions can be found in Table 1.

4 ANALYTICAL METHODS

4.1 Whole rock and mineral chemistry

A milled representative section of samples was sent to Amdel Mineral Laboratories, Adelaide, to obtain the whole rock chemical composition (Appendix 1). The concentration of major and trace elements were analysed through solution ICP-MS. A subsample was initially fused with lithium metaborate followed by disolution in nitric acid before being presented for ICP-MS analysis (see Payne *et al.* 2010).

Mineral chemistry was obtained through Electron Probe Micro-Analysis (EPMA) in order to determine diffusion cooling histories of garnet-bearing samples. Point mineral compositions were obtained using a Cameca SX51 Electron Microprobe with a beam current of 20nA and an accelerating voltage of 15kV at the University of Adelaide. The X_{Mg} ($Mg/(Mg + Fe^{2+})$) was subsequently calculated for use in diffusion-based cooling models. The mineral chemistry of all samples analysed on the microprobe throughout the study can be found in Table 2. The chemical zoning profiles of garnet obtained through EPMA are shown in Appendix 2.

4.2 Pressure-temperature pseudosections

Phase equilibria techniques were employed to determine the physical P-T conditions of metamorphism in the Wigley Block. A pressure-temperature (P-T) pseudosection was calculated for sample AS2010-65J using the whole rock chemical composition. P-T pseudosections were calculated using the phase equilibria forward modelling program THERMOCALC v 3.33 (October 2009, update of Powell and Holland 1988) in order to graphically represent the stability of mineral assemblages within a given rock composition in P-T space. The internally consistent data set of Holland & Powell (1998; dataset tcds55 November 2003 update) was used for the geologically realistic system NCKFMASHTO (Na_2O-CaO-K_2O-FeO-MgO-Al_2O_3-SiO_2-H_2O-TiO_2-Fe_2O_3).

4.3 Geochronology

4.3.1 U-Pb Monazite LA-ICP-MS geochronology

Samples were selected for U-Pb monazite geochronological analysis based on their mineral assemblage and spatial relationships to defining structures within the region. *In situ* monazite geochronology was conducted on grains in thin section, with the exception of AS2010-64J, where separated monazite grains were mounted in epoxy resin (method outlined in zircon geochronology). Monazite grains were analysed *in situ* from various microstructural locations within thin sections in order to preserve the microstructural context the age data (Kelsey *et al.* 2007, Payne *et al.* 2008). Prior to analysis, all monazite grains were imaged by backscatter electron (BSE) on a Phillips XL30 Scanning Electron Microscope (SEM) in order to identify internal compositional variability and to select homogeneous areas for age determination.

U-Pb isotopic analysis was conducted using a New Wave 213 nm Nd-YAG laser coupled to an Agilent 7500cs ICP-MS at the University of Adelaide. Ablation was performed in a helium atmosphere, with a beam diameter of approximately 15 μm at the sample surface, a repetition rate of 5 Hz and laser intensity of 9-10 J/cm^2. Each analytical run had a total acquisition time of 90 s, comprising 20 s of background measurement, 10 s of laser firing with the shutter closed to allow for beam stabilisation and 60 s of sample ablation. Isotopic masses were measured for 10 ms, 15 ms, 30 ms and 15 ms for ^{204}Pb, ^{206}Pb, ^{207}Pb and ^{238}U respectively. The comprehensive methodology followed for monazite isotopic analysis is outlined in Payne *et al.* (2008).

Raw LA-ICP-MS data was processed using 'GLITTER', a data reduction program developed at Macquarie University, Sydney (Griffin *et al.* 2008). U-Pb fractionation was corrected for using the internal monazite standard MAdel (TIMS normalisation data: 207Pb/206Pb age= 491.0 ± 2.7 Ma; 206Pb/238U age= 518.37 ± 0.99 Ma; 207Pb/235U age= 513.13 ± 0.19 Ma: Payne *et al.* 2008; updated with additional TIMS data), with the exception of AS2010-66D where fractionation was corrected for using the external monazite standard 44069 (TIMS normalisation data: 206Pb/238U = 426 ± 3 Ma: Aleinikoff *et al.* 2006). The accuracy of data correction was monitored by repeated analysis of the in-house monazite standard 94-222/Bruna NW (*c.* 450 Ma) (Payne *et al.* 2008), with the exception of AS2010-66D where data accuracy was monitored by the internal monazite standard MAdel. Signals were examined carefully for anomalous portions of signal related to zones of Pb loss or gain and the best portion of each ablation signal was selected for age and error

determination. Common lead (^{204}Pb) was not corrected for during data reduction, however analyses were discarded if common lead levels rose to levels high enough to compromise the integrity of the output age. Throughout the study, the weighted averages obtained for MAdel are ^{207}Pb/^{206}Pb= 487.9 ± 4.6 Ma (n=122, MSWD=0.62), ^{206}Pb/^{238}U= 517.3 ± 1.4 Ma (n=122, MSWD=0.89) and ^{207}Pb/^{235}Pb= 511.8 ± 1.2 Ma (n=122, MSWD=0.90), 222 are ^{207}Pb/^{206}Pb= 475 ± 16 Ma (n=24, MSWD=2.3), ^{206}Pb/^{238}U= 447.9 ± 3.5 Ma (n=24, MSWD=1.5) and ^{207}Pb/^{235}Pb= 453.2 ± 3.1 Ma (n=24, MSWD=1.5) and 44069 are ^{207}Pb/^{206}Pb= 418 ± 14 Ma (n=25, MSWD=1.4), ^{206}Pb/^{238}U= 424.4 ± 2.4 Ma (n=25, MSWD=1.02) and ^{207}Pb/^{235}Pb= 423.5 ± 3.7 Ma (n=25, MSWD=2.4).

4.3.2 U-Pb zircon LA-ICP-MS geochronology

Zircon geochronology was used to constrain igneous and metamorphic events and to constrain the maximum depositional age of metasediments. A provenance study was not included due to time constraints. Zircons were extracted from whole rock samples of approximately 2 kg using a crusher, tungsten carbide mill and conventional magnetic and heavy liquid separation techniques. Individual zircons were then hand picked, mounted in 2.5 cm diameter circular epoxy grain mounts and hand polished until the centre of the zircons were revealed. Prior to LA-ICP-MS analysis, all zircon grains were imaged by backscatter electron (BSE) and cathodoluminescence (CL) on a Phillips XL20 Scanning Electron Microscope (SEM) in order to study their internal structural, determine if multiple age components were present and to select homogeneous areas for age determination.

U-Pb isotopic analyses of zircons were obtained using a similar methodology to monazite geochronology. Laser ablation was performed with a beam diameter of approximately 30 μm at the sample surface, a repetition rate of 5 Hz and laser intensity of 9-10 J/cm^2. Each analysis consisted of a total acquisition time of 100 s, comprising 20 s of background measurement, 10 s of laser firing with the shutter closed to allow for beam stabilisation and 70 s of sample ablation. Isotope masses were measured for 10 ms, 15 ms, 30 ms, 10 ms, 10 ms and 15 ms for ^{204}Pb, ^{206}Pb, ^{207}Pb, ^{208}Pb, ^{232}Th and ^{238}U respectively.

U-Pb fractionation was corrected for using the external zircon standard GJ (TIMS normalisation data: 207Pb/206Pb age= 607.7 ± 4.3 Ma; 206Pb/238U age= 600.7 ± 1.1 Ma; 207Pb/235U age= 602.0 ± 1.0 Ma: Jackson *et al.* 2004). The accuracy of data correction was monitored by repeated analysis of the internal zircon

standard Plešovice (ID-TIMS normalisation data: 207Pb/206Pb age= 337.13 ± 0.37 Ma: Sláma *et al.* 2008). Raw data was reduced using 'GLITTER' and common lead was not corrected for as outlined above. Throughout the study, the weighted averages obtained for GJ are $^{207}Pb/^{206}Pb$= 608.3 ± 3.6 Ma (n=236, MSWD=0.39), $^{206}Pb/^{238}U$= 601.1 ± 1.8 Ma (n=236, MSWD=3.4) and $^{207}Pb/^{235}Pb$= 602.7 ± 1.6 Ma (n=236, MSWD=3.4) and Plešovice are $^{207}Pb/^{206}Pb$= 344.8 ± 8.5 Ma (n=40, MSWD=0.87), $^{206}Pb/^{238}U$= 334.5 ± 1.8 Ma (n=40, MSWD=1.8) and $^{207}Pb/^{235}Pb$= 335.7 ± 1.8 Ma (n=40, MSWD=2.0).

Reduced monazite and zircon data was then exported into excel where subsequent conventional concordia and weighted average plots were generated using Isoplot v4.11 (Ludwig 2003). Ages quoted throughout the study are $^{207}Pb/^{206}Pb$ ages as the data contains ages older than *c.* 1000 Ma and all errors stated in data tables and along side concordia diagrams are at the 1σ level. Concordancy was calculated using the ratio of $^{206}Pb/^{238}U$ / $^{207}Pb/^{206}Pb$. All geochronological data acquired throughout the study can be found in Appendix 3 and 4.

4.1 Temperature-time modelling

Temperature-time models were constructed using the diffusion code THERMAL HISTORY (Robl *et al.* 2007) to describe the diffusive zoning that arises from the binary Fe-Mg exchange between garnet and biotite during cooling from peak metamorphic conditions. The model determines the cooling history of a single garnet grain by solving the Arrhenius equation of diffusivity ($D=D_0e^{-Q/RT(t)}$) through the input of parameters for Fe-Mg exchange within that particular system. The diffusivity constants constrained by Ganguly *et al*. (1998) that represent a typical garnet-biotite couple in an upper amphibolite or granulite facies rock were used to model the Fe-Mg exchange between garnet and biotite. The extent of Fe-Mg re-equilibration is highly dependent on both the temperature and rate of cooling, thus variations in temperature and the radius of each grain strongly influences the internal composition of garnet (Hauzenberger *et al.* 2005, Robl *et al.* 2007). For the modelling of diffusion profiles in garnet outlined by Robl et al. 2007, the following assumptions must be made: (a) garnet crystals are spherical and completely surrounded by an infinite reservoir of biotite, thus the two are in chemical equilibrium, (b) the system is only expressed through the diffusion of Fe and Mg (c) garnet crystals hold no record of previous zoning at the peak temperature, (d) the amount of garnet and biotite and the size of each garnet crystal remains constant throughout the cooling history and (e) diffusion within

biotite is infinitely fast thus chemical zoning within biotite is not observed (Dodson 1986, Hauzenberger *et al.* 2005, Robl *et al.* 2007). Samples were selected for temperature time analysis based on garnet being in direct contact with coarse and/or abundant biotite and the obtained EPMA chemical zoning profile. Eight traverses through the centre of the grains were conducted on garnets from two samples. Garnet traverses which showed no evidence of resorption and possessed relatively flay lying cores and constant downward inflections of X(Mg) towards the outer rim were favoured.

5 RESULTS

5.1 Metamorphic Petrology

Samples selected for metamorphic petrography encompass a range of locations widely distributed throughout the southern Aileron Province. In the central Wigley Block, samples were selected from the Charles River Gneiss and unnamed Paleoproterozoic gneisses. Samples of migmatised garnet-sillimanite metapelite and mylonite located within unnamed Paleoproterozoic Gneisses are located within the structurally younger E-W trending regional fabric. Samples of migmatised garnet-sillimanite-biotite metapelite from the Charles River Gneiss are typically located within an older fabric that trends into the E-W high strain zone. In the southern Aileron province, a sample was taken from a gently folded metapelite with a shallow westerly plunging mineral lineation, interleaved within the Teapot Complex.

5.1.1 Garnet-sillimanite bearing pelites

These are garnet porphyroblastic rocks which contain a strongly developed foliation defined by biotite and sillimanite that occurs within a matrix that contains variable amounts of microcline and quartz with subordinate plagioclase.

Sample AS2010-65J: Location 0385454 7389461

Porphyroblastic garnet-biotite-sillimanite-bearing gneiss

Garnet forms grains that range in size from 1-9 mm, although predominately 3-7 mm, and contain inclusions of biotite-sillimanite-quartz (Figure 5a). In general the inclusions are unoriented or weakly oriented, but on occasion form well defined inclusion fabrics that parallel the fabric in the matrix (in the 2D plane of the thin section). The rims of garnet may also contain large inclusions of monazite (~250 μm). The foliation is defined by biotite and sillimanite which forms a domainal fabric that is interlayered with domains dominated by quartz and plagioclase, with lesser microcline. The domainal fabric layers are typically 3-5 mm wide, with elongate quartz up to 3 by 1 mm and plagioclase and microcline < 1 mm. Quartz and feldspar show undulose

extinction. Sillimanite occurs in bundles defined by aggregates of elongate fine-grained prismatic sillimanite. Sillimanite also occurs as inclusions in plagioclase and quartz. Both sillimanite and garnet are overprinted by a well developed fracture fabric that is orthogonal to the foliation (in 2D), and approximately orthogonal to the lineation in hand sample. When these fractures occur in sillimanite that is included in plagioclase and quartz, the fractures terminate in the quartz and plagioclase host (Figure 5b), with occasional fine-grained trails of opaques in the quartz-plagioclase matrix that mark the former continuation of the fracture. These annealed fractures suggest the extension of the sillimanite aggregates was associated with the deformation recorded by the fabric and its associated lineation. Biotite tends to be more strongly concentrated around garnet with typically larger crystals forming in strain shadows on garnet (Figure 5a).

Sample AS2010 -66D: Location 0382933 7386196

Intensely foliated garnet-sillimanite-biotite-bearing gneiss

Garnet occurs as grains up to 4 mm diameter that have occasional inclusions of biotite and sillimanite. The fabric is deformed by intensely aligned bundles of sillimanite comprising of fine-grained aggregates of prismatic sillimanite. In places sillimanite forms densely intergrown aggregates with biotite. Where this happens, sillimanite grains sometimes become coarsely prismatic (Figure 5c). The matrix of the assemblage is dominated by quartz which forms strongly undulose grains whose internal sub-grains form a well developed fabric that lies approximately 30 degrees from the bulk sillimanite-biotite fabric. The matrix also contains layers comprising of coarse-grained (up to 1.5 mm) microcline. In comparison with the quartz, the microcline shows much less sub-grain development.

Sample AS2010-67A2: Location 0383662 7386185

Coarse-grained garnet rich biotite-sillimanite-bearing gneiss

Garnet grains up to 11 mm diameter form around 25% of the assemblage and contains inclusions of biotite and mats of sillimanite, together with plagioclase, microcline and minor quartz. In some garnets, sillimanite is oriented defining an internal foliation that is generally oblique the external fabric (Figure 5d). The external

foliation is dominated by coarse-grained biotite which encloses the garnet. In places, dense mats of sillimanite are intergrown with biotite. Parallel to the foliation are layers dominated by coarse-grained microcline and quartz. These domains contain occasional large monazite grains.

Sample RED2011-01: Location 0275184 7397376

Garnet-biotite-sillimanite-bearing gneiss

Garnet forms irregular shaped grains up to 7 mm in diameter. The garnets are inclusion free and are enclosed in a quartz dominated matrix with grains up to 6 mm in diameter. The matrix also contains subordinate microcline up to 1 mm. The foliation is deformed by biotite and sillimanite which envelopes the garnet and large grains of quartz. Sillimanite occurs both in dense aggregates of fine-grain prismatic sillimanite crystals, as well as intergrown with biotite. In places the fabric wraps texturally early biotite grains. Some of the sillimanite and biotite exhibit well developed microboudinage with the interboudin necks filled with fine-grained ilmenite (Figure 5e). The sample contains abundant monazite throughout the matrix.

5.1.2 Garnet-sillimanite-cordierite bearing pelites

A variation in the metapelitic compositions is represented by cordierite-bearing assemblages.

Sample AS2010-63D: Location 0380898 7387482

Garnet-cordierite-sillimanite-biotite-bearing gneiss

Garnet forms grains between 2-11 mm in diameter, with the larger grains being comparatively sparse. Garnet contains rounded inclusions of biotite, sillimanite and quartz. The matrix comprises large grains (up to 15 by 6 mm) of partially pinitised cordierite that are distinctly elongate parallel to the foliation which is defined by prismatic sillimanite and lesser biotite. Cordierite contains inclusions of sillimanite, biotite and microcline; however sillimanite and microcline dominate the inclusion assemblage, suggesting that cordierite growth locally depleted the abundance of biotite (Figure 5f). Cordierite also contains rounded inclusions of garnet,

suggesting that it postdates garnet. Microcline forms an abundant mineral in the matrix together with minor quartz.

Sample AS09-4: Location: 0383255 7388323

A variation on the two assemblages described above is a garnet-biotite-sillimanite-bearing assemblage that contains intensely foliated biotite and sillimanite domains that form part of a layered composite fabric with granoblastic K-feldspar, plagioclase and quartz. The composite fabric encloses coarse-grained garnet that occurs in clusters with K-feldspar and quartz along the fabric. These clusters are suggestive of migmatitic segregations. Garnet contains inclusions of biotite, sillimanite, quartz and plagioclase, and where it was in contact with the biotite-sillimanite-bearing foliation domains is now separated from biotite and sillimanite by well developed coronae of cordierite. These coronae also contain K-feldspar and locally large monazite grains that are conspicuously coarser-grained than monazite elsewhere in the matrix (Figure 5g). The textural setting of the cordierite suggests that it formed via reaction between garnet, sillimanite and biotite. The foliation also envelopes the cordierite domains, suggesting that cordierite formation was in part synchronous with deformation.

5.1.3 Mylonites

Sample AS2010-72D: Location 0385790 7388832

Mylonite with rounded porphyroclasts of microcline and plagioclase up to 9 mm in diameter are enclosed by an intense fine-grained fabric comprising of dynamically recrystallised quartz ribbons and thin layers of biotite (Figure 5h). The porphyroclasts have been recrystallised around their margins to fine-grained granoblastic aggregates as well as delta and sigma style clasts with elongate tails. Many of the porphyroclasts show only limited undulose extinction despite the intensity of the mylonitic fabric. The abundance of microcline and plagioclase porphyroclasts suggests the mylonite was derived from a granitic precursor, consistent with the field relationships in which the mylonites cross cut felsic orthogneiss.

5.2 Mineral Chemistry

Sample AS2010-65J

Core and rim compositions were obtained from two garnet grains in sample AS2010-65J. X_{alm} values slightly decrease from rim to core (0.833-0.772). X_{py} values increase from 0.092 in the rim to 0.175 in the core of the grain. X_{spss} values increased slightly from the core towards the rim, with values typically ranging between 0.025 and 0.038 respectively. A small variation in X_{grs} is observed ranging between 0.043 in the core to 0.038 in the rim.

Sample AS2010-66D

Six traverses conducted on 5 garnet grains in sample AS2010-66D demonstrate very similar zoning patterns with X_{alm} values gradually decreasing from rim to core (0.808 – 0.725). X_{py} values gradually increase from 0.084 in the rim to 0.208 in the core of the grain. X_{grs} values vary slightly throughout the traverse and demonstrate no distinct zoning pattern. Values ranged between 0.023 and 0.049, with a slight increase in calcium towards the outer rim of the grains. X_{spss} values increased slightly from the core towards the rim, with values ranging between 0.027 and 0.084 respectively. Biotite grains analysed throughout sample AS2010-66D had X_{mg} values typically ranging between 0.442 and 0.539, TiO_2 content between 1.59 and 4.49 wt% and Al_2O_3 content between 16.29 and 20.44.

Sample AS2010-67A2

Three traverses conducted on 3 garnet grains in sample AS2010-67A2 show a gradual decrease in X_{alm} values from 0.843 at the rim to 0.741 in the core of the grain. X_{py} values gradually increase from the rim to the core of the grain, with values between 0.093 and 0.214 respectively. X_{grs} values vary slightly throughout the traverse and demonstrate no distinct zoning pattern with values ranging between 0.024 and 0.032. X_{spss} values decreased slightly from 0.017 at the rim to 0.039 in the core of the grain. Biotite grains analysed throughout sample AS2010-67A2 typically had a TiO_2 content between 1.75 and 5.11 wt%, Al_2O_3 content between 16.88

and 19.63, and X_{mg} values ranging between 0.297 and 0.452. Plagioclase grains have X_{Na} values ranging between 0.732 to 0.971 and X_{Ca} values between 0.027 and 0.266.

5.3 Pressure-temperature conditions and diffusion-based cooling history

In order to constrain the physical conditions of metamorphism, a P-T pseudosection was calculated for the metapelitic sample AS2010-65J (Figure 6) using the bulk composition obtained from Amdel Laboratories. The interpreted peak mineral assemblage (garnet + biotite + sillimanite + liquid + K-feldspar + plagioclase + ilmenite + quartz) defines a field with P-T conditions between approximately 775-830 °C and 6-10 kbars. Calcium isopleths constructed in the peak field demonstrate garnet decreases in X_{Ca} down pressure from 0.05 to 0.025. Modal proportions of garnet within the sample field decrease down temperature from 0.225 to 0.125. The absence of microstructural mineral relationships means a P-T path was unable to be defined for this sample (Vernon 1996). However, one possibility to explain this in an evolutionary way is if the rocks followed a strongly decompressive path within the peak field. A diffusion-based cooling profile was calculated for a small garnet from a nearby sample (AS2010-66D) using an X_{Mg} value of 0.448 for biotite and a radius of 403.1 μm for garnet. The closure temperature of the core analysis indicates X_{Mg} diffusion ceased in the core at approximately 780 °C (Figure 7). This is consistent with the predictions of the temperature constraints based on the P-T pseudosection

5.4 Geochronology

In situ monazite LA-ICP-MS geochronology was conducted on 7 samples with the exception of AS2010-66J where a monazite mount was used. Zircon LA-ICP-MS geochronology was conducted on 6 samples mounted in epoxy resin. A summary of monazite and zircon geochronology obtained throughout the study, including calculated ages and interpretations can be found in Table 3.

5.4.1 U-Pb Monazite LA-ICP-MS geochronology

Sample AS2010-63D (Figure 3a, N-S trending fabric)

Twenty-three analyses were conducted on 14 monazite grains located within the matrix and fabric. Monazite grains were typically found within or along the grain boundaries of biotite, with no monazites found within garnet grains. Grains analysed ranged in length between approximately 30-60 μm and do not exhibit zoning under BSE imaging (Figure 8b). The grains were euhedral with round or elongate shapes, parallel to the fabric. Of the 23 analyses, 1 analysis was rejected outright due to a high level of common Pb present throughout the signal (79 counts per second). Two distinct age populations are present in AS2010-63D (Figure 8a), with monazite grains analysed within the earlier garnet-bearing assemblage typically preserving older ages than the overprinting cordierite-bearing assemblage. The old age population has an older discordant population with a $^{207}Pb/^{206}Pb$ isotopic age of 1638 ± 19 Ma and an upper intercept of 1763 ± 31 Ma (MSWD=1.7). The young monazite age population has a $^{207}Pb/^{206}Pb$ weighted average isotopic age of 1090 ± 15 Ma (n=7, MSWD=0.69) with concordancy ranging from 97-101%. Monazite grains from the younger population were typically smaller.

Sample AS2010-65J (Figure 3a, E-W trending fabric)

Thirty analyses were conducted on 17 individual monazite grains located within the matrix and fabric. Monazite grains were typically found along the grain boundaries of biotite and garnet, with a few grains found within garnet and quartz. Grains analysed were typically rounded, euhedral and elongated parallel to the fabric, with a small monazite population exhibiting anhedral cracked and angular shapes (Figure 8d). Grains ranged in size between 20- 240 μm long and did not exhibit zoning under BSE imaging. Of the 30 analyses collected, 6 were rejected outright on the basis of noisy time-resolved signals and high levels of common Pb. An additional 6 analyses with >10% discordance were excluded from age calculations. Using the 'unmix' algorithm of Sambridge and Compston (1994), two age populations were identified in sample AS2010-65J. The older population ($^{207}Pb/^{206}Pb$ = 1187 ± 17 Ma (n=6, MSWD=0.71) was yielded by typically discordant analyses and were excluded from further age calculations. The sample has a $^{207}Pb/^{206}Pb$ weighted average isotopic age of 1128 ± 12 Ma (n=12, MSWD=1.03) with concordancy ranging between 94-103% (Figure 8c). There is no apparent correlation between the two age populations and the textural location of monazite grains analysed.

Sample AS2010-66D (Figure 3a, NE-SW trending fabric)

Forty-five analyses were conducted on 27 individual monazite grains within the matrix and fabric. Monazite grains were located along the grain boundaries of biotite and garnet however no monazites were found within these minerals. Grains analysed ranged in length between approximately 20-250 μm and showed no zoning in BSE imaging. Monazite grains were typically rounded or elongate parallel to the fabric, with occasional anhedral fractured grains (Figure 8f). Of the 45 analyses, two were rejected outright on the basis of noisy time-resolved signals. Two distinct age populations are present in AS2010-66D (Figure 8e), with monazite grains analysed within garnet and the matrix preserving older ages than those along the grain boundaries of biotite and within the foliated matrix. The old monazite age population has a $^{207}Pb/^{206}Pb$ weighted average isotopic age of 1720 ± 17 Ma (n=10, MSWD=1.6) with concordancy ranging from 97-102%. The young monazite age population has a $^{207}Pb/^{235}U$ weighted average isotopic age of 1100.9 ± 8.0 Ma (n=22, MSWD=1.4), with concordancy ranging between 96-110%. The $^{207}Pb/^{235}U$ weighted average age was used in this instance because the ratio is less sensitive to reversely discordant monazite. Monazite grains from the young population were typically smaller.

Sample AS2010-66J (Figure 3a, E-W trending fabric)

Forty-two analyses were conducted on 31 individual monazite grains mounted in epoxy resin; hence the microstructural location of these grains is unknown. Grains analysed were typically anhedral, cracked and fractured with blocky angular shapes and ranged in length between approximately 50-400 μm. Some grains exhibited zoning in BSE imaging, with dark domains forming around the rims and within microfractures of the grains (Figure 9b). Initial analyses of these domains provided noisy and largely discordant ages therefore were avoided during further analysis. Of the 42 analyses, 13 were rejected outright on the basis of high levels of common Pb (above 24 counts per second) and noisy time-resolved signals and an additional 3 analyses with >10% discordance were excluded from age calculations. Of the 29 analyses, a further 3 analyses defining an older discordant age population ($^{207}Pb/^{206}Pb$ age= 1176 ± 25 Ma (MSDW=0.51)) were rejected from age calculations using the unmix algorithm (Figure 9a, Sambridge and Compston 1994). Sample AS2010-66J has

a $^{207}Pb/^{206}Pb$ weighted average isotopic age of 1116.3 ± 8.2 Ma (n=26, MSWD=0.55) with concordancy ranging between 92-101%.

Sample AS2010-67A2 (Figure 3a, NE-SW trending fabric)

Twenty-seven analyses were conducted on 10 monazite grains within the matrix and fabric. Monazite grains were located along grain boundaries, microfractures and commonly within biotite grains. Grains analysed ranged in length between approximately 60-120 μm and did not appear to be zoned in BSE imaging (Figure 9d). Monazite grains were typically euhedral with rounded or elongate shapes, parallel to the fabric. Of the 27 analyses, 3 were rejected outright due to noisy time-resolved signals. Two distinct age populations are present within AS2010-67A2 (Figure 9c), with monazite grains analysed along the grain boundaries of biotite and garnet typically preserving older ages than those analysed within biotite and garnet. The older monazite population had a $^{207}Pb/^{206}Pb$ weighted average isotopic age of 1565 ± 20 Ma (n=12, MSWD=2.5) with concordance of 99 and 100%. The young monazite age population has a $^{207}Pb/^{206}Pb$ weighted average isotopic age of 1127 ± 20 Ma (n=9, MSWD=1.19) with concordancy ranging from 99-102%.

Sample AS2010-72D (Figure 3a, E-W trending fabric)

Forty-one analyses were conducted on 21 monazite grains located along grain boundaries within the mylonitic fabric. Monazite grains were typically euhedral to subhedral and possessed spherical shapes with milled disseminated rims under BSE imaging (Figure 9f). Grains ranged in diameter between 50-120 μm and did not appear to be zoned in BSE imaging. Of the 41 analyses, 13 were rejected outright on the basis of noisy isotopic ratios and high levels of common Pb (above 18 counts per second). A concordia plot calculated for AS2010-72D produces a single age population (Figure 9e). The sample has a $^{207}Pb/^{206}Pb$ weighted average isotopic age of 1129.4 ± 7.9 Ma (n=28, MSWD=0.99) with concordancy ranging from 92-104%.

Sample RED2011-01 (Figure 1)

Twenty analyses were conducted on 11 individual monazite grains within the fabric. Monazite grains were typically found along the grain boundaries of biotite, with a few grains found within biotite. Grains analysed from sample RED2011-01 were typically euhedral with rounded or elongate shapes, parallel to the fabric and ranged in length between 40-80 μm and did not appear to be zoned in BSE imaging (Figure 9a). Of the 20 analyses, 1 analysis was rejected due to a noisy time-resolve signal. A concordia plot calculated for RED2011-01 displays a single concordant age population (Figure 10a). The sample has a $^{207}Pb/^{206}Pb$ weighted average isotopic age of 1141.9 ± 9.9 Ma (n=19, MSWD=0.69) with concordancy ranging from 96-104%.

5.4.2 U-Pb zircon LA-ICP-MS geochronology

Sample AS2010-64J (Figure 3a, E-W trending fabric)

In transmitted light (TL), zircons from sample AS2010-64J were typically elongate, euhedral to subhedral and translucent pale pink to dark brown crystals. Zircon grains were generally 90-290 μm long with aspect ratios of 1:3, with the larger dark down grain population (approximately 30%) reaching proportions of up to 500 x 200 μm. Zircon crystals were commonly fractured, with microfracture density increasing towards the centre of larger grains. Inclusions of sillimanite needles were also observed in larger dark brown crystals. Under CL, the vast majority of grains exhibit weakly luminescent, well-defined concentric oscillatory zoning (Figure10d), with a smaller population exhibiting weakly luminescent featureless domain zoning. Up to 50% of grains exhibit weakly luminescent convoluted metamorphic cores and 10 % had very weakly luminescent metamict cores which were avoided during analysis. Sixty-two analyses were conducted on 59 individual zircon grains. Of the 62 analyses collected, 14 were rejected outright on the basis of excessive discordance (>10%), noisy isotopic ratios and high levels of common Pb (above 30 counts per second). Two age populations are present in this sample (Figure 10c), with zircons exhibiting concentric oscillatory and sector zoning preserving older ages than convoluted and 'ghost' zoned grains. The older population has a $^{207}Pb/^{206}Pb$ weighted average isotopic age of 1649.7 ± 6.7 Ma (n=32, MSWD=0.85) with concordancy ranging from 93-103%. The younger population has a $^{207}Pb/^{206}Pb$ weighted average isotopic age of 1637 ± 13 Ma (n=16, MSWD=1.4) with concordancy ranging from 96-98%.

Sample COL2011-01 (Figure 3a, E-W trending fabric)

Sixty analyses were conducted on 56 individual zircon grains. Zircons from sample COL2011-01 were largely elongate, euhedral to subhedral grains with rounded edges. Crystals ranged in length between approximately 60-260 μm with aspect ratios of 1:3. Zircon grains were occasionally fractured, with microfracture density increasing towards the centre of larger metamict grains. Under CL, the vast majority of grains exhibit moderately to weakly luminescent, moderately defined concentric oscillatory zoning (Figure 10f). A smaller population (approximately 35%) exhibit weakly luminescent featureless domain zoning with highly luminescent metamorphic overgrowths around the rim. Weakly luminescent metamict cores were avoided during analysis. Of the 60 analyses, 22 were rejected outright on the basis of noisy isotopic signals and high levels of common Pb (above 30 counts per second). A concordia plot calculated for COL2011-01 (Figure 10e) displays a single concordant age population. The sample has a calculated $^{207}Pb/^{206}Pb$ weighted average of 1636.8 ± 6.5 Ma (n=38, MSWD=0.86) with concordancy ranging from 98-101%. Analyses were not subdivided into cores and rims as there were not enough analyses of cores to provide a definitive age outside of uncertainty.

Sample HAM2011-02 (Figure 1, 2 and 3b, NW-SE trending fabric in the strain shadow of a boudin)

Forty-nine analyses were conducted on 31 individual zircon grains. Zircons from sample HAM2011-02 were elongate and highly euhedral with angular edges. Crystals ranged in length between 0.4-1.7 mm (Figure 11b) with aspect ratios of 1:4. Zircon grains were occasional internally fractured. Under CL, the vast majority of grains exhibited weakly luminescent weakly to moderate defined oscillatory and sector zoning of the rims and moderately luminescent chaotic internal zoning. Most grains possessed weakly luminescent metamict cores and metamorphic overgrowths on the rims and were avoided during analysis. Of the 49 analyses, 16 were rejected outright due to high levels of common Pb (above 30 counts per second) and noisy isotopic ratio signals. Of the 33 analyses, a further 4 analyses defining an older discordant age population identified using the ‘unmix’ algorithm of (Sambridge & Compston (1994) were rejected. A Concordia plot of HAM2011-02 (Figure 11a) produces a single age population with a $^{207}Pb/^{206}Pb$ weighted average isotopic age of 1137.4 ± 8.1 Ma (n=29, MSWD=1.2) with concordancy ranging between 96-104%.

Sample HAM2011-08 (Figure 3b, E-W trending fabric)

Fifty analyses were conducted on 48 individual zircon grains. Crystals were generally 80-300 μm long with aspect ratios of 1:3. A few larger grains were present reaching proportions of up to 480 x 180 μm. Under CL, two distinct populations of zircons were present for sample HAM2011-08. The first population encompassed ~90% of all zircons and was defined by largely subhedral crystals with rounded edges. The zircon grains typically exhibited highly luminescent strong oscillatory zoning with a smaller proportion of zircons exhibiting highly luminescent domain zoning, particularly within the centre of grains. The remaining population was defined by euhedral angular zircons. Zircon grains in this population typically exhibited weakly luminescent oscillatory zoning of the rims and weakly luminescent chaotic metamict cores (Figure 11d). Throughout analysis, chaotic metamict cores and metamorphic over growths around the rim of crystals were avoided. Of the 50 analyses, 14 were rejected outright on the basis of noisy time-resolved signals and high levels of common Pb (above 40 counts per second). An additional 2 analyses with >8% discordance were excluded from age calculations. Two distinct age populations are present in HAM2011-08, with zircons analysed from the larger highly luminescent oscillatory-zoned zircon population preserving older ages than the smaller weakly luminescent-zoned grains. The old age population has a $^{207}Pb/^{206}Pb$ weighted average isotopic age of 1626.2 ± 7.2 Ma (n=28, MSWD=0.50) and concordances ranging from 95-102%. The young age population has a $^{207}Pb/^{206}Pb$ weighted average isotopic age of 1139 ± 19 Ma (n=4, MSWD=1.11) and concordances ranging from 97-101%.

5.4.3 U-Pb detrital zircon LA-ICP-MS geochronology

Sample AS2010-62D (Figure 3a, N-S trending fabric)

Detrital zircon from sample AS2010-62D are typically stubby to elongate, euhedral to subhedral and translucent pale pink to dark brown crystals with well-defined rounded edges. Zircon grains were generally 80-130 μm long, with the larger translucent brown grain population (approximately 35%) reaching proportions of up to 342 x 120 μm. The smaller zircon population was typically more rounded and 10% of

these grains appear to have a hexagonal 'soccer ball' form (Figure 12c). As a whole, the detrital zircon grains exhibit surficial pitting and mechanical abrasion consistent with transportation, deposition and prolonged weathering. Under CL, the vast majority of grains exhibit weakly luminescent well-defined concentric oscillatory zoning with a smaller population exhibiting highly luminescent featureless domain zoning. Some grains exhibited transgressive metamorphic overgrowths (Figure 12c). Weakly luminescent metamict cores were avoided during analysis.

Eighty-five analyses were conducted on eighty-three individual zircon grains from sample AS2010-62D. Of the 85 analyses collected, 10 were rejected outright on the basis of noisy time-resolved signals and high levels of common Pb. Within the youngest spread of ages, two prominent peaks emerge at *c.* 1825 Ma and 1950 Ma from largely oscillatory zoned and highly luminescent domain zoned grains. The $^{207}Pb/^{206}Pb$ weighted average age of the first prominent population is 1835 ± 15 Ma (n=23, MSWD=3.1). The first and second youngest concordant oscillatory zoned grains within the sample have $^{207}Pb/^{206}Pb$ ages of 1804.3 ± 20 Ma and 1815.3 ± 18 Ma with concordances of 97 and 98 % respectively. The youngest cluster of detrital zircons within this sample range in age between *c.*1590 Ma and 1755 Ma with concordancy between 92 to 98% and exhibit blurry and convoluted zoning. A broad range of age data between *c.* 2280-2850 Ma is also apparent, with minor peaks in the age spectra at *c.* 2750 Ma, 2470 Ma and 2290 Ma emerging from highly luminescent domain zoned zircons and oscillatory zoned zircons.

Sample AS2010-59J (Figure 3a, E-W trending fabric)

Detrital zircon from sample AS2010-59J display euhedral to subhedral, stubby to slightly elongate and translucent pale pink to dark brown crystal morphologies. Zircon grains were generally 80-160 μm long, with the larger brown translucent grain population (approximately 35%) up to 200 μm long with length to width aspect ratios of approximately 2:1. Approximately half of zircon crystals are fractured, with microfracture density increasing towards the centre of the grains for brown crystals in particular. The smaller-sized zircon population was typically more rounded and 5% of these grains appear to have a textured hexagonal 'soccer ball' surface. Similarly to AS2010-62D, the detrital zircon population exhibits surficial pitting and mechanical abrasion. Under CL, grains typically exhibit weakly to highly luminescent oscillatory zoning and highly

luminescent featureless domain zoning. Some grains exhibited transgressive overgrowths and convoluted metamorphic cores (Figure 12f).

One hundred and eleven analyses were conducted on 108 individual zircon grains from sample AS2010-62D (Figure 12d). Of the 111 analyses collected, 10 were rejected outright on the basis of noisy isotopic ratios and high levels of common Pb. Figure 12e shows a significant peak in the detrital zircon age spectra at *c.* 1820 Ma. The $^{207}Pb/^{206}Pb$ weighted average age of the youngest peak is 1823 ± 9.7 Ma (n=43, MSWD=2.7) and is yielded from typically oscillatory zoned and highly luminescent domain zoned grains. The first and second youngest concordant oscillatory zoned grains have $^{207}Pb/^{206}Pb$ ages of 1714.9 ± 19 Ma and 1746.2 ± 19 Ma with concordancy of 99 and 102% respectively. A broad range of age data between *c.* 2000-2700 Ma is also apparent, with minor peaks in the age spectra at *c.* 2070 Ma and 2460 Ma emerging from weakly luminescent oscillatory zoned and highly luminescent domain zoned grains respectively. The age spectrum of this sample has distinct similarities with sample AS2010-62D.

6 DISCUSSION

The Wigley Block preserves a protracted history of tectonometamorphic events between *c.* 1800-1100 Ma. The following discussion aims to interpret the timing and conditions of tectonometamorphism which produced the dominant structural character of the Wigley Block. The timing and P-T constrains on metamorphism and magmatic events within the Wigley Block have significant implications for redefining the southern margin of the North Australia Craton during the assembly of Proterozoic Australia.

6.1 Interpretation of geochronology

6.1.1 Monazite U-Pb age data

Monazite is a common accessory mineral in amphibolite to granulite facies terranes and thus can be very powerful for understanding the age constraints and P-T conditions of high grade metamorphic events (Kelly *et al.* 2006, Kingsbury *et al.* 1993, Parrish 1990, Smith and Barreiro 1990). Throughout the study, monazite samples AS2010-65J, AS2010-66J, AS2010-72D and RED2010-01 exhibit a single age population ranging between *c*. 1122 and 1142 Ma. Samples AS2010-63D, AS2010-66D and AS2010-67A2 have two age populations, with a common young population at *c.* 1100 Ma and an old population between c. 1565 and 1720 Ma.

Monazite grains from sample AS2010-65J in the E-W trending high strain zone have a single age population of 1128 ± 12 Ma. Studies have demonstrated that U-Pb ages in relatively large (50-100 μm) monazite grains can remain unaffected by temperatures in excess of 750-800 °C even with very slow cooling rates, therefore monazites shielded from resetting by garnet grains are more likely to preserve the age of initial crystallisation (Cutts *et al.* 2010, DeWolf *et al.* 1993, Rubatto *et al.* 2001, Seydoux-Guillaume *et al.* 2002). Alternatively, it is possible that the monazite grains were originally older and were reset during subsequent metamorphism. The recrystallization of monazite can be facilitated by the presence of fluids at low temperatures, as monazites can be dissolved and reprecipitated in locations easily accessible by hydrothermal fluid including along grain boundaries and within microfractures (Crowley and Ghent 1999, DeWolf *et al.* 1993, Kelly *et al.* 2006, Parrish 1990). Therefore given the probability of pre-Grenvillian monazite at *c.* 1600 or 1700 Ma, it is likely

that monazite from sample AS2010-65J were completely reset during metamorphism at *c.* 1130 Ma, leading to the development of Grenvillian-only monazite.

Monazites obtained from a microgranite which intruded an intensely foliated augen gneiss from the E-W trending high strain zone in the central Wigley Block (AS2010-66J), preserve a single $^{207}Pb/^{206}Pb$ age population of 1116.3 ± 12 Ma. Since the microgranite cross cuts the gneiss and is also weakly foliated parallel to the intense E-W foliation of the augen gneiss, it is possible that the microgranite intruded the augen gneiss during deformation associated with the formation of the E-W trending fabric (Figure 4f). The ages preserved by monazite provide an age constraint on the deformation.

Monazites analysed from the south-up E-W trending mylonitic fabric in AS2010-72D preserve a single age population with a $^{207}Pb/^{206}Pb$ weighted isotopic age of 1127 ± 20 Ma. The minimum age of the E-W trending mylonitic system is constrained by the presence of cross cutting dolerite dykes of the 1080 Ma Stuart Dyke Swarm (Figure 4h). Subsequently, it is likely that the monazites preserved within this sample record the age of the mylonitisation at *c.* 1130 Ma. This interpretation is supported by Grenvillian-aged monazite data obtained from sample AS2010-65J as well as the age of the syn-deformational microgranite, suggesting that metamorphism at *c.* 1130 Ma was coeval with pervasive E-W trending deformation.

Further west in the vicinity of the Teapot Complex (Figure 1), monazites analysed within biotite grains and along grain boundaries of the foliated matrix in sample RED2011-01 yield a single age population with a $^{207}Pb/^{206}Pb$ weighted isotopic age of 1141.9 ± 9.9 Ma. Due to the microstructural location of the monazite, it is a reasonable assumption that the ages preserved within biotite grains of the foliated matrix reflect the age of the tectonic fabric.

In contrast to the samples discussed above that have single age populations, ages obtained from samples AS2010-63D, AS2010-66D and AS2010-67A2 are more complex. All three samples exhibit a discordia which defines an upper intercept between *c.*1600 and 1700 Ma and a lower intercept at *c.* 1110 Ma. Sample AS2010-66D exhibits a discord of monazite with an upper intercept of 1735 ± 28 Ma which is statistically comparable with the $^{207}Pb/^{206}Pb$ weighted average age of the oldest concordant population in the sample (1720 ± 17 Ma). *In situ* analysis reveals the older age population typically comes from monazite shielded within garnet, quartz and matrix biotite, where as younger ages were obtained from monazite located along the grain boundaries of

biotite and sillimanite within the foliated matrix. Therefore, it is probable that the 1720 ± 17 Ma population of monazite included within the coarse-grained matrix assemblage and the 1091.9 ± 5.4 Ma population of monazite located within foliated matrix are both metamorphic, thus suggesting polymetamorphism. Similarly, sample AS2010-67A2 exhibits a discordia with an upper intercept of 1565 ± 20 Ma which is statistically comparable with the $^{207}Pb/^{206}Pb$ weighted average age of the old population (1598 ± 26 Ma). *In situ* analysis reveals the older age population typically comes from monazite grains analysed along the grain boundaries of biotite and garnet within the matrix, whereas younger ages were obtained from monazite analysed within biotite in the foliated matrix. Likewise, it can be suggested that 1598 ± 26 Ma monazite grains are located within biotite and garnet within the matrix assemblage and 1127 ± 20 Ma monazite grains included within biotite within the foliated matrix are both metamorphic, again suggesting polymetamorphism. However, in this case, there is no evidence for the event at *c.* 1720 Ma that is recorded in AS2010-66D.

Sample AS2010-63D also has a discordant population, however the absence of an old concordant population produces a poorly constrained upper intercept at 1763 ± 31 Ma (MSWD=1.7). One concordant analysis is present at 1668 ± 18 Ma, however little weight can be placed upon this age as it is within error of the discord and concordia. *In situ* analyses indicates 1638 ± 19 Ma aged monazite grains were typically preserved within the garnet-sillimanite-biotite bearing assemblage whereas younger 1090 ± 15 Ma aged monazites were located within the cordierite-bearing matrix. Similarly, sample AS09-4 exhibits a garnet-bearing assemblage being texturally replaced by a cordierite-bearing assemblage. Monazites hosted within cordierite coronas have been directly dated at 1119 ± 7.4 Ma (n=37, MSWD=2.2, Cutts and Hand unpublished data, April 2011, Figure 11e), and are interpreted to preserve the growth age of the cordierite-bearing mineral assemblage which post dates the older *c.* 1700 Ma garnet-bearing assemblage.

Another interpretation is that the older monazite populations identified in sample AS2010-66D, AS2010-67A2 and AS2010-63D are detrital. Detrital monazite is less common than detrital zircon in high-grade rocks, but a number of studies (eg. Rubatto *et al.* 2001, Williams 2001) have shown that monazite can preserve detrital ages during subsequent high-grade metamorphism. In this case, an argument exists to say the terrain has not undergone metamorphism at *c.*1760-1720, *c.*1600 and *c.*1130. If this is the case, the older populations of monazite define a maximum depositional age of 1720 ± 17 Ma, 1565 ± 20 Ma and ~ 1668 ± 18 Ma for each sample respectively. The absence of multiple older monazite populations in any one sample supports this

interpretation as monazite samples in close proximity to each other do not record the same metamorphic ages (see also zircon metamorphic ages below). In this case, the single common metamorphic age at *c.*1130 Ma in all samples might suggest that deposition occurred in the interval *c.*1600-1130 Ma. However due to the limitations of the study, it is not possible to conclusively distinguish whether the old monazite populations are metamorphic or detrital.

6.1.2 Zircon U-Pb age data

Zircons analysed from sample AS2010-64J preserve two distinct populations. Cores and rims from weakly luminescent oscillatory and sector zoned zircons yield a $^{207}Pb/^{206}Pb$ isotopic age of 1649.7 ± 6.8 Ma. Oscillatory and sector zoning are characteristic features of igneous zircons (eg. Corfu *et al.* 2003) and are likely to represent the age crystallisation of igneous precursors to the augen gneiss (Corfu *et al.* 2003, Hoskin and Schaltegger 2003). Cores from weakly luminescent zircons exhibiting fuzzy primary igneous and convoluted zoned zircons are characteristic of metamorphic growth (eg. Whitehouse and Kemp 2010) and give a $^{207}Pb/^{206}Pb$ isotopic age of 1637 ± 13 Ma. Inherited zircons exposed to lower-grade P-T conditions typically show evidence of resorption or metamorphic overgrowths (Hoskin and Schaltegger 2003) as opposed to zircons subjected to high-grade granulite facies conditions, which may completely recrystallise during metamorphism at sub-solidus conditions or during anatexis (Roberts and Finger 1997, Rubatto *et al.* 2001, Schaltegger *et al.* 1999). Solid-state modifications of magmatic zircons can however occur during late and post-magmatic cooling thus the possibility exists that these features did not develop during a discrete metamorphic event must be considered (Corfu *et al.* 2003). Subsequently, the analysis of zircon internal morphologies alone cannot be used to attribute the two age populations to two discrete events. However, it is probable that the older population of zircons formed in response to melt crystallisation.

Zircons from sample COL2011-01 were obtained from a small scale migmatitic leucosome which parallels fabric within the augen gneiss represented by AS2010-64J. Weakly luminescent moderate oscillatory and featureless domain zoning in zircon grains in this sample give a $^{207}Pb/^{206}Pb$ isotopic age of 1636.8 ± 6.5 Ma. As previously described, these zircons exhibit features characteristic of igneous origin. However, the structural context of this sample suggests the zircons are more likely to represent a metamorphic age linked to partial melting. In this case, the igneous morphologies are interpreted to reflect zircon growth in a melt-

dominated migmatitic segregation. The age of these migmatite-hosted zircons is identical within error to the younger population in AS2010-64J. This suggests the younger population in AS2010-64J may be metamorphic, and also record the age of migmatisation which produced the pervasive quartzofeldspathic segregations throughout the augen gneiss.

Sample HAM2011-02 was obtained from a syn-tectonic pegmatite which accumulated in the strain shadow adjacent to a mafic boudin (Figure 4g). This sample was obtained ~50km west of the central Wigley Block within the regional E-W trending high-strain fabric in the area (Figure 3b). Very weakly luminescent oscillatory and sector zoned zircon rims from this sample give a $^{207}Pb/^{206}Pb$ isotopic age of 1137.4 ± 8.1 Ma. Xenocrystic cores typically exhibit chaotic internal fracturing associated with metamictisation (Corfu *et al.* 2003). Overgrowths of weakly luminescent oscillatory and sector zones are typical igneous characteristics, and reflect growth in a melt-dominated volume, consistent with the interpretation that melt migrated to the strain shadow region during deformation. Therefore it seems likely that the age preserved by the pegmatite dates the timing of melt crystallisation during deformation. This interpretation is supported by the observation that elsewhere in the same high-strain fabric, pegmatite segregations underwent solid-state deformation indicating that deformation occurred before, during and after melt migration within the fabric.

Zircon from sample HAM2011-08 were obtained from a migmatitic melt vein which parallels the regional E-W trending fabric in the Hamilton Creek area (similar to COL2011-01). The sample gives two distinct age populations joined by a discordia. Highly luminescent strongly oscillatory and sector zoned zircon cores and rims preserved a $^{207}Pb/^{206}Pb$ weighted average isotopic age of 1626.9 ± 7.1 Ma. Smaller weakly luminescent oscillatory zoned zircon rims from the second population produced a younger $^{207}Pb/^{206}Pb$ isotopic age of 1139 ± 19 Ma. The comparatively large error reflects the small number of analyses. As previously described, both age populations exhibit internal morphologies characteristic of igneous origin that can be interpreted to represent (a) the magmatic crystallisation or (b) growth of zircon in response to a high-grade metamorphic event associated with partial melting and recrystallization of inherited crystals (Corfu *et al.* 2003, Hoskin and Schaltegger 2003). Cores and rims from the older population of zircon in sample HAM2011-08 yield ages within error and do not typically exhibit internal morphologies characteristic of metamorphic growth, therefore it seems probable that the zircon grains preserve a magmatic crystallisation age of 1626.9 ± 7.1 Ma. The younger 1139 ± 19 Ma zircon population is joined to the older age population by a discordia which has an

upper intercept of 1640 ± 15 Ma. The occurrence of discordant analyses suggests the partial resetting of the U-Th-Pb system of inherited *c.*1630 Ma zircons in response to metamorphism at *c.*1130 Ma. Therefore it is probable that the rims of the younger zircons preserve the age of the crystallisation of the melt vein and therefore in all probability the age of the foliation that confines the melt vein. This interpretation is consistent with the age of 1137 Ma age obtained from the regional E-W trending fabric elsewhere in the Hamilton Creek area (HAM2011-02) as well as the monazite ages from the central Wigley Block and the Teapot Complex area.

6.2 Age constraints on protoliths

6.2.1 Maximum depositional age for sediments

Detrital zircon analysis was performed on two metasedimentary samples incorporated within unnamed Paleoproterozoic gneisses of the central Wigley Block. In sample AS2010-62D, 61 out of 75 analyses were between 95-105% concordant and record a large spread of ages between *c.* 1590-2864 Ma (Figure 12b). Zircons exhibiting rounded 'soccer ball' shapes, internal recrystallization fronts (Figure 12c) and convoluted zoning yield the youngest ages with a spread between *c.* 1590 and 1755 Ma and give a maximum depositional age of 1591.5 ± 19.3 Ma. These internal and external zircon morphologies typically form in response to metamorphic processes of varying grade and are likely to represent the resorption or solid-state recrystallization of inherited zircons (Corfu *et al.* 2003). Throughout the study, many near concordant zircon analyses were obtained (Figure 12a), and can be interpreted to have experienced Pb loss in response to various geological processes (eg. Whitehouse and Kemp 2010). One interpretation is that they are metamorphic style zircons which grew during one or more metamorphic events, however the data does not definitively allow the age of those events to be well constrained. One possibility is the spread of ages from metamorphic style zircon reflects resetting during an event at *c.*1650 Ma. However, resetting at *c.*1130 Ma is more probable to have occurred. If these zircons were partially reset by post deposition metamorphism at *c.*1130 Ma (as suggested by analyses which lie along a discordia), the ages preserved by the youngest detrital zircons may not reflect their initial crystallisation age hence impact the true maximum depositional age of the sample. If the spread of metamorphic style zircon between *c.* 1590-1755 Ma are interpreted to reflect post depositional modifications,

the next youngest cluster of detrital zircons exhibiting characteristic igneous morphologies in this sample give a conservative $^{207}Pb/^{206}Pb$ weighted isotopic maximum depositional age of 1835 ± 20 Ma (n=23, MSWD=3.1).

In sample AS2010-59J, 81 out of 101 analyses were between 95-105% concordant, recording a large spread of ages between *c.* 1714- 2640 Ma (Figure 12e). Zircons exhibiting highly luminescent oscillatory cores and sector zoned rims yield the youngest ages with a spread between *c.* 1714 and 1757 Ma and give a maximum depositional age of 1714.9 ± 19 Ma. These morphologies have the character of grains likely to represent the crystallisation age in response to a magmatic or high grade metamorphic event (eg. Corfu *et al.* 2003). Unlike sample AS2010-62D, this sample does not yield any *c.*1591- 1755 Ma zircons that preserve characteristic metamorphic morphologies. However similarly to AS2010-62D, analyses are typically near concordant and seem to trend down the discordia to a metamorphic event at *c.* 1130 Ma. The youngest cluster of detrital zircons in this sample has a $^{207}Pb/^{206}Pb$ weighted isotopic maximum depositional age of 1823 ± 9.7 Ma (n=43, MSWD=2.7) which is comparable to the youngest peak observed in sample AS2010-62D of 1835 ± 20 Ma.

Similarly, monazite from the old age populations of samples AS2010-63D, AS2010-66D and AS2010-67A2 can also be used to determine the maximum depositional ages for metasedimentary rocks within the Wigley Block assuming they are detrital. These samples give a maximum depositional age range between *c.* 1565 and 1720 Ma which are comparable with the maximum depositional age of *c.* 1591 Ma of detrital sample AS2010-62D. The difference in maximum depositional ages demonstrated by the three samples may represent a shift in provenance during sedimentation.

If the sediments of the Wigley Block were deposited at *c.*1835 Ma, this raises the question as to why *c.*1630 Ma aged migmatisation and associated deformation recorded in AS2010-64J are not recorded by monazite samples when there is such strong evidence for *c.*1630-1650 Ma metamorphism recorded within migmatitic melt veins of nearby zircon samples. There are several possible explanations for this relationship. Firstly, metasediments of the Wigley Block were deposited after metamorphism at *c.* 1630 Ma therefore the detrital populations of monazites in sample AS2010-63D, AS2010-66D and AS2010-67A2 do not necessarily record this event (i.e. the granites (AS2010-64J and HAM2011-08) are basement to the pelites). Secondly, the pelites were deposited at *c.*1700 Ma however were not in the vicinity of the *c.*1650 Ma granite and the subsequent

deformation/metamorphic event at 1630 Ma. In this model, the granites and 1630 Ma metamorphic rocks were subsequently structurally juxtaposed next to the pelites in an extensional detachment setting. However both migmatitic granites and metasediments are now intimately interlayered, suggesting it is not a simple case of juxtaposing a metamorphic rock system against less metamorphosed rocks prior to or during Grenvillian deformation. It is beyond the scope of this study to determine if structural juxtaposition of different tectonic histories has occurred, and at this stage a conservative interpretation is that the absence of *c.* 1630 Ma monazite ages in the pelites suggests sedimentation occurred post-1630 Ma. Sequences of <1630 Ma are widespread in the Warumpi Province to the south (Morrissey *et al.* 2011) and therefore the Wigley Block may also have sedimentary units of similar ages.

6.2.2 Igneous protolith ages

A sample of migmatised augen gneiss (AS2010-64J) located within the E-W trending structural belt of the central Wigley Block yields a $^{207}Pb/^{206}Pb$ weighted isotopic zircon age of 1649.7 ± 6.8 Ma. Similarly, zircons from a migmatised augen gneiss (HAM2011-08) located in Hamilton Creek ~50 km along strike of central Wigley Block yield a $^{207}Pb/^{206}Pb$ weighted isotopic zircon age of 1626.9 ± 7.1 Ma. The spatial distribution of these samples suggests the presence of a widespread magmatic event within the southern margin of the Aileron Province between *c.*1630-1650 Ma. The proximity of sample AS2010-64J to the visually indistinguishable units of the voluminous Flint Springs Gneiss suggests similar ages are prevalent throughout the Wigley Block. Comparable ages of magmatism have been documented within the Warumpi Province from the *c.*1650 Ma Boggy Hole Suite (Figure 2, Zhao and Bennett 1995, Zhao and McCulloch 1995). The Boggy Hole Suite belongs to the Calcalkaline-trondhjemitic (CAT) subgroup of granites and consist of largely quartzofeldspathic augen and biotite gneisses which were derived from a relatively mafic source (Warren and Shaw 1995, Zhao and McCulloch 1995, Zhao and Cooper 1992). The timing of magmatism within the central Wigley Block is approximately coeval with the timing of the *c.* 1640 Ma Liebig Orogeny documented within the Warumpi Province (Scrimgeour *et al.* 2005b), and may suggest magmatism associated with this event is more extensive than previously thought. It may also suggest that the Warumpi Province is not exotic to the Aileron Province as suggested by Scrimgeour *et al.* (2005b).

6.3 Interpretation of P-T conditions and diffusion-based cooling history

Sample AS2010-65J comes from the E-W trending high strain zone that runs through the central Wigley Block. The construction of a P-T pseudosection from this sample integrated with diffusion based cooling rates provides new information on the P-T conditions of Grenvillian-aged metamorphism in the central Wigley Block. The peak metamorphic mineral assemblage constrains pressure and temperature conditions between ~775 to 830 °C and 6 to 10 kbars (Figure 6). Spot analyses obtained from zoned garnet grains decrease in X_{Ca} from ~0.043 in the core to ~0.038 in the rim and further constrain peak pressure conditions between approximately 7.9 to 9.3 kbars. *In situ* U-Pb monazite geochronology of sample AS2010-65J yields a $^{207}Pb/^{206}Pb$ age of 1128 ± 12 Ma, however the peak garnet-bearing assemblage is unlikely to have grown during the Grenvillian (refer to interpretation of geochronology). Therefore it is likely that garnet grains from this sample were reset during Grenvillian-aged reworking. If this is the case, the decrease of X_{Ca} towards the rim of the garnets suggests the rock experienced decompression within the peak field during metamorphism. Similarly, the apparent absence of microstructural mineral relationship suggests the sample may have experienced a strongly decompressive path within the peak field.

Additionally in sample AS09-4 (Figure 5g), cordierite forms coronas that developed at the contact between garnet and the regional fabric within the central Wigley Block. In this sample, the monazite within the fabric has an age of 1119 ± 7.4 Ma (Cutts and Hand unpublished data, April 2011), confirming the fabric grew during the Grenvillian. Since cordierite developed at the expense of the fabric, it appears likely that a stable garnet-sillimanite-biotite assemblage was overprinted by cordierite and K-feldspar. Such a reaction texture is very common in rocks that undergo decompression from the mid-lower crust (Clarke and Powell 1991, Reid *et al.* 2008). Therefore, the development of syn-deformation cordierite-bearing assemblages at the expense of garnet-sillimanite-biotite bearing associations indicates that decompression accompanied deformation, and is probably a pressure response to the south side-up movement recorded by the shear zones during Grenvillian-aged deformation.

The composition of a small garnet core from sample AS2010-66D which has Grenvillian-aged monazites suggests elemental diffusion ceased in the core at approximately 780 °C (Figure 7c). This temperature coincides with the peak field between ~7.9 and 8.25 kbars within the estimated peak P-T space based on

calcium compositional isopleths. When integrated with the constrained P-T conditions and the field context of sample AS2010-65J, it suggests deformation associated with decompression and the development of the pervasive E-W trending fabric during the Grenvillian occurred under granulite facies conditions.

The P-T pseudosection calculated for AS2010-65J reflects the bulk composition of a comparatively anhydrous rock at Grenvillian times. However, if the rock had been previously metamorphosed (i.e. at *c.*1600 or 1700 Ma), it is also likely that the rock was dehydrated before Grenvillian deformation at *c.*1130 Ma. Consequently, the bulk composition of AS2010-65J cannot experience typical sub-solidus hydrous reactions involving muscovite, staurolite and chlorite that are expected at low P-T conditions in a standard metapelites prograde evolution (White *et al.* 2007, Morrissey *et al.* 2011). The volume and composition of the fluid lost from the system also impacts the position of the solidus and subsequently the peak mineral assemblage. For a sub-aluminous metapelitic composition with a H_2O content of 6.60 mol.%, the solidus is typically located at approximately 650 °C (White *et al.* 2007). Therefore it may be that the location of the solidus for the calculated for AS2010-65J at approximately 775 °C is higher than experienced by the rocks during Grenvillian metamorphism if further dehydration/melt loss has predicted the bulk composition corresponded to pre-Grenvillian times. However, in reality it is extremely difficult to constrain the H_2O content of the bulk composition during metamorphism. To explore the sensitivity of the calculated phase relationships in Figure 6, a T-x diagram could be constructed, using the bulk composition of AS2010-65J (x=0) and the same bulk composition with the H_2O content increased to ~7.5% (X=1), to investigate the sub-solidus reactions that may have occurred prior to melt loss. However due to time constraints, a T-x demonstrating this relationship was not completed.

6.4 Age of deformation in the southern Aileron Province

Tectonic events between *c.* 1100 and 1650 Ma have been recorded within samples from the central Wigley Block. The $^{207}Pb/^{206}Pb$ weighted isotopic ages of monazite and zircon found in nine structurally constrained samples within this study range from 1090 ± 15 Ma in sample AS2010-63D to 1141.9 ± 9.8 Ma in sample RED2011-01 and regionally correlate to the age of the 1130-1150 Ma Teapot Event (Biermeier *et al.* 2003a, Black and Shaw 1992, Collins and Shaw 1995, Scrimgeour *et al.* 2005b). This event has historically been

regarded as a thermal event. However Morrissey et al. (2011) demonstrated it corresponded to regional scale deformation which provided the macroscopic structural architecture in the Warumpi Province. This study significantly expands the structural magnitude of the Teapot Event as it shows that the crustal-scale high-strain belts along the southern margin of the Aileron Province and northern margin of the Warumpi province are Grenvillian in age.

Samples AS2010-65J, AS2010-66J and AS2010-72D located within the E-W trending high strain belt give single *c.* 1130 Ma aged populations. Monazite from a syn-tectonic microgranite within the E-W trending belt (AS2010-66J) preserves a crystallisation age of 1122.1 ± 9.1 Ma that is synchronous with the development of an E-W trending foliation observed in AS2010-65J. The mylonitic fabric in sample AS2010-72D gives a metamorphic age of 1129 ± 7.9 Ma for the fabric that records south-side up movement (Figure 4a). The minimum age of the E-W trending mylonitic system in the Wigley Block is constrained by the presence of cross cutting dolerite dykes of the 1080 Ma Stuart Dyke Swarm (Figure 4h).

Samples AS2010-63D, AS2010-66D and AS2010-67A2 are located within the fabric that predates the E-W trending belt and trends into the E-W zone in the central Wigley Block. These samples preserve two distinct age populations including a common younger *c.* 1110 Ma population which correlates with the Teapot Event, and an older population between *c.* 1600-1720 Ma. As previously discussed, monazite grains which preserve older ages are interpreted to be detrital and therefore do not support metamorphism in the central Wigley Block between *c.* 1600-1720 Ma.

Samples analysed from two other regions located between ~50-110km west along strike of the E-W trending structural corridor similarly exhibit $^{207}Pb/^{206}Pb$ monazite and zircon isotopic ages between *c.* 1137 and 1142 Ma. Zircons from a syn-tectonic pegmatite approximately 50km west of the central Wigley Block (HAM2011-02), preserve a crystallisation age of 1137.4 ± 8.1 Ma which is structurally interpreted as the age of migmatisation. A migmatised granitic gneiss located on the northern margin of the same mega boudin (HAM2011-08) displays two distinct concordant age populations of zircon at 1139 ± 19 Ma and 1626.9 ± 7.1 Ma which regionally correlate to the Teapot Event and Liebig Orogeny respectively (Scrimgeour *et al.* 2005b). The sample is dominated by *c.* 1627 Ma zircons which are interpreted to reflect the age of the igneous protolith within the younger overgrowths reflecting anatexis associated with regional deformation subsequent

crystallisation at *c.* 1140 Ma. Similarly, monazites analysed from a garnet-sillimanite-biotite gneiss (RED2011-01) located 110 km west of the central Wigley Block within the Teapot Complex, have an isotopic age of 1141.9 ± 9.9 Ma. This sample in particular has important regional implications. It is a strongly foliated gneissic fabric that has been overprinted by E-W trending upright folds. Previously, this migmatitic complex was considered to reflect a static thermal event (Collins and Shaw 1995, Collins and Williams 1995, Scrimgeour *et al.* 2005a, Shaw and Black 1991). However, the data from RED2011-01 shows that migmatisation within the Teapot Complex was associated with high-grade deformation. The integration of these samples to the data set compiled from the central Wigley Block and the results obtained by Morrissey *et al.* (2011) confirms the regional continuity and structural complexity of tectonometamorphic reworking attributed to the 1130-1150 Ma Teapot Event along the E-W trending southern margin of the southern Aileron Province and the Warumpi Province.

Samples AS2010-64J and COL2011-01 from the central Wigley Block produced igneous and metamorphic isotopic ages between *c.*1650 and 1636 Ma which regionally correlate to the age of the 1640 Ma Liebig Orogeny (Scrimgeour *et al.* 2005b). In conjunction with the protolith age of sample HAM2011-08 further west, this suggests *c.*1650-1630 Ma magmatism and metamorphism previously confined to the Warumpi Province extends further north into the southern Aileron Province.

Through the analysis of U-Pb isotopic systems in monazite and zircon, the dominant structural character of the central Wigley Block is unequivocally the result of the *c.* 1130-1150 Ma Teapot Event. Deformation during this event may have occurred to produce a flat lying fabric within a north-south extensional system. This may account for the development of E-W trending folds and laterally continuous E-W trending high strain belts (eg. Goscombe *et al.* 2003), which are paralleled by a series of pervasive south side up mylonites which concentrate on the steeply dipping limbs of the upright folds. Migmatised granitic gneisses throughout the Wigley Block provide evidence for extensive magmatism and subsequent metamorphism at *c.* 1630 Ma coeval with the 1640 Ma Liebig Orogeny documented within the Warumpi Province.

6.5 Regional implications

Monazite and zircon ages recorded throughout the study, combined with those of Morrissey *et al.* (2011) confirm the regional continuity and structural complexity of tectonometamorphic reworking attributed to the 1130-1150 Ma Teapot Event in the southern Aileron Province and northern Warumpi Province. Although sporadic, Grenvillian-aged data has been recorded in several other studies throughout the southern margin of the Arunta region (Figure 13 and Table 4). Most recently, monazite and Sm-Nd garnet analysis of metasediments have recorded extensive 1120-1159 Ma ages throughout the eastern Warumpi Province in structures previously attributed to the *c.* 1590 Ma Chewings Orogeny (Morrissey *et al.* 2011). Further west within the Warumpi Province, zircons from the Teapot Granite yield a $^{207}Pb/^{206}Pb$ crystallisation age of 1136 ± 6 Ma (Black and Shaw 1995), Rb-Sr ages record the recrystallisation of micas in the Ormiston Pound Granite between 1100-1030 Ma (Collins *et al.* 1995) and zircons from migmatites of the Kakalyi Gneiss west of Mt Liebig preserve a crystallisation age of 1149 ± 3 Ma (Scrimgeour *et al.* 2005b). In the southern Aileron Province, monazite rims from deformed amphibolite to granulite facies metapelites north of the Redbank Shear Zone record 1139 ± 25 Ma ages (Biermeier *et al.* 2003a) and a pegmatite yielded a Rb-Sr age of 1140 ± 56 Ma (Shaw and Black 1991). Lastly, in the western Aileron Province, the undeformed ultramafic Mordor Complex has a zircon crystallisation age of 1133 ± 5 Ma (Claoué-Long and Hoatson 2005).

Until recently, the Teapot Event was believed to be mostly thermal in nature with little to no evidence of associated deformation or metamorphism (Collins and Shaw 1995, Collins *et al.* 1995, Scrimgeour *et al.* 2005a, Shaw and Black 1991). However, recent work conducted within the eastern Warumpi Province provides evidence for significant deformation associated with Grenvillian-aged metamorphism at *c.*1130 Ma originally attributed to the *c.* 1590 Ma Chewings phase of deformation (Morrissey *et al.* 2011). Furthermore in the Casey Inlier in the northeast of the Amadeus Basin (Figure 13), regional deformation of a Mesoproterozoic cover succession under upper greenschist facies conditions produced a pervasive NW-SE trending schistose fabric and kilometre scale isoclinal folding in response to easterly directed thrusting (Close *et al.* 2007). The deformation has not been directly dated however maximum depositional ages obtained from a Mesoproterozoic cover succession and the unconformably overlying Neoproterozoic Heavitree Quartzite provide maximum and minimum age constraints on deformation between *c.* 1235 and 800 Ma (Close *et al.*

2007). Integrated with strong evidence for Grenvillian-aged deformation from the Wigley Block, it seems likely the timing of the Teapot Event is associated with extensive deformation along the southern margin of the Arunta Region. If the probable Grenvillian-aged structural trends in the Casey Inlier are rotated through their smallest angle and oriented parallel with the fabric in the southern Aileron and northern Warumpi Province, the tectonic transport is south over north which is the same as that recorded in the Wigley Block and Hamilton Creek area.

Extensive geochronological data collected from the Wigley Block south of the Redbank Shear Zone, provides irrefutable evidence for Grenvillian-aged metamorphism associated with intense E-W trending, N-S compressional deformation. Presently no evidence of Grenvillian-aged reworking has been recorded in regions north of the Redbank Shear Zone (i.e. Strangways Range (Claoué-Long *et al.* 2008, Maidment *et al.* 2005), therefore the Redbank Shear Zone is interpreted to represent the macroscopic boundary of the northern edge of the Grenvillian orogenic belt in the southern Aileron Province (Figure 14). The Redbank Shear Zone has been interpreted to have experienced a protracted history of activation and reactivation from the Mesoproterozoic to the Palaeozoic (Marjoribanks and Black 1974, Teyssier 1985, Hand and Sandiford 1999). North over south thrust movement of the Redbank Shear Zone is interpreted to have initiated at or before 1500-1400 Ma during the Anmatjira Orogenic Phase, resulting in dehydration and intense mylonitisation of the surrounding host rocks. However there is no robust or definitive geochronology to support this notion (eg. Biermeier *et al.* 2003b, Shaw and Black 1991) and the data that does exist is based on interpretation or the use of disequilibrium geochronological techniques. In contrast, the data provided by this study is from structurally constrained samples using robust *in situ* geochronological techniques. Additionally, Hamilton Creek samples HAM2011-02 and HAM2011-08 come from the regionally defined Redbank Deformed Zone suggesting that the history of the Redbank zone might be dominantly Grenvillian. This is also apparent in the data of Biermeier *et al.* (2003a) who obtained Grenvillian ages from xenotime in high grade metasediments within the E-W trending high strain rocks in the Mount Ziel area north of the Teapot Complex. The presence of regionally developed E-W trending structures within the southern North Australian Craton and the northern Warumpi Province coincides with the suture trend of the Redbank Shear Zone and Grenvillian-aged geochronological data (Figure 14). The geochronological data presented here introduces the possibility that the suture imaged by Selway et al. (2009, 2006, Figure 14) is Grenvillian in age.

The Grenvillian-aged orogenic belt in the Arunta region has recently been postulated as continuously linked from the Warumpi Province to the Musgrave Province by Morrissey et al. (2011) through the interpretation of seismic and aeromagnetic data. Sub-horizontal reflections observed in seismic images extending beneath the later Neoproterozoic to Mid-Palaeozoic Amadeus Basin have been interpreted to correlate with a structural fabric associated with north-directed transport in the eastern Warumpi Province (Morrissey *et al.* 2011). Steeply dipping foliations observed in the Wigley Block appear to shallow towards the south and parallel the foliations observed beneath the Amadeus Basin which supports the interpretation that the basement south of the Redbank Shear Zone to the southern margin of the Amadeus Basin forms a single tectonic province (Wright *et al.* 1991).

The timing of deformation in the southern Aileron and Warumpi Province coincides with the later stages of the pervasive long-lived *c.* 1220 to 1140-1120 Ma Musgrave Orogeny in the Musgrave Province (Kelsey *et al.* 2010, Smithies *et al.* 2011). The Musgrave Province is an understudied Proterozoic terrane which lies at the triple junction between the North, West and South Australian Cratons (Figure 1, Kelsey *et al.* 2010, Smithies *et al.* 2011). Metamorphism in this region is characterised by ultrahigh temperatures (UHT) of up to 1000 °C in comparatively thin crust (Kelsey *et al.* 2010). Due to the prolonged duration of the magmatism (~60 Ma), these authors (Kelsey *et al.* 2010, Smithies *et al.* 2011, Evins *et al.* 2010) have interpreted the Musgrave Province to represent extensional upwelling associated with a failed intracontinental rift system. However, if the south-dipping lithospheric-scale feature imaged by Selway *et al.* (2009) is a Grenvillian-aged structure, one logical interpretation is that it represents the south-directed underthrusting of the North Australian Craton lithosphere. Selway *et al.* (2009) interpreted this feature to be a fossilised subduction zone associated with the *c.*1640 Ma Liebig-age accretion of the North Australian Craton to the Warumpi Province. However based on the regional extent of compressional south-over-north Grenvillian-aged structures at the surface above this feature, another interpretation is that it is a Grenvillian-aged subduction zone. In this case the UHT Musgrave Province would have existed in a back arc setting which has been suggested by a number of workers as a logical geodynamic environment for long lived UHT metamorphism in thin crust (Brown 2007, Hyndman *et al.* 2005, Currie and Hyndman 2005). The back arc system in the Musgrave Province may have existed until collision terminated the system at *c.* 1150 Ma. This would explain why deformation in the southern North

Australian Craton and the northern Warumpi Province occurred at the end of the long-lived UHT event in the Musgrave Province.

7 CONCLUSIONS

U-Pb geochronology reveals the dominant structural architecture of the southern margin of the Aileron Province, central Australia is unequivocally the result of Grenvillian-aged (*c.*1130 Ma) reworking. Deformation associated with this event produced kilometre-scale E-W trending folds which evolved over time into shear zones and mylonites with south-side up kinematics. Phase equlibria modelling on metapelites from the central Wigley Block indicates metamorphic conditions during the Grenvillian were around 8.5 kbars and 800 °C, and were associated with the development of syn-deformation cordierite bearing assemblages at the expense of earlier garnet, sillimanite and biotite. The formation of cordierite implies that the rocks followed a decompressional evolution. The pervasive Grenvillian deformation overprints an earlier high-grade metamorphic event at *c.* 1630 Ma which is recorded by zircon growth in migmatitic fabrics of granitic protoliths which intruded between 1650 and 1630 Ma. Monazites within the Wigley Block also record ages between *c.*1600 and 1720 Ma and may suggest the occurrence of multiple pre-Grenvillian metamorphic events. However the lack of conclusive evidence for 1630 Ma metamorphism within the metapelitic rocks suggests these older monazite ages may be detrital rather than metamorphic. Detrital zircon grains provide a conservative maximum depositional age of *c.* 1830 Ma for the metasediments, and the occurrence of younger concordant grains down to *c.* 1590 Ma may represent metamorphically induced partial Pb loss during Grenvillian overprinting, although metamorphism at c.1600 Ma cannot be ruled out. Deformation in the southern Aileron Province is kinematically comparable with a south-dipping lithospheric-scale feature imaged to depths of 200km by magnetotellurics (Selway *et al.* 2009), which has previously been interpreted to represent a fossilized Paleoproterozoic subduction zone. However, it is possible that this interpreted fossil subduction zone is a Grenvillian feature and was associated with extensive crustal reworking which marks the suturing of the North Australian Craton with rocks comprising of the Musgrave Province and the South Australian Craton.

8 ACKNOWLEDGEMENTS

I am most thankful to my supervisor, Martin Hand, who has been my constant pillar of support throughout the year. I feel very privileged to have worked beside such a knowledgeable person. A big thankyou to PhD students Alec Walsh and Jade Anderson, and 2010 honours student Laura Morrissey for their never ending support and always finding time around their busy schedules to help, particularly with THERMOCALC. To Justin Payne for offering support and advice in the final few months. Kathryn Cutts and David Kelsey for answering questions on THERMOCALC. Katie Howard for her support throughout the year and answering many monazite and zircon related questions. My deepest thanks to Angus Netting, Ben Wade and the staff at Adelaide Microscopy for their technical support, weekend phone calls and last minute carbon coating- your dedication is truly appreciated. To my family for their support and understanding throughout the year- I promise I will help out around the house more from now on. And finally to the Honours students of 2011 who made this year truly memorable!

9 REFERENCES

ALEINIKOFF J. N., SCHENCK W. S., PLANK M. O., SROGI L. A., FANNING C. M., KAMO S. L. & BOSBYSHELL H. 2006 Deciphering igneous and metamorphic events in high-grade rocks of the Wilmington Complex, Delaware: Morphology, cathodoluminescence and backscattered electron zoning, and SHRIMP U-Pb geochronology of zircon and monazite, *Geological Society of America Bulletin,* vol. 118, no. 1-2, pp. 39-64.

BETTS P. G. & GILES D. 2006 The 1800-1100 Ma tectonic evolution of Australia, *Precambrian Research,* vol. 144, pp. 92-125.

BETTS P. G., GILES D., LISTER G. S. & FRICK L. R. 2002 Evolution of the Australian lithosphere, *Australian Journal of Earth Sciences,* vol. 49, pp. 661-695.

BETTS P. G., GILES D. & SCHAEFER B. F. 2008 Comparing 1800-1600 Ma accretionary and basin processes in Australia and Laurentia: Possible geographic connections in Columbia, *Precambrian Research,* vol. 166, pp. 81-92.

BIERMEIER C., STÜWE K., FOSTER D. A. & FINGER F. 2003a Thermal evolution of the Redbank thrust system, central Australia: Geochronological and phase-equilibrium constraints, *Tectonics,* vol. 22, pp. 1-23.

BIERMEIER C., WIESINGER K., STÜWE K., FOSTER D. A. F., GIBSON H. J. & RAZA A. 2003b Aspects of the structural and late thermal evolution of the Redbank Thrust system, central Australia: constraints from the Spears Metamorphics, *Australian Journal of Earth Sciences,* vol. 50, pp. 983-999.

BLACK L. P. & SHAW R. D. 1992 U-Pb zircon chronology of prograde Proterozoic events in the central and southern provinces of the s Block, central Australia, *Australian Journal of Earth Sciences,* vol. 39, no. 2, pp. 153-171.

--- 1995 An assessment, based on U-Pb zircon data, of Rb-Sr dating in the Arunta Inlier, central Australia, *Precambrian Research,* vol. 71, pp. 3-15.

BROWN M. 2007 Metamorphic conditions in orogenic belts: A record of secular change, *International Geology Review,* vol. 49, pp. 193-234.

BUICK I. S., MILLER J. A., WILLIAMS I. S. & CARTWRIGHT I. 2001 Ordovician high-grade metamorphism of a newly recognised late Neoproterozoic terrane in the northern Harts Range, central Australia, *Journal of Metamorphic Geology,* vol. 19, pp. 373-394.

CAWOOD P. A. & KORSCH R. J. 2008 Assembling Australia: Proterozoic building of a continent, *Precambrian Research,* vol. 166, pp. 1-38.

CLAOUÉ-LONG J. & EDGOOSE C. J. 2008 The age and significance of the Ngadarunga Granite in Proterozoic central Australia, *Precambrian Research,* vol. 166, pp. 219-229.

CLAOUÉ-LONG J. & HOATSON D. M. 2005 Proterozoic mafic-ultramafic intrusions in the Arunta Region, central Australia. Part 2: Event chronology and regional correlations, *Precambrian Research,* vol. 142, pp. 134-158.

CLAOUÉ-LONG J., MAIDMENT D., HUSSEY K. & HUSTON D. 2008 The duration of the Strangways Event in central Australia: evidence for prolonged deep crust processes, *Precambrian Research,* vol. 166, pp. 246-262.

CLARKE G. L. & POWELL R. 1991 Decompressional coronas and symplectites in granulites of the Musgrave Complex, central Australia, *Journal of Metamorphic Geology,* vol. 9, no. 4, pp. 441-450.

CLOSE D. F., SCRIMGEOUR I. R., CARSON C. & CLAOUÉ-LONG J. 2007 Diverse terranes and mineral potential of the Casey Inlier, Arunta Region, *Annual Geoscience Exploration Seminar (AGES) 2007. Record of Abstracts. Northern Territory Geological Survey, Record 2007-001.*

CLOSE D. F., SCRIMGEOUR I. R., EDGOOSE C. J. & CROSS A. 2004 Late Palaeoproterozoic development of the SW margin of the North Australian Craton, *Geological Society of Australia (Abstracts),* vol. 73, p. 149.

CLOSE D. F., SCRIMGEOUR I. R., EDGOOSE C. J., CROSS A., CLAOUÉ-LONG J., KINNY P. D. & MEIXNER A. 2003 Redefining the Warumpi Province. In: Munson, T. W. Scrimgeour, I. (Eds), Annual Geoscience Exploration Seminar (AGES) 2003. Record of Abstracts, *Northern Territory Geological Survey Record 2003-01*.

COLLINS W. J. & SHAW R. D. 1995 Geochronological constraints on orogenic events in the Arunta Inlier: a review, *Precambrian Research,* vol. 71, pp. 315-346.

COLLINS W. J. & WILLIAMS I. S. 1995 SHRIMP ionprobe dating of short-lived Proterozoic tectonic cycles in the northern Arunta Inlier, central Australia, *Precambrian Research,* vol. 71, no. 69-89.

COLLINS W. J., WILLIAMS I. S., SHAW R. D. & MCLAUGHLIN N. A. 1995 The age of the Ormiston Pound Granite: implications for Mesoproterozoic evolution of the Arunta Inlier, central Australia, *Precambrian Research,* vol. 71, no. 91-105.

CONDIE K. C. 2000 Episodic continental growth models: afterthoughts and extensions, *Tectonophysics,* vol. 322, pp. 153-162.

COPELAND P., PARRISH R. R. & HARRISON T. M. 1988 Identification of inherited radiogenic Pb in monazite and its implications for U-Pb systematic, *Nature,* vol. 333, pp. 760-763.

CORFU F., HANCHAR J. M., HOSKIN P. W. O. & KINNY P. D. 2003 Atlas of zircon textures. In HANCHAR J. M. & HOSKIN P. W. O. eds. Zircon. pp. 468-500. Washington, D. C.

CROWLEY J. L. & GHENT E. D. 1999 An electron microprobe study of the U-Th-Pb systematics of metamorphosed monazite: the role of Pb diffusion versus overgrowth and recrystallisation., *Chemical Geology,* vol. 157, pp. 285-302.

CURRIE C. A. & HYNDMAN R. D. 2005 The thermal structure of subduction zones: The case for a hot back-arc, *EOS (Transactions of the American Geophysical Union),* vol. 86, abstract T11B-0366.

CUTTS K. A. & HAND M. unpublished data, April 2011 In situ U-Pb LA-ICPMS monazite dating, sample AS09-4. Adelaide University.

CUTTS K. A., KINNY P. D., STRACHAN R. A., HAND M., KELSEY D. E., EMERY M., FRIEND C. R. L. & LESLIE A. G. 2010 Three metamorphic events recorded in a single garnet: Integrated phase modelling, in situ LA-ICPMS and SIMS geochronology from the Moine Supergroup, NW Scotland, *Journal of Metamorphic Geology*.

DEWOLF C. P., BELSHAW N. & ONIONS R. K. 1993 A metamorphic history from micron-scale Pb-207/Pb-206 chronometry of Archean monazite, *Earth and Planetary Science Letters,* vol. 120, no. 3-4, pp. 207-220.

DODSON M., H. 1986 Closeure Profiles in cooling systems, *Materials Science Forum,* vol. 7, pp. 145-154.

EDGOOSE C. J., SCRIMGEOUR I. R. & CLOSE D. F. 2004 Geology of the Musgrave Block, Northern Territory. Northern Territory Geological Survey.

EVINS P. M., SMITHIES R. H., HOWARD H. M., KIRKLAND C., WINGATE M., T. D. & BODORKOS S. 2010 Devil in the detail; The 1150-1000 Ma magmatic and structural evolution of the Ngaanyatjarra Rift, west Musgrave Province, Central Australia, *Precambrian Research,* vol. 183, pp. 572-588.

FLÖTTMANN T. & HAND M. 1999 Folded basement-cored tectonic wedges along the northern edge of the Amadeus Basin, central Australia: evaluation of orogenic shortening, *Journal of Structural Geology,* vol. 21.

GANGULY J., CHENG W. & CHAKRABORTY S. 1998 Cation diffusion in aluminosilicate garnets: experimental determination in pyrope-almandine diffusion couples, *Contributions to Mineralogy and Petrology,* vol. 131, pp. 171-180.

GILES D., BETTS P. G. & LISTER G. S. 2002 Far-field continental backarc setting for the 1.80-1.67Ga basins of northeastern Australia.

--- 2004 1.8-1.5-Ga links between the North and South Australian Cratons and the Early-Middle Proterozoic configuration of Australia, *Tectonophysics,* vol. 380, pp. 27-41.

GOSCOMBE B., HAND M. & GRAY D. 2003 Structure of the Kaoko Belt Namibia: a progressive evolution of a classic transpressional orogen, *Journal of Structural Geology,* vol. 25, pp. 1049-1081.

GRIFFIN W. L., POWELL W. J., PEARSON N. J. & O'REILLY S. Y. 2008 GLITTER: data reduction software for laser ablation ICP-MS. In SYLVESTER P. ed. Laser Ablation ICP-MS in the Earth Sciences: Current Practices and Outstanding Issues., Mineralogical Association of Canada. Short Course Series 40. pp. 308-311.

HAINES P. W., HAND M. & SANDIFORD M. 2001 Palaeozoic synorogenic sedimentation in central and northern Australia: a review of distribution and timing with implications for the evolution of intracontinental orogens, *Australian Journal of Earth Sciences,* vol. 48, pp. 911-928.

HAND M. & BUICK I. S. 2001 The tectonic evolution of the Reynolds-Anmatjira Ranges: a case study in terrain reworking from the Arunta Inlier, central Australia, *Geological Society of London, Special Publications,* vol. 184, pp. 237-260.

HAND M. & SANDIFORD M. 1999 Intraplate deformation in central Australia, the link between subsidence and fault reactivation, *Tectonophysics,* vol. 305, pp. 121-140.

HAUZENBERGER C., ROBL J. & STÜWE K. 2005 Garnet Zoning in high pressure granulite-facies metapelites, Mozambique belt, SE-Kenya: constraints on the cooling history, *European Journal of Mineralogy,* vol. 17, pp. 43-55.

HOATSON D. M., SUN S. & CLAOUÉ-LONG J. 2005 Proterozoic mafic-ultramafic intrusions in the Arunta Region, central Australia. Part 1: Geological setting and mineral potential, *Precambrian Research,* vol. 142, pp. 93-133.

HOLLAND T. J. B. & POWELL R. 1998 An internally consistent thermodynamic dataset for phases of petrological interest, *Journal of Metamorphic Geology,* vol. 16, pp. 309-343.

HOSKIN P. W. O. & SCHALTEGGER U. 2003 The composition of zircon and igneous and metamorphic petrogenesis. In HANCHAR J. M. & HOSKIN P. W. O. eds. Zircon. pp. 27-62. Washington, D. C.

HYNDMAN R. D., CURRIE C. A. & MAZZOTTI S. 2005 The origin of global mountain belts: Hot subduction zone backarcs [abs], *EOS (Transactions of the American Geophysical Union),* vol. 86, abstracts T11B-0367.

JACKSON M. J., PEARSON N. J., GRIFFIN W. L. & BELOUSOVA E. A. 2004 The application of laser ablation-inductively coupled plasma-mass spectrometry to in situ U-Pb zircon geochronology, *Chemical Geology,* vol. 211, pp. 47-69.

KELLY N. M., CLARKE G. L. & HARLEY S. L. 2006 Monazite behaviour and age significance in poly-metamorphic high-grade terrains: A case study from the western Musgrave Block, central Australia, *Lithos,* vol. 88, pp. 100-134.

KELSEY D. E., HAND M., CLARK C. & WILSON C. J. L. 2007 On the application of in situ monazite chemical geochronology to constraining P-T-t histories in high-temperature (>850°C) polymetamorphic granulites from Prydz Bay, East Antarctica, *Journal of the Geological Society, London,* vol. 164, pp. 667-683.

KELSEY D. E., SMITHIES R. H., HAND M., CLARK C., KIRKLAND C. & EVINS P. M. 2010 What is the tectonic setting of long-lived Grenvillian-aged ultrahigh temperature, high geothermal gradient metamorphism in the Musgrave Province, central Australia?, *Geological Society of America Abstracts with Programs*.

KINGSBURY J. A., MILLER C. F., WOODEN J. L. & HARRISON T. M. 1993 Monazite paragenesis and U-Pb systematics in rocks of the eastern Mojave Desert, California, USA.: implications for thermochronometry, *Chemical Geology,* vol. 110, pp. 147-167.

LAMBECK K., BURGESS G. & SHAW R. D. 1988 Teleseismic travel-time anomalies and deep crustal structure in central Australia, *Geophysical Journal,* vol. 94.

LUDWIG K. R. 2003 User's Manual for Isoplot 3.00, *Berkeley Geochronological Centre, Special Publication*, no. No. 4, 71.

MAIDMENT D. & HAND M. 2002 The extent od Cambrian metasediments and the Ordovician Larapinta Event, eastern Arunta Province, central Australia, *Geological Society of Australia (Abstracts),* vol. 67.

MAIDMENT D., HAND M. & WILLIAMS I. S. 2005 Tectonic cycles in the Strangways Metamorphic Complex, Arunta Inlier, central Australia: geochronological evidence for exhumation and basin formation between two high-grade metamorphic events, *Australian Journal of Earth Sciences,* vol. 52, pp. 205-215.

MARJORIBANKS R. W. 1975 The structural and metamorphic geology of the Ormiston area, central Australia, *Bureau of Mineral Resources Australia Record 1975/13*.

MARJORIBANKS R. W. & BLACK L. P. 1974 Geology and geochronology of the Arunta Complex, north of Ormiston Gorge, central Australia, *Journal of the Geological Society of Australia,* vol. 21, pp. 291-299.

MCLAREN S., SANDIFORD M. & POWELL R. 2005 Contrasting styles of Proterozoic crustal evolution: A hot-plate tectonic model for Australian terranes.

MORRISSEY L., PAYNE J. L., KELSEY D. E. & HAND M. 2011 Grenvillian-aged reworking in the North Australian Craton, central Australia: constraints from geochronology and modelled phase equilibria, *Precambrian Research,* vol. X.

MYERS J. S., SHAW R. D. & TYLER I. M. 1996 Tectonic evolution of Proterozoic Australia, *Tectonics,* vol. 15, no. 6, pp. 1431-1446.

NEUMANN N. L. & FRASER G. L. 2007 Geochronological synthesis and Time-Space plots for Proterozoic Australia. Canberra: Australian Government, Geoscience Australia.

OFFE L. A. & SHAW R. D. 1983 Alice Springs Region, Northern Territory. 1:100 000 Map Commentary, *Bureau of mineral resources, Geology and Geophysics*.

OLIVER N. H. S., HOLCOMBE R. J., HILL E. J. & PEARSON P. J. 1991 Tectono-metamorphic evolution of the Mary Kathleen Fold Belt, northwest Queensland: A reflection of mantle plume processes?, *Australian Journal of Earth Sciences,* vol. 38, pp. 425-455.

PARRISH R. R. 1990 U-Pb dating of monazite and its application to geological problems, *Canadian Journal of Earth Sciences,* vol. 27, no. 11, pp. 1431-1450.

PAYNE J. L., FERRIS G., BAROVICH K. M. & HAND M. 2010 Pitfalls of classifying ancient magmatic suites with tectonic discrimination diagrams: An example from the Paleoproterozoic Tunkillia Suite, southern Australia., *Precambrian Research,* vol. 177, pp. 227-240.

PAYNE J. L., HAND M., BAROVICH K. M., REID A. & EVANS D. A. D. 2009 Correlations and reconstruction models for the 2500-1500 Ma evolution of the Mawson Continent, *Geological Society of London, Special Publications,* vol. 323, pp. 319-355.

PAYNE J. L., HAND M., BAROVICH K. M. & WADE B. P. 2008 Temporal constraints on the timing of high-grade metamorphism in the northern Gawler Craton; implications for assembly of the Australian Proterozoic, *Australian Journal of Earth Sciences,* vol. 55, pp. 623-640.

POWELL R. & HOLLAND T. J. B. 1988 An internally consistent thermodynamic dataset with uncertainties and correlations: 3. Application methods, worked examples and a computer program, *Journal of Metamorphic Geology,* vol. 6, pp. 173-204.

REID A., HAND M., JAGODZINSKI E., KELSEY D. E. & PEARSON N. J. 2008 Paleoproterozoic orogenesis in the southeastern Gawler Craton, South Australia, *Australian Journal of Earth Sciences,* vol. 55, no. 4, pp. 449-471.

ROBERTS M. P. & FINGER F. 1997 Do U-Pb zircon ages from granulites reflect peak metamorphic conditions?, *Geology,* vol. 25, pp. 319-322.

ROBL J., HERGARTEN S., STÜWE K. & HAUZENBERGER C. 2007 THERMAL HISTORY: A new software to interpret diffusive zoning profiles in garnet, *Computers & Geosciences,* vol. 33, pp. 760-772.

RUBATTO D., WILLIAMS I. S. & BUICK I. S. 2001 Zircon and monazite response to prograde metamorphism in the Reynolds Range, central Australia, *Contributions to Mineral Petrology,* vol. 140, pp. 458-468.

SAMBRIDGE M. S. & COMPSTON W. 1994 Mixture modeling of multi-component data sets with application to ion-probe zircon ages, *Earth and Planetary Science Letters,* vol. 128, pp. 373-390.

SANDIFORD M. & HAND M. 1998 Controls on the locus of intraplate deformation in central Australia, *Earth and Planetary Science Letters,* vol. 162, pp. 97-110.

SCHALTEGGER U., FANNING C. M., GÜNTHER D., MAURIN J. C., SCHULMANN K. & GEBAUER D. 1999 Growth, annealing and recrystallization of zircon and preservation of monazite in high-grade metamorphism: conventional and in-situ U-Pb isotope, cathodoluminescence and microchemical evidence, *Contributions to Mineral Petrology,* vol. 134, pp. 186-201.

SCOTT D. L., RAWLINGS D. J., PAGE R. W., TARLOWSKI C. Z., IDNURM M., JACKSON M. J. & SOUTHGATE P. N. 2000 Basement framework and geodynamic evolution of the Palaeoproterozoic superbasins of north-central Australia: an integrated review of geochemical, geochronological and geophysical data, *Australian Journal of Earth Sciences,* vol. 47, pp. 341-380.

SCRIMGEOUR I. R. 2004 A revised province definition and Palaeoproterozoic framework for the Arunta region, central Australia, *Geological Society of Australia (Abstracts),* vol. 73, p. 185.

SCRIMGEOUR I. R., CLOSE D. F. & EDGOOSE C. J. 2005a Mount Leibig Northern Territory (second ed.) 1:250 000 geological map series explanatory notes, *Northern Territory Geological Survey, Darwin.*

SCRIMGEOUR I. R., KINNY P. D., CLOSE D. F. & EDGOOSE C. J. 2005b High-T granulites and polymetamorphism in the southern Arunta Region, central Australia: Evidence for a 1.64 Ga accretional event, *Precambrian Research,* vol. 142, pp. 1-27.

SELWAY K., HAND M., HEINSON G. & PAYNE J. L. 2009 Magnetotelluric constraints on subduction polarity: Reversing reconstruction models for Proterozoic Australia.

SELWAY K., HEINSON G. & HAND M. 2006 Electrical evidence of continental accretion: steeply dipping crustal-scale conductivity contrast, *Geophysical Research Letters,* vol. 33.

SEYDOUX-GUILLAUME A.-M., PAQUETTE J.-L., WIEDENBECK M., MONTEL J.-M. & HEINRICH W. 2002 Experimental resetting of the U-Th-Pb systems in monazite, *Chemical Geology,* vol. 191, pp. 165-181.

SHAW R. D. & BLACK L. P. 1991 The history and tectonic implications of the Redbank Thrust Zone, central Australia, based on structural, metamorphic and Rb-Sr isotopic evidence, *Australian Journal of Earth Sciences,* vol. 38, pp. 307-332.

SHAW R. D. & LANGWORTHY A. P. 1984 Strangways Region, Northern Territory. 1:100 000 Map Commentary, *Bureau of Mineral Resources Australia, Canberra.*

SHAW R. D., LANGWORTHY A. P., OFFE L. A., STEWART A. J., ALLEN A. R. & SENIOR B. R. 1979 Geological report on 1:100 000 scale mapping of the southern Arunta Block, Northern Territory, *Bureau of Mineral Resources Australia Record 1979/47*.

SHAW R. D., ZEITLER P. K., MCDOUGALL I. & TINGATE P. R. 1992 The Paleozoic history of an unusual intracratonic thrust belt in central Australia based on 40Ar/39Ar, K-Ar and fission-track dating, *Journal of the Geological Society,* vol. 149, pp. 937-954.

SLÁMA J., KOŠLER J., CONDON D. J., CROWLEY J. L., GERDES A., HANCHAR J. M., HORSTWOOD S. A., MORRIS G. A., NASDALA L., NORBERG N., SCHALTEGGER U., SCHOENE B., TUBRETT M. N. & WHITEHOUSE M. J. 2008 Plešovice zircon- A new natural reference material for U-Pb and Hf isotopic microanalysis, *Chemical Geology,* vol. 249, pp. 1-35.

SMITH H. A. & BARREIRO B. 1990 Monazite U-Pb dating of staurolite grade metamorphism in pelitic schists, *Contributions to Mineral Petrology,* vol. 105, pp. 602-615.

SMITHIES R. H., HOWARD H. M., EVINS P. M., KIRKLAND C., KELSEY D. E., HAND M., WINGATE M., T. D., COLLINS A. S. & BELOUSOVA E. A. 2011 High-temperature granite magmatism, crust-mantle interaction and the Mesoproterozoic intracontinental evolution of the Musgrave Province, central Australia, *Journal of Petrology,* vol. 52, no. 5, pp. 931-958.

TEYSSIER C. 1985 A crustal system in an intracratonic tectonic environment, *Journal of Structural Geology,* vol. 7, pp. 689-700.

TEYSSIER C., AMRI C. & HOBBS B. E. 1988 South Arunta Block: The internal zones of a proterozoic overthrust in central Australia, *Precambrian Research,* vol. 40/41, pp. 157-173.

VERNON R. H. 1996 Problems with inferring P-T-t paths in low-P granulite facies rocks, *Journal of Metamorphic Geology,* vol. 14, pp. 143-153.

WADE B. P., BAROVICH K. M., HAND M., SCRIMGEOUR I. R. & CLOSE D. F. 2006 Evidence for Early Mesoproterozoic arc magmatism in the Musgrave Block, central Australia: Implications for Proterozoic crustal growth and tectonic reconstructions of Australia.

WADE B. P., HAND M., MAIDMENT D., CLOSE D. F. & SCRIMGEOUR I. R. 2008a Origin of metasedimentary and igneous rocks from the Entia Dome, eastern Arunta region, central Australia: a U-Pb LA-ICPMS, SHRIMP and Sm-Nd isotope study, *Australian Journal of Earth Sciences,* vol. 55, pp. 703-719.

WADE B. P., KELSEY D. E., HAND M. & BAROVICH K. M. 2008b The Musgrave Province: Stitching north, west and south Australia, *Precambrian Research,* vol. 166, no. 1-4, pp. 370-386.

WARREN R. G. & SHAW R. D. 1995 Hermansburg, Northern Territory (second ed.) 1:250 000 geological map series explanatory notes, *Northern Territory Geological Survey, Darwin.*

WHITE R. W., POWELL R. & HOLLAND T. J. B. 2007 Progress relating to calculation of partial melting equilibria for metapelites, *Journal of Metamorphic Geology,* vol. 25, pp. 511-527.

WHITEHOUSE M. J. & KEMP A. I. S. 2010 On the difficulty of assigning crustal residence, magmatic protolith and metamorphic ages to Lewisian granulites: constraints from combined in situ U–Pb and Lu–Hf isotopes, *Geological Society of London, Special Publications,* vol. 335, pp. 81-101.

WILLIAMS I. S. 2001 Response of detrital zircon and monazite, and their U-Pb isotopic systems, to regional metamorphism and host rock partial melting, Cooma Complex, south-eastern Australia, *Australian Journal of Earth Sciences,* vol. 48, pp. 557-580.

WILLIAMS I. S., BUICK I. S. & CARTWRIGHT I. 1996 An extended episode of early Mesoproterozoic metamorphic fluid flow in the Reynolds Range, central Australia, *Journal of Metamorphic Geology,* vol. 14, pp. 29-47.

WRIGHT C., GOLEBY B. R., SHAW R. D., COLLINS C. D. N., KENNETT B. L. N. & LAMBECK K. 1992 Seismic structure and continuity of the Redbank Thrust Zone, central Australia, *BMR J. Aust. Geol. Geophys,* vol. 13, pp. 359-368.

WRIGHT C., GOLEBY B. R., SHAW R. D., COLLINS C. D. N., KORSCH R. J., BARTON T., GREENHALGH S. A. & SUGIHARTO S. 1991 Seismic reflection and refraction profiling in central Australia: Implications for understanding the evolution of the Amadeus Basin. In KORSCH R. J. & KENNARD J. eds. Geological and geophysical studies in the Amadeus Basin, central Australia. Australian Bureau of Mineral Resources, Geology and Geophysics, Canberra.

WYBORN L. 1992 Proterozoic granite types in Australia- Implications for lower crust composition, structure and evolution, *Transactions of the Royal Society of Edinburgh, Earth Sciences,* vol. 83.

ZHAO J. & BENNETT V. C. 1995 SHRIMP U-Pb zircon geochronology of granites in the Arunta Inlier, central Australia: implications for Proterozoic crustal evolution, *Precambrian Research,* vol. 71, pp. 17-43.

ZHAO J. & COOPER J. A. 1992 The Atnarpa Igneous Complex, southeast Arunta Inlier, central Australia: implications for subduction at an Early-Mid Proterozoic continental margin, *Precambrian Research,* vol. 56, pp. 227-253.

ZHAO J. & MCCULLOCH M. T. 1993 Sm-Nd mineral isochron ages of Late Proterozoic dyke swarms in Australia-Evidence for 2 distinctive events of mafic magmatism and crustal extension, *Chemical Geology,* vol. 109, pp. 341-354.

--- 1995 Geochemical and Nd isotopic systematics of granites from the Arunta Inlier, central Australia: implications for Proterozoic crustal evolution, *Precambrian Research,* vol. 71, pp. 265-299.

10 TABLE & FIGURE CAPTIONS

Table 1: Summary of samples analysed throughout the study including grid reference, lithological unit, rock type and relationship to defining structures in the region.

Table 2: Representative electron microprobe analyses of Wigley Block samples used in garnet-biotite diffusion-based cooling models and phase equilibria modelling.

Table 3: U-Pb monazite and zircon geochronology and pressure-temperature summary. Weighted average ages are grouped by column based on their geological interpretation. $^{207}Pb/^{206}Pb$ weighted average isotopic ages are stated unless indicated.

Table 4: Summary of existing Grenvillian-aged geochronological data along the southern margin of the Arunta Region used to compile Figure 13. Table adapted from Morrissey *et al.* (2011).

Figure 1: Simplified geological map showing the location of the Aileron Province, Warumpi Province and the Irindina Province with respect to the Arunta Region, central Australia (adapted from Scrimgeour *et al.* 2005b). The study largely focuses on the fault bounded Wigley Block in the southern Aileron Province. Faults interpreted to represent the Central Australian Suture, including the Charles River Thrust, Redbank Shear Zone and Desert Bore Shear Zone, are indicated. A solid geology map of the study area demonstrates the spatial extent of Grenvillian-aged U-Pb data obtained throughout the study. The location of the Arunta Region with respect to the Musgrave Province and North Australia Craton are also indicated (adapted from Wade *et al.* 2008b).

Figure 2: Geological map of the primary study region demonstrating the distribution of major lithologies and geological structures within the Wigley Block and Warumpi Province. Two areas of significant interest are highlighted and expanded upon in Figure 3.

Figure 3: Aerial photographs of the (a) central Wigley Block and (b) Hamilton Creek area. Images highlight key structural elements, interpreted foliation trends and sample locations.

Figure 4: Field photographs demonstrating key structural relationships: (a) Delta clast located within an E-W trending ultramylonite zone showing south side up kinematics. (b) S-C fabrics from a partially migmatised mylonite within the E-W trending high strain zone showing south side up kinematics. (c) A strongly foliated migmatised augen gneiss with a near horizontal mineral lineation displaying dextral shear sense. (d) Boudinage formation in a partially migmatised mylonite within the E-W trending high strain zone under an interpreted N-S compressional regime. (e) Felsic melt veins cross cutting the E-W trending fabric of a partially migmatised mylonite. (f) A megacrystic augen gneiss crosscut by a syn-tectonic microgranite possessing a weak foliation parallel to the intense E-W foliation of the augen gneiss. (g) Mafic migmatitic boudins completely enveloped by a syn-tectonic pegmatite demonstrating a pervasive NW-SE foliation parallel to migmatitic layering. (h) 1080 Ma Stuart Dyke cross-cutting the E-W trending mylonitic system in the central Wigley Block.

Figure 5: Photomicrographs of key petrological relationships: (a) AS2010-65J: Garnet porphyroblasts wrapped by a fabric comprising of biotite and prismatic sillimanite. Coarse-grained biotite is growing in the pressure shadow of garnet grains. (b) AS2010-65J: Sillimanite growing in the biotite matrix and occurring as randomly oriented inclusions within quartz. Sillimanite mats possess a fracture fabric which terminates in the quartz host. (c) AS2010-66D: Coarse-grained prismatic sillimanite intergrown with the intensely foliated biotite-sillimanite fabric. (d) AS2010-67A2: Garnet porphyroblast completely enveloped by coarse-grained biotite. Sillimanite is highly pervasive and defines an internal foliation orthogonal to the external fabric. (e) RED2011-01: Coarse-grained biotite-sillimanite fabric containing abundant monazite. Sillimanite mats exhibit

well developed microboudinage, with ilmenite filling the boudin necks. (f) AS2010-63D: Texturally younger pinitised cordierite containing inclusions of sillimanite, biotie, garnet and microcline. (g) AS09-4: Cordierite corona separating garnet from the enveloping biotite-sillimanite fabric. The cordierite corona contains K-feldspar and monazite. (h) AS2010-72D: Very fine-grained mylonitic fabric comprising of intensely layered recrystallised quartz ribbons and biotite. Inclusions of microcline and plagioclase possess recrystallised tails that give kinematics.

Figure 6: Calculated P-T pseudosection for sample AS2010-65J. The bulk composition is shown above. The numbered list of mineral assemblages corresponds to the numbered fields in the diagram. Assemblage variance 'v' is indicated in each field. The bold lines represent the aluminosilicate stability fields. Garnet compositional isopleths for calcium (X_{Ca}) are plotted in the peak field and are represented by a small spaced dashed black line. The isopleths that are bolded bound the core compositional range of garnets and are interpreted to represent the peak conditions. The modal proportions of garnet are plotted in the peak field and are represented by a large spaced dashed black line. The diffusional closure temperature of a small garnet core from the central Wigley Block is represented by small spaced dashed white line at 780 °C. The white dashed arrow represents the interpreted P-T path based on the change in garnet composition from core to rim and dated reaction textures observed within AS2010-63 and AS09-04 in the central Wigley Block.

Figure 7: (b) Chemical zoning profile from a single garnet grain (a) in sample AS2010-66D. (c) Diffusional based cooling estimate for sample AS2010-66D which best satisfies the chemical zoning pattern observed in the garnet core based on the cooling history of Dodson (1986). X_{Mg} ranges from 0.195 in the core to 0.106 in the rim. The subsequent closure temperature of the garnet core is highlighted and is interpreted to represent the minimum peak temperature during resetting in the Grenvillian.

Figure 8: *In situ* LA-ICPMS monazite U-Pb geochronology. The ages shown next to the BSE images are $^{207}Pb/^{206}Pb$ ages. (a) AS2010-63D: Concordia plot of 22 monazite analyses with the weighted average of the old and young age population given. (b) AS2010-63D: BSE images of monazite grains located within biotite

and quartz respectively. (c) AS2010-65J: Concordia plot of 18 monazite analyses with weighted average age of the young population given. (d) AS2010-65J: BSE images of monazite grains located along the grain boundary of garnet and within the fabric respectively. (e) AS2010-66D: Concordia plot of 43 monazite analyses with the weighted average of the old and young age population given. (f) AS2010-66D: BSE images of monazite grains located along the grain boundary of biotite and within the foliated matrix respectively.

Figure 9: *In situ* LA-ICPMS monazite U-Pb geochronology. The ages shown next to the BSE images are $^{207}Pb/^{206}Pb$ ages: (a) AS2010-66J: Concordia plot of 29 monazite analyses with the weighted average age of the young population given (b) AS2010-66J: BSE images of mounted monazite grains. (c) AS2010-67A2: Concordia plot of 24 monazite analyses with the weighted average age of the old and young population given. (d) AS2010-67A2: BSE images of monazite grains located within biotite and along the grain boundary of biotite within the fabric respectively. (e) AS2010-72D: Concordia plot of 28 monazite analyses with the weighted average age given. (f) AS2010-72D: BSE images of monazite grains located within the mylonitic fabric.

Figure 10: *In situ* monazite and zircon LA-ICPMS U-Pb geochronology. The ages shown next to the BSE and CL images are $^{207}Pb/^{206}Pb$ ages: (a) RED2011-01: Concordia plot of 19 monazite analyses with the weighted average age given. (b) RED2011-01: BSE images of monazite grains located within biotite in the fabric (c) AS2010-64J: Concordia plot of 48 zircon analyses with the weighted average ages given for the igneous population (blue) and metamorphic population (red). (d) AS2010-64J: CL images of a moderately luminescent oscillatory zoned igneous zircon and an igneous zircon with a fuzzy metamorphic core respectively. (e) COL2011-01: Concordia plot of 38 zircon analyses with the weighted average age given. (f) COL2011-01: CL images of moderately luminescent oscillatory zoned zircons.

Figure 11: LA-ICPMS zircon and monazite U-Pb geochronology. The ages shown next to the CL images are $^{207}Pb/^{206}Pb$ ages: (a) HAM2011-02: Concordia plot of 33 zircon analyses with the weighted average age of the young population given. (b) HAM2011-02: CL images of zircons exhibiting chaotic metamict cores and

weakly luminescent oscillatory zoned rims. (c) HAM2011-08: Concordia plot of 35 zircon analyses with the weighted average age of the old and young population given. (d) HAM2011-08: CL images of zircon grains exhibiting highly and weakly luminescent oscillatory zoning respectively. (e) AS09-4: Concordia plot of 37 monazite analyses with the weighted average age of the young population given.

Figure 12: LA-ICPMS detrital zircon U-Pb geochronology. The ages shown next to the CL images are $^{207}Pb/^{206}Pb$ ages. (a) AS2010-62D: Concordia plot of detrital zircon population with 95-105% concordancy. (b) AS2010-62D: Age spectra plot of detrital zircons grains, demonstrating all data (light grey) and 95-105% concordant data (dark grey). (c) CL images of zircon grains from the youngest spread of ages exhibiting (1) moderately luminescent oscillatory zoning, (2) textured 'soccer ball' morphologies and (3) transgressive metamorphic overgrowths. (d) AS2010-59 J: Concordia plot of detrital zircon population with 95-105% concordancy. (e) AS2010-59J: Age spectra plot of detrital zircon sample AS2010-59J, demonstrating all data (light grey) and 95-105% concordant data (dark grey). (e) AS2010-59J: CL images of zircon grains from the youngest age population exhibiting (1) textured 'soccer ball' morphologies, (2) weakly luminescent oscillatory zoning and (3) highly luminescent oscillatory zoning.

Figure 13: Simplified geological map of the Arunta region, adapted from Scrimgeour *et al.* (2005b) and Morrissey et al. (2011), demonstrating the spatial extent of Grenvillian-aged reworking along the southern margin of the Arunta Region. Sample type, geochronological method and references used to compile the map are presented in Table 4.

Figure 14: 3D diagram demonstrating the correlation between surficial E-W trending structures along the southern margin of North Australia Craton and the suture trend of the Redbank Shear Zone and the interpreted boundary between the North Australia Craton and Warumpi Province imaged by magnetotellurics (MT). The white stars indicate the locations of Grenvillian-aged data associated with deformation. The larger scale MT image demonstrates the location of the Warumpi Province MT transect with respect to significant lithospheric scale geological features including the Amadeus Basin and the interpreted fossilised subduction zone between

the North Australia Craton and the Warumpi Province. It is noted that the Warumpi Province MT line imaged by Selway *et al.* (2006) was not collected along the exact surface transect demonstrated in the figure and is purely intended to provide insight into the sub-surface geology beneath the southern Aileron Province. Figure adapted from Selway *et al.* (2006, 2009).

11 TABLES

Table 1: Summary of samples

SAMPLE	LOCATION (53 J)	UNIT	LITHOLOGY	FIELD RELATIONSHIPS
AS2010-59J	0382856 7388399	Unnamed Paleoproterozoic bt-gt gneisses	gt-bi-sill migmatitic metapelite	Sample is located within an older fabric which trends into the E-W trending high strain belt. The fabric possesses a shallow westerly plunging mineral lineation is cross cut by pegmatitic melt segregations.
AS2010-62D	0381019 7386876	Unnamed Paleoproterozoic bt-gneisses	gt migmatitic metapelite	Sample is located within an older fabric which trends into the E-W trending high strain belt. The migmatitic veins are deformed into lenses.
AS2010-63D	0380898 7387482	Unnamed Paleoproterozoic bt-gneisses	cd-sill-bi-gt quartzitic gneiss	Sample is located within an older fabric which trends into the E-W high strain belt. Gneiss has a shallow northerly plunging lineation with an L tectonic fabric.
AS2010-64J	0384206 7389096	Unnamed Paleoproterozoic bt-gneisses	Augen Gneiss	Sample is located within the E-W trending high strain belt and exhibits an L-S tectonic fabric. Augen gneiss exhibits melt veins parallel and oblique to the fabric. Augen exhibit good dextral shear sense.
AS2010-65J	0385454 7389461	Unnamed Paleoproterozoic bt-gneisses	gt-bi-sill migmatitic metapelite	Sample is located within the E-W trending high strain belt and exhibits stromatic leucosomal segregations. Metapelite possesses a shallow westerly plunging lineation defined by sillimanite.
AS2010-66D	0382933 7386196	Charles River Gneiss	gt-bi-sill migmatitic gneiss	Sample is located within an older fabric which trends into the E-W high strain belt and is intensely lineated with a shallow westerly plunge.
AS2010-66J	0385454 7389461	Unnamed Paleoproterozoic bt-gneisses	Syn-tectonic microgranite	Sample is located within the E-W trending high strain belt and cross-cuts the L-S tectonic fabric of AS2010-64 (July). Granite is folded and foliated parallel to the gneissic fabric.
AS2010-67A2	0383622 7386185	Charles River Gneiss	gt-bi-sill migmatitic metapelite	Sample is located within an older fabric which trends into the E-W high strain belt and contains s-vergent tight to isoclinal folds.
AS2010-72D	0385790 7388832	Unnamed Paleoproterozoic bt-gneisses	Ultramylonite	Sample is located in an >60 m wide E-W trending shear zone. Mylonitisation is more intense towards the centre of the zone. Sigma and delta clasts demonstrate south-side up movement.
COL2011-01	0384206 7389096	Unnamed Paleoproterozoic bt-gneisses	Migmatitic leucosome	Sample is located within the E-W trending high strain belt and is parallel to the fabric of sample AS2010-64 (July). Leucosomes are folded.
HAM2011-02	0330270 7388919	Unnamed Paleoproterozoic migmatitic orthogneiss	Syn-tectonic pegmatite	Sample is located within the strain shadow of a kilometre scale boudin. Pegmatite completely envelops migmatitic boudins and is foliated parallel to the migmatitic fabric.
HAM2011-08	0329884 7390901	Unnamed Paleoproterozoic bt-gneisses	Migmatitic melt vein	Sample is located within the strain shadow of a kilometre scale boudin. Migmatitic vein is parallel to the foliation.
RED2011-01	0275184 7397376	Teapot Granite Complex	gt-bi-sill metapelite	Sample is located along the strike of the E-W trending high strain belt in the Central Wigley Block and contains shallow westerly plunging open folds.

Table 2: Representative Electron Microprobe analyses

	AS09-3					**AS2010-59J**			**AS2010-60B**				**AS2010-65J**		**AS2010-66D**			**AS2010-67A2**			
	gt core	gt rim	bi	pl	mt	gt core	gt rim	bi	gt core	gt rim	bi	mt	gt core	gt rim	gt core	gt rim	bi	gt core	gt rim	bi	pl
SiO2	36.71	36.479	33.98	59.2	0.12	37.14	35.59	34.77	37.31	36.72	34.85	0.13	37.03	36.51	35.99	35.4	33.53	36.22	36.2254	34.1892	62.26
TiO2	0.02	0.042	3.28	0.08	0.05	0.03	0.08	2.6	0.02	0.03	2.51	0.02	0.03	0.05	0	0.03	1.88	0	0.0448	3.1258	0
Al2O3	21.41	21.2582	18.15	25.66	0	21.56	20.36	17.86	21.42	21.15	19.7	0.54	20.97	20.72	21.64	21.03	17.73	20.78	21.25	17.9077	22.48
Cr2O3	0.01	0.01	0.04	0.02	0	0	0	0.01	0.03	0	0.04	0	0	0.01	0	0	0.02	0	0.0114	0.0566	0.01
FeO	33.34	35.8779	18.73	0	60.39	33.89	36.89	19.1	33.68	33.06	18.21	88.95	1.79	1.23	33.98	35.2	19.06	34.31	36.1844	21.338	0.3
MnO	0.96	1.3238	0.02	0	0	0.83	1.61	0.04	1.81	5.06	0.05	0.06	33.48	36.22	1.26	3.76	0.13	0.79	1.4849	0.0475	0
MgO	5.66	3.3902	10.25	0.05	0	5.61	2.4	9.79	4.99	2.08	8.93	0	1.06	1.64	5.11	2.72	11.7	4.85	3.0832	8.4097	0
ZnO	0.02	0.027	0.01	0	0.05	0.07	0.03	0	0.06	0.17	0	0	4.34	2.24	0	0	0	0	0.0042	0.0387	0.03
CaO	1.59	1.0057	0.06	5.32	0.01	1.16	1.03	0.05	1.21	1.09	0.02	0.02	1.49	1.3	1.34	1.36	0.01	1.01	0.9747	0.0448	3.12
Na2O	0	0.0003	0.11	7.4	0.1	0.04	0	0.1	0.04	0.04	0.14	0.02	0.02	0.01	0.01	0.01	0.07	0.03	0.0003	0.1046	9.38
K2O	0	0.0387	9.17	0.05	0	0.01	0.03	9.01	0	0.05	8.29	0	0.01	0.04	0.02	0.03	9.4	0	0.0188	5.788	0.01
Total	99.72	99.54	93.88	97.78	60.75	100.4	98.03	93.5	100.59	99.49	92.77	89.83	100.22	100.08	99.41	99.62	93.56	98.16	99.29	91.11	97.6
No. Oxygens	12	12	11	8	4	12	12	11	12	12	11	4	12	12	12	12	11	12	12	11	8
Si	2.93	2.96	2.63	2.68	0.01	2.95	2.96	2.7	2.96	2.99	2.69	0.01	3.01	2.98	2.9	2.9	2.62	2.96	2.952	2.703	2.81
Ti	0	0	0.19	0	0	0	0.01	0.15	0	0	0.15	0	0	0	0	0	0.11	0	0.003	0.186	0
Al	2.02	2.03	1.66	1.37	0	2.02	2	1.63	2.01	2.03	1.79	0.03	2.01	1.99	2.06	2.03	1.63	2	2.041	1.668	1.2
Cr	0	0	0	0	0	0	0	0	0	0	0	0	0	0	0	0	0	0	0.001	0.004	0
Fe2+	2.23	2.43	1.21	0	3.96	2.25	2.57	1.24	2.24	2.25	1.18	3.92	0.12	0.08	2.29	2.42	1.24	2.34	2.465	1.41	0.01
Mn2+	0.06	0.09	0	0	0	0.06	0.11	0	0.12	0.35	0	0	2.31	2.5	0.09	0.26	0.01	0.05	0.102	0.003	0
Mg	0.67	0.41	1.18	0	0	0.66	0.3	1.13	0.59	0.25	1.03	0	0.13	0.2	0.61	0.33	1.36	0.59	0.375	0.991	0
Zn	0	0	0	0	0	0	0	0	0	0.01	0	0	0.26	0.13	0	0	0	0	0	0.002	0
Ca	0.14	0.09	0	0.26	0	0.1	0.09	0	0.1	0.1	0	0	0.13	0.11	0.12	0.12	0	0.09	0.085	0.004	0.15
Na	0	0	0.02	0.65	0.01	0.01	0	0.02	0.01	0.01	0.02	0	0	0	0	0	0.01	0	0	0.016	0.82
K	0	0	0.91	0	0	0	0	0.89	0	0.01	0.82	0	0	0	0	0	0.94	0	0.002	0.584	0
Total Cations	8.06	8.02	7.81	4.96	3.99	8.04	8.04	7.78	8.03	8	7.68	3.97	0	0	8.07	8.08	7.93	8.04	8.03	7.57	5
Xmg	0.23	0.14	0.49	0.97	0	0.23	0.1	0.48	0.21	0.1	0.47	0	0	0	0.21	0.12	0.52	0.2	0.13	0.41	0
Xna				0.713																	0.844
X(alm)	0.72	0.81	0.81			0.73	0.84		0.73	0.76			0.05	0.03	0.74	0.77		0.76	0.81		
X(py)	0.22	0.09	0.14			0.22	0.1		0.19	0.09			0.05	0.07	0.2	0.11		0.19	0.12		
X(grs)	0.04	0.06	0.03			0.03	0.03		0.03	0.03			0.05	0.04	0.04	0.04		0.03	0.03		
X(spss)	0.02	0.04	0.03			0.02	0.04		0.04	0.12			0.86	0.86	0.03	0.08		0.02	0.03		

Table 3: U-Pb monazite and zircon geochronology and P-T Summary

	Metamorphism	Magmatism	Metamorphism	Metamorphism	Maximum Depositional Ages	P-T conditions (P kbars, T°C)
In situ U-Pb monazite LA-ICPMS						
AS2010-63 (Dec)				1090 ± 15 Ma		
AS2010-65 (July)				1128 ± 12 Ma		7.9-9.3, 775-830
AS2010-66 (Dec)	1720 ± 17 Ma			1091.9 ± 5.4 Ma ($^{207}Pb/^{235}U$)		
AS2010-67A2	1598 ± 26 Ma			1127 ± 20 Ma		
AS2010-72 (Dec)				1129.4 ± 7.9 Ma		
RED2011-01				1141.9 ± 9.9 Ma		
AS09-4*				1119 ± 7.4 Ma		
U-Pb monazite LA-ICPMS						
AS2010-66 (July)				1116 ± 8.3Ma		
U-Pb zircon LA-ICPMS						
AS2010-64 (July)		1649.7 ± 6.7 Ma	1637 ± 13 Ma			
COL2011-01			1636.8 ± 6.5 Ma			
HAM2011-02				1137.4 ± 8.1 Ma		
HAM2011-08		1626.2 ± 7.2 Ma		1139 ± 19 Ma		
AS2010-62 (Dec)					1835 ± 20 Ma	
AS2010-59 (July)					1823 ± 9.7 Ma	

* Cutts *et al.* (personal communication, April 2011)

Table 4: Distribution of Grenvillian-aged reworking in the Arunta Region

	STUDY	GEOCHRONOLOGY METHOD	ROCK TYPE	AGE (MA)
A	This study	Monazite	Metapelites incorporated within the Charles River Gneiss and unnamed Paleoproterozoic gneisses of the central Wigley Block	1090 ± 15 1128 ± 12 1091.9 ± 5.4 1127 ± 20 1129.4 ± 7.9
			Syn-tectonic microgranite	1116 ± 8.3
B	This study	Zircon	Pegmatite	1137.4 ± 8.1
		Zircon	Migmatitic melt vein	1139 ± 19
C	This study	Monazite	E-W trending metapelite incorporated within the Teapot Granite	1141.9 ± 9.9
D	Morrissey *et al.* 2011	Monazite Monazite Monazite Sm-Nd garnet Sm-Nd garnet	Chewings Range metapelite (N directed fabric overprinted by upright folds)	1129 ± 11 1121 ± 7.2 1159 ± 24 1100 ± 22 1141 ± 22
E	Morrissey *et al.* 2011	Monazite	Simpson Gap Metapelites (interlayered with N directed fabric in Rungutjirba Gneiss)	1139 ± 13
F	Morrissey *et al.* 2011	Monazite Monazite	Teppa Hill Metamorphics (S directed, flat lying fabric)	1146 ± 21 1120 ± 9.1
G	Black & Shaw 1995	Zircon	Teapot Granite (felsic granite)	1136 ± 6
H	Collins *et al.* 1995	Rb-Sr	Ormiston Pound Granite (recrystallised)	1100-1130
I	Scrimgeour *et al.* 2005b	Zircon	Locally migmatised Kakalyi Gneiss	1149 ± 3
J	Biermeier *et al.* 2003a	Monazite rims	Mylonitised amphibolite to granulite facies metapelites	1139 ± 25
K	Shaw & Black 1991	Rb-Sr	Pegmatite	1140 ± 56
L	Claoué-Long & Hoatson 2005	Zircon	Undeformed ultramafic alkaline Mordor Complex	1133 ± 5
M	Close *at al.* 2007	Detrital zircon	Casey Inlier cover sequence: Upper greenschist schistose fabric constrained between 1235 and 830 Ma	Between 1235 and 830

Table adapted from Morrissey *et al.* (2011)

Figure 1.

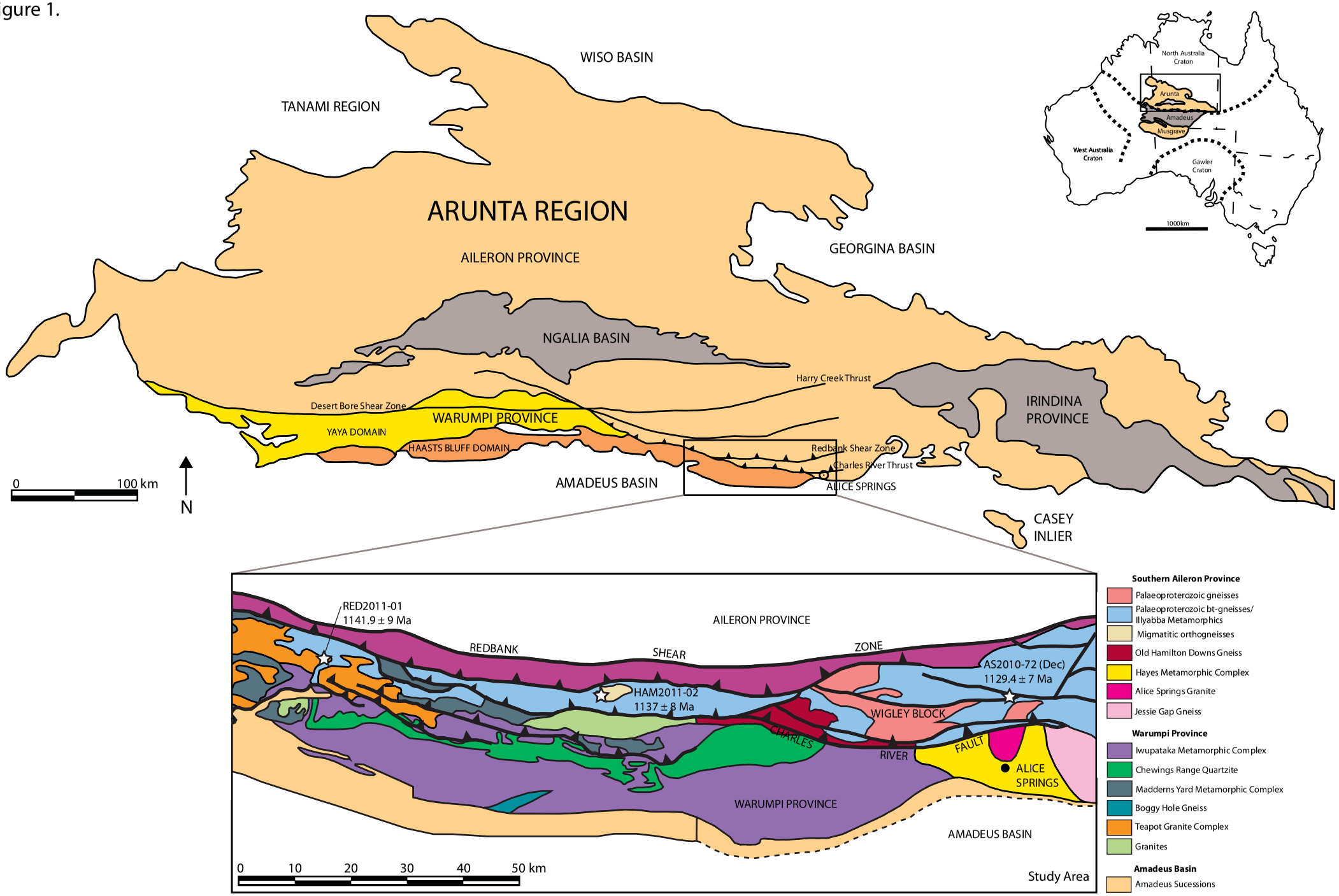
WISO BASIN
TANAMI REGION
ARUNTA REGION
AILERON PROVINCE
GEORGINA BASIN
NGALIA BASIN
Harry Creek Thrust
Desert Bore Shear Zone
WARUMPI PROVINCE
YAYA DOMAIN
HAASTS BLUFF DOMAIN
IRINDINA PROVINCE
Redbank Shear Zone
Charles River Thrust
ALICE SPRINGS
AMADEUS BASIN
CASEY INLIER
0
100 km
N
North Australia Craton
Arunta
Amadeus
Musgrave
West Australia Craton
Gawler Craton
1000km
RED2011-01
1141.9 ± 9 Ma
AILERON PROVINCE
REDBANK
SHEAR
ZONE
HAM2011-02
1137 ± 8 Ma
AS2010-72 (Dec)
1129.4 ± 7 Ma
WIGLEY BLOCK
CHARLES
RIVER
FAULT
ALICE SPRINGS
WARUMPI PROVINCE
AMADEUS BASIN
0
10
20
30
40
50 km
Study Area
Southern Aileron Province
Palaeoproterozoic gneisses
Palaeoproterozoic bt-gneisses/ Illyabba Metamorphics
Migmatitic orthogneisses
Old Hamilton Downs Gneiss
Hayes Metamorphic Complex
Alice Springs Granite
Jessie Gap Gneiss
Warumpi Province
Iwupataka Metamorphic Complex
Chewings Range Quartzite
Madderns Yard Metamorphic Complex
Boggy Hole Gneiss
Teapot Granite Complex
Granites
Amadeus Basin
Amadeus Sucessions

Figure 2.

GEOLOGY OF THE MACDONNELL RANGES

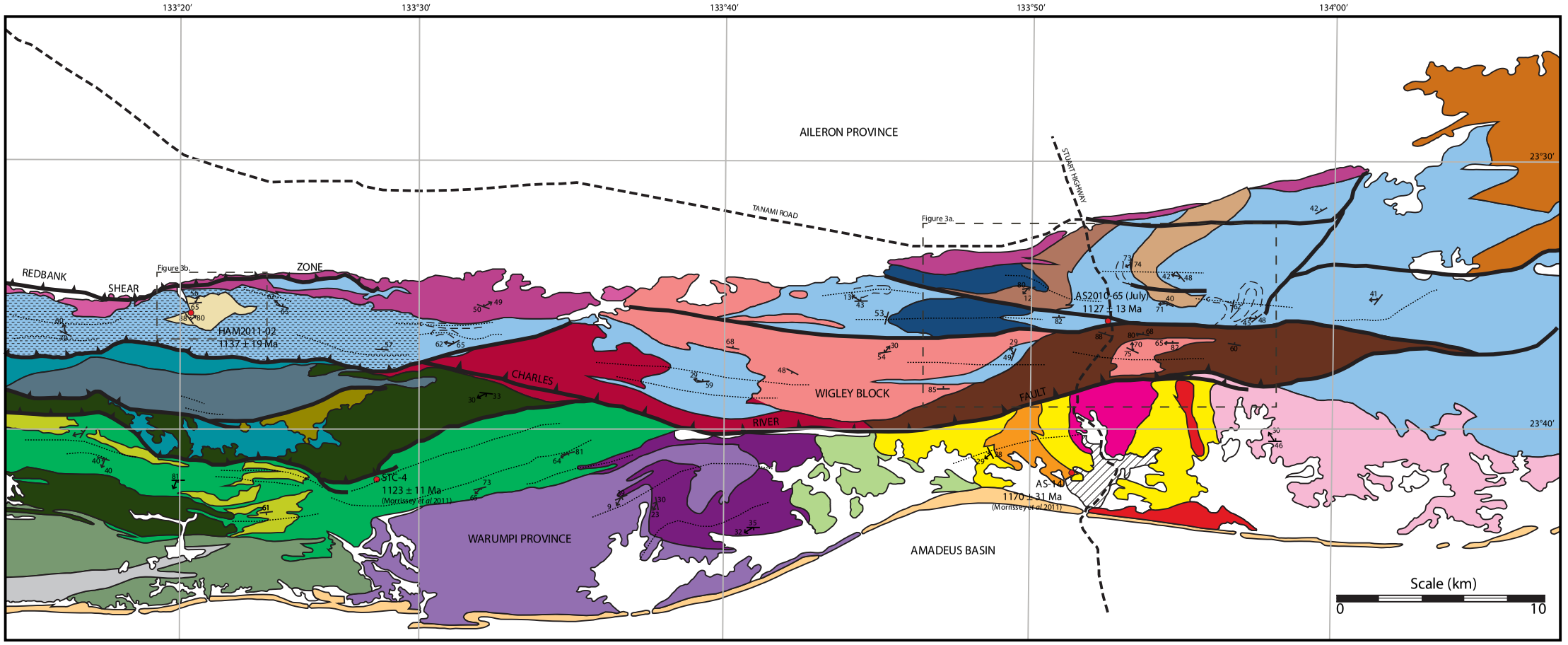

Amadeus Basin

Neoproterozoic Sequences

- Heavitree Quartzite (c. 830 Ma)
- Alice Springs
- Roads
- Faults
- Thrust fault
- Stratigraphic boundary
- Strike and dip of Strata
- Trend and plunge of lineation
- Stratigraphic trend line
- Interpreted fold axial hinge
- Sample location

Warumpi Province

Iwupataka Metamorphic Complex, Early Proterozoic (Arunta Block)

- Burt Bluff Gneiss (c.1605 Ma)
- Rungutjirba Gneiss (c. 1605 Ma)
- Chewings Range Quartzite
- Simpsons Gap Metasediments
- Brinkley Bluff Gneiss
- Ellery Granitic Complex
- Ryans Gap Metamorphics

Madderns Yard Metamorphic Complex, Early Proterozoic (Arunta Block)

- Boggy Hole Gneiss (c. 1650 Ma)
- Palaeoproterozoic Metasediments
- Orthogneiss
- Mesoproterozoic Metasediments

Hayes Metamorphic Complex, Palaeoproterozoic (Arunta Block)

- Sadedeen Range Gneiss
- Teppa Hill Metamorphics
- Emily Gap Schist

Wigley Block, southern Aileron Province

Palaeoproterozoic Metasediments (Arunta Block)

- Palaeoproterozoic bt-gneisses/ Illyabba Metamorphics
- Palaeoproterozoic gt-bi gneisses
- Randall Peak Metamorphics
- Charles River Gneiss
- Flint Springs Gneiss
- Bond Springs Gneiss
- Migmatitic orthogneisses

Middle to Late Proterozoic Metasediments (Arunta Block)

- Redbank Deformed Zone
- Palaeoproterozoic gneisses
- Alice Springs Granite (1750 Ma)
- Jessie Gap Gneiss
- Old Hamilton Downs Gneiss

Figure 3.

(a)

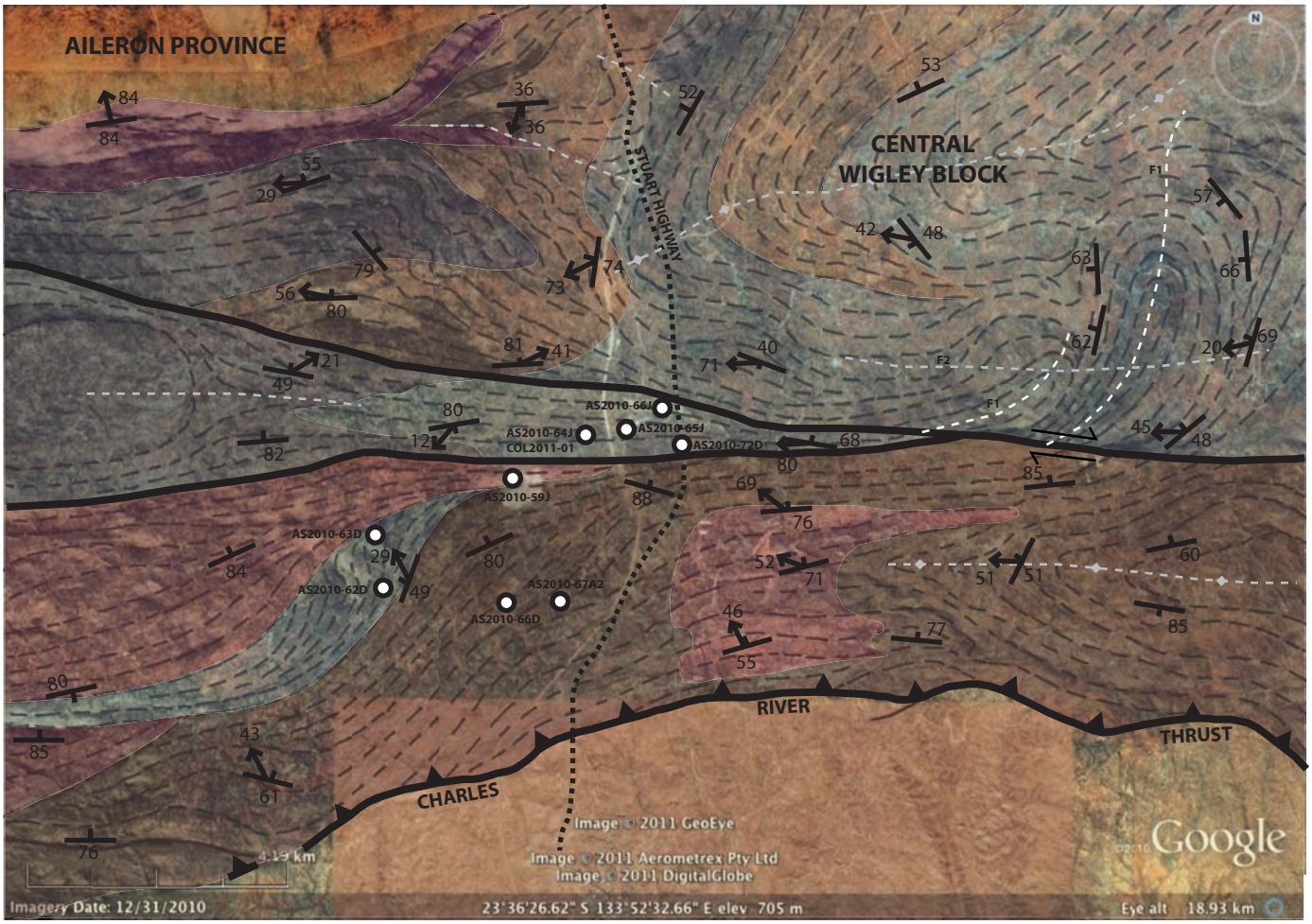

(b)

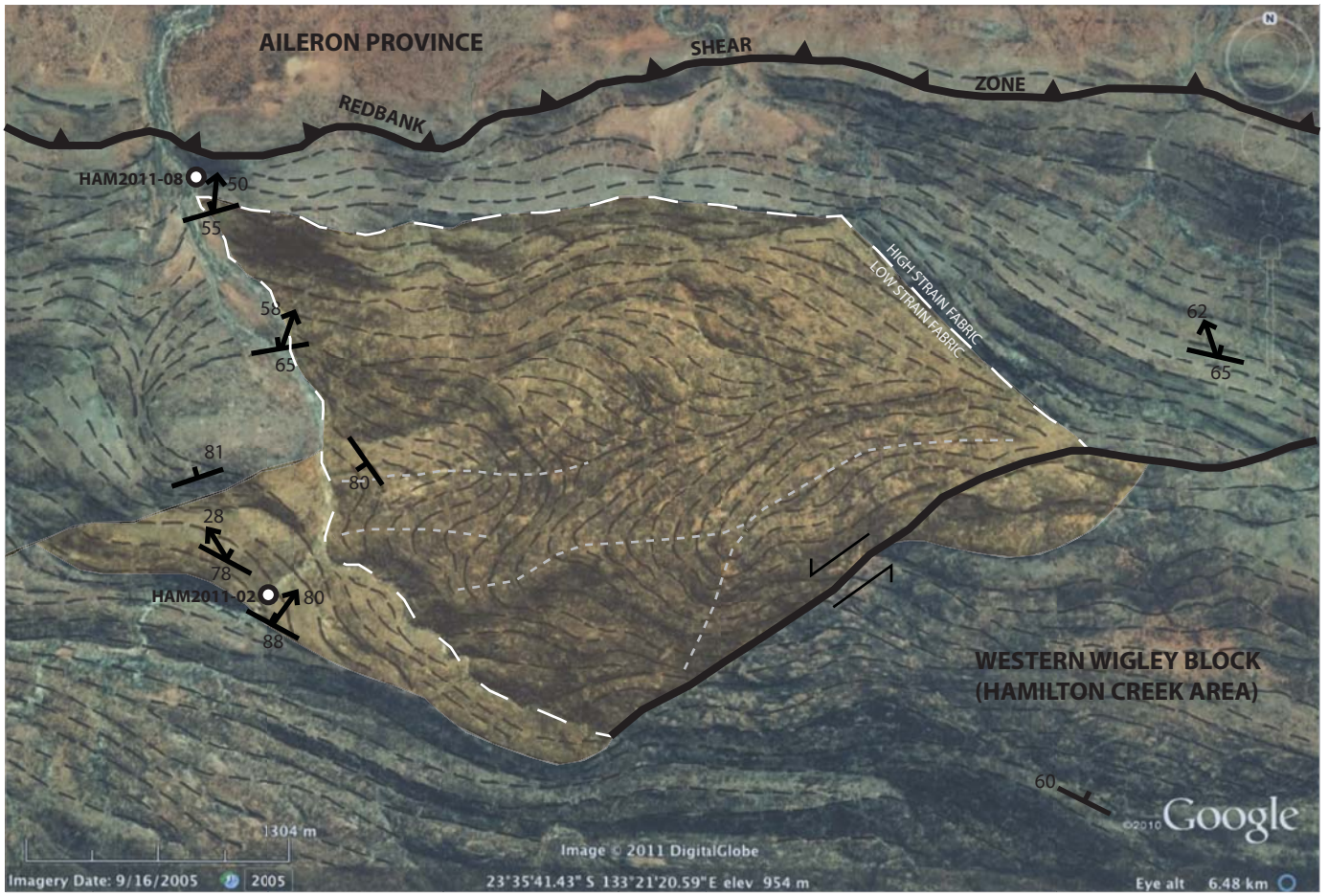

Key

- Sample location
- Dip and strike of strata
- Trend and plunge of lineation
- Fault
- Thrust fault
- Fabric trend line
- Interpreted fold axial hinge
- Anticline
- Displacement
- Palaeoproterozoic bt-gneisses/ Illyabba Metamorphics
- Palaeoproterozoic gt-bi gneisses
- Charles River Gneiss
- Flint Springs Gneiss
- Bond Springs Gneiss
- Migmatitic orthogneiss
- Redbank Deformed Zone
- Palaeoproterozoic gneisses

Figure 4.

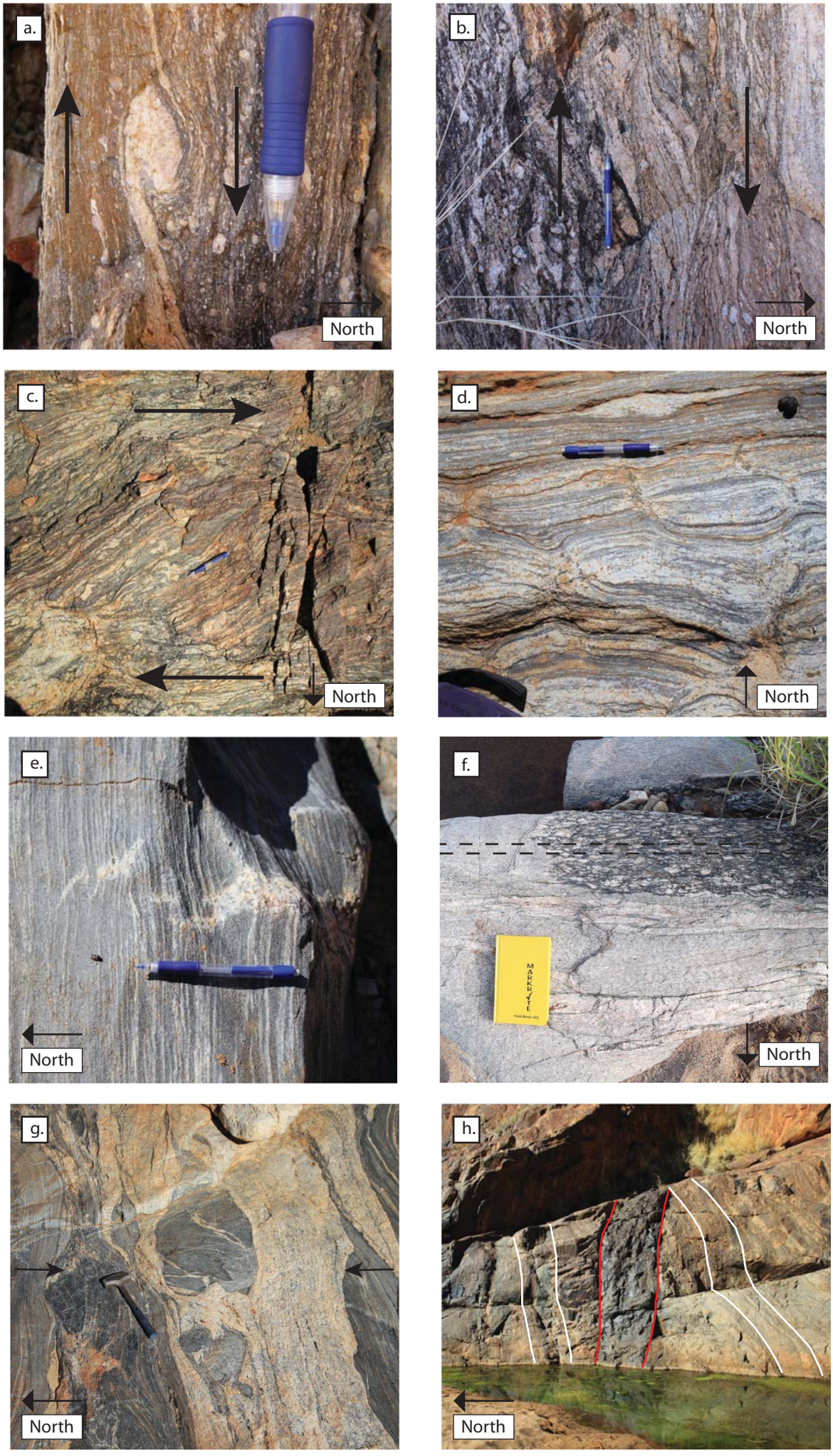

Figure 5.

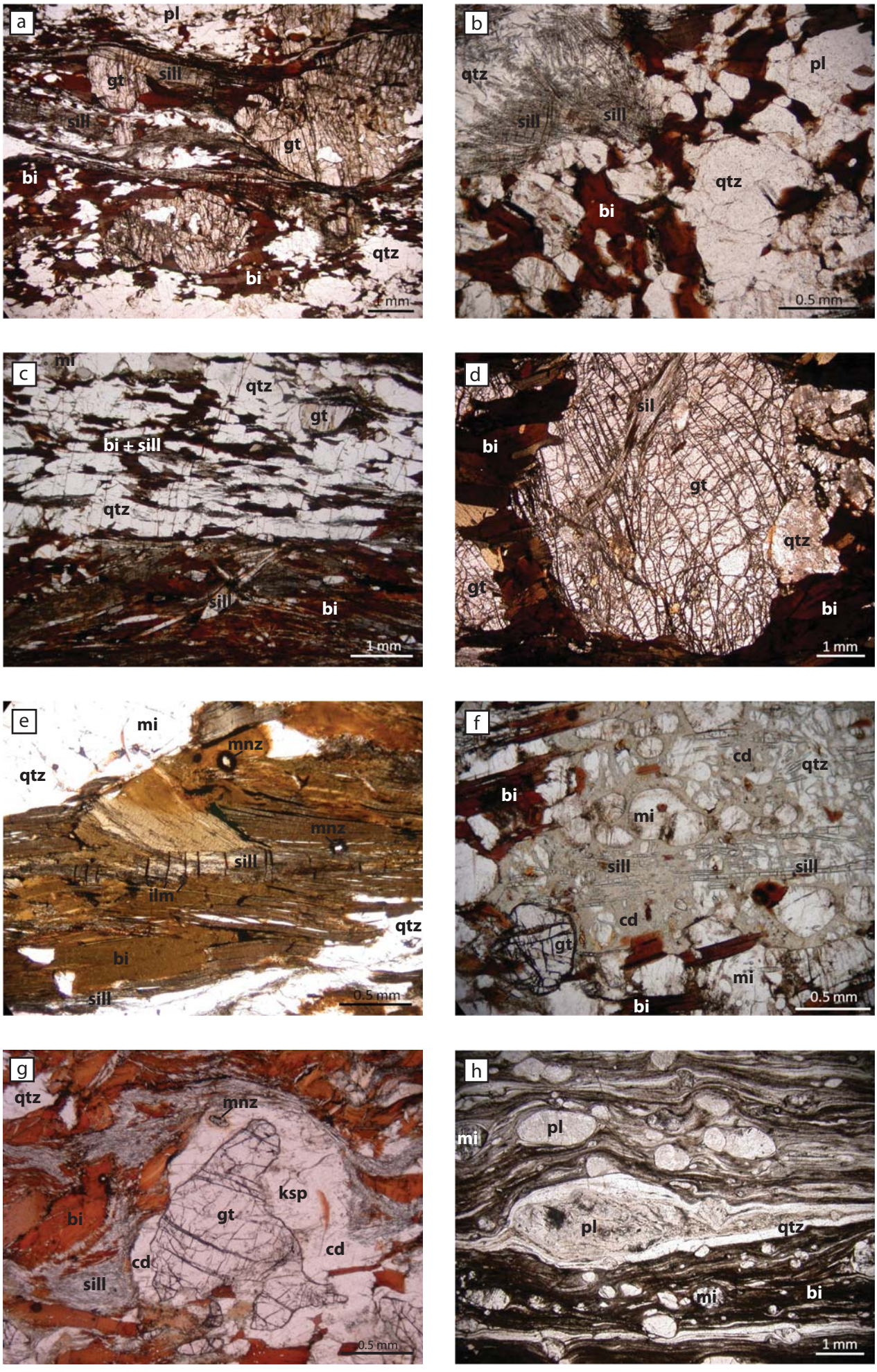
a
pl
gt
sill
sill
gt
bi
qtz
bi
1 mm
b
qtz
pl
sill
sill
qtz
bi
0.5 mm
c
mi
qtz
gt
bi + sill
qtz
sill
bi
1 mm
d
sil
bi
gt
qtz
gt
bi
1 mm
e
mi
mnz
qtz
mnz
sill
ilm
qtz
bi
sill
0.5 mm
f
cd
qtz
bi
mi
sill
sill
cd
gt
mi
bi
0.5 mm
g
qtz
mnz
ksp
bi
gt
cd
cd
sill
0.5 mm
h
mi
pl
pl
qtz
mi
bi
1 mm

Figure 6.

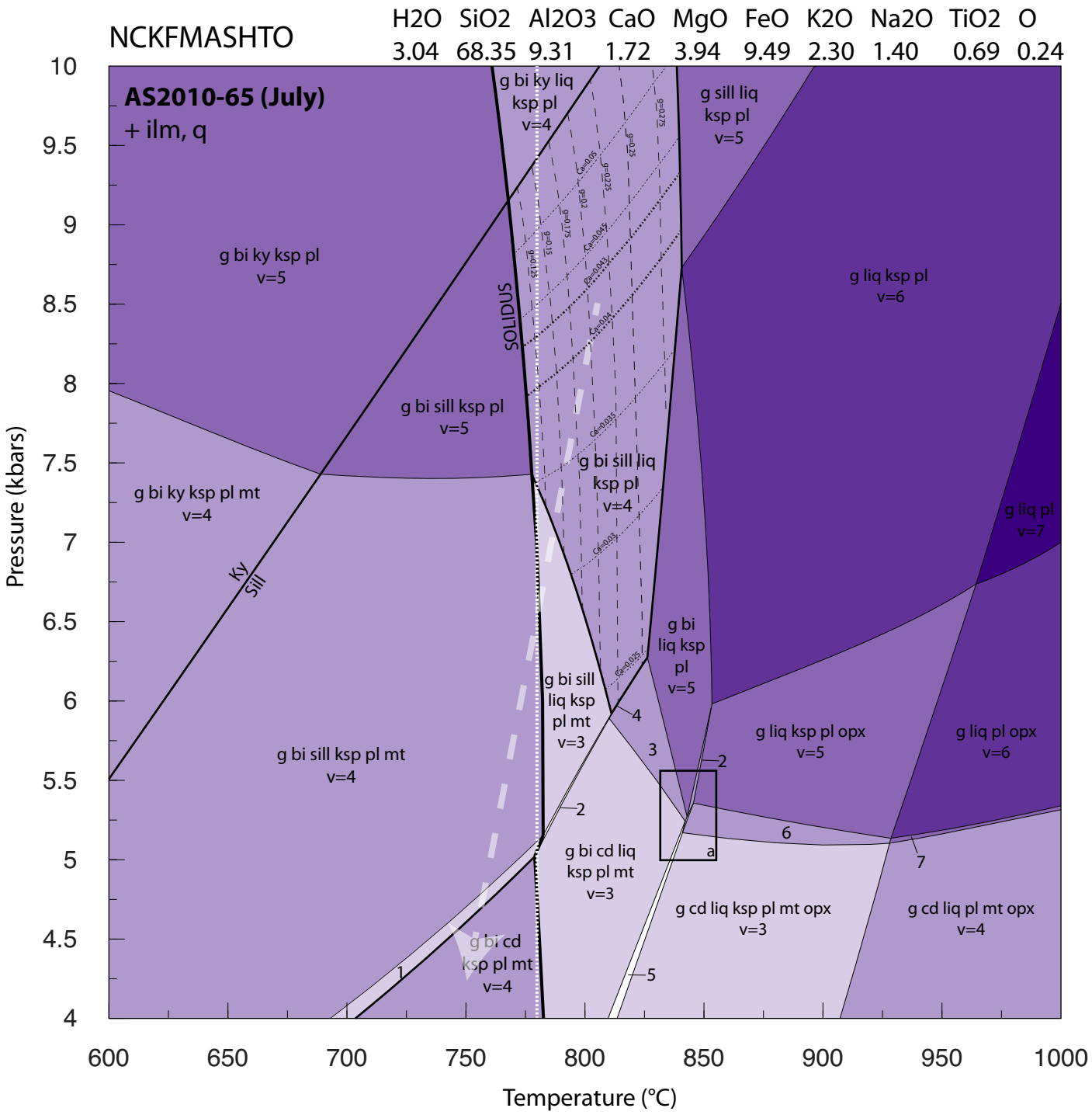

1. g bi sill cd ksp pl mt
2. g bi sill liq cd ksp pl mt
3. g bi liq cd ksp pl
4. g bi sill liq cd ksp pl
5. g bi liq cd ksp pl mt opx
6. g liq cd ksp pl opx
7. g liq cd pl opx
8. g bi liq cd ksp pl opx
9. g bi liq ksp pl opx

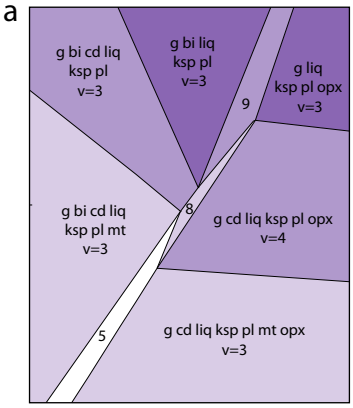

Figure 7.

a)

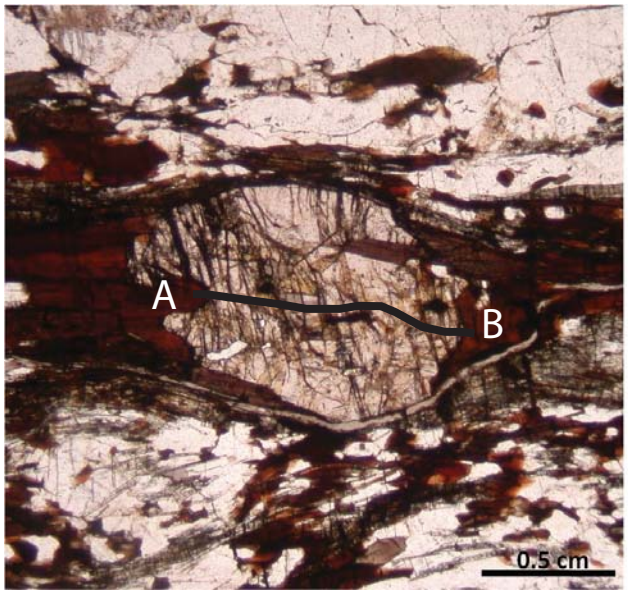
A
B
0.5 cm

b)

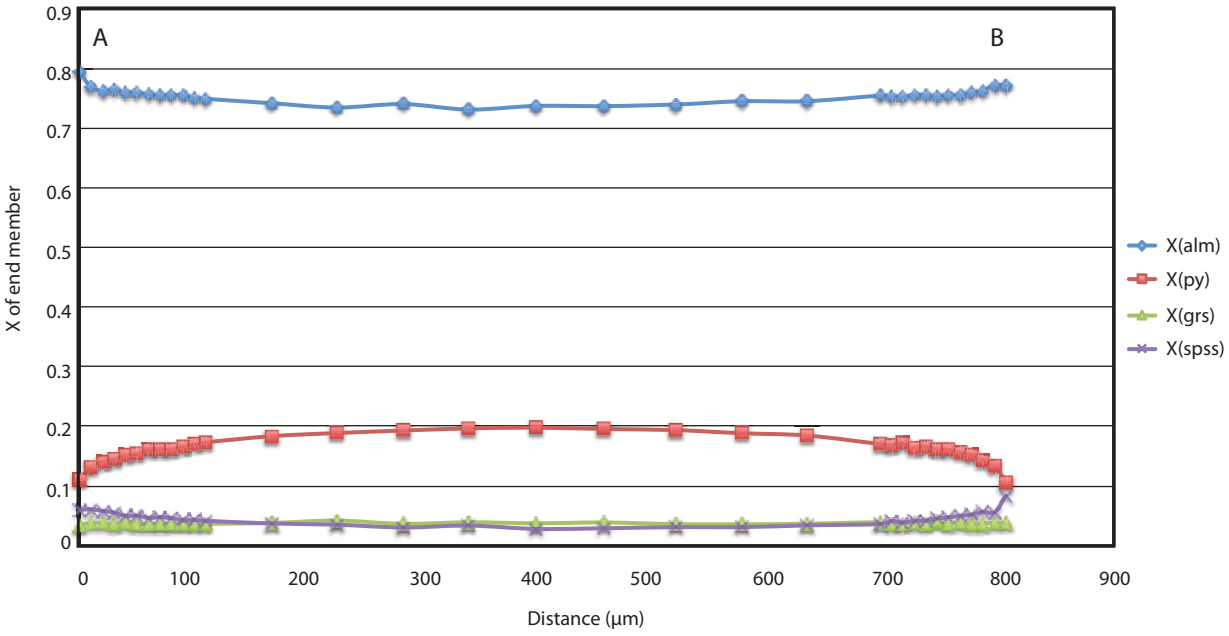
A
B
X of end member
Distance (μm)
X(alm)
X(py)
X(grs)
X(spss)

c)

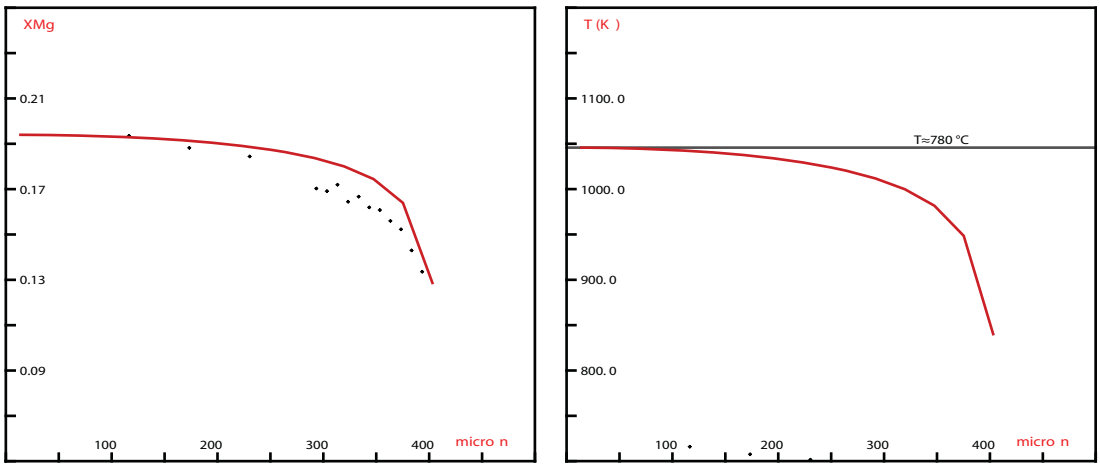
XMg
T (K)
T≈780 °C
micro n
micro n

Figure 8.

(a) AS2010-63D: Concordia plot of all data

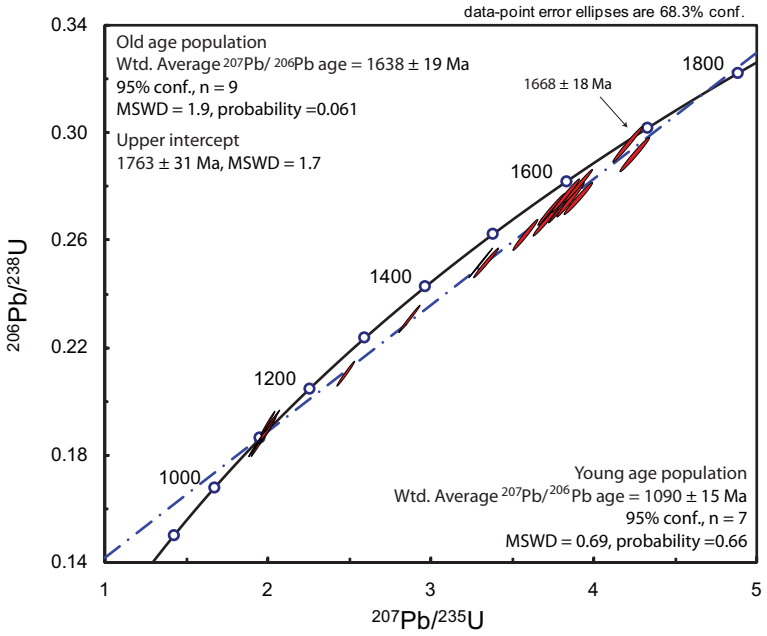

(b) AS2010-63D: Monazite backscatter electron images

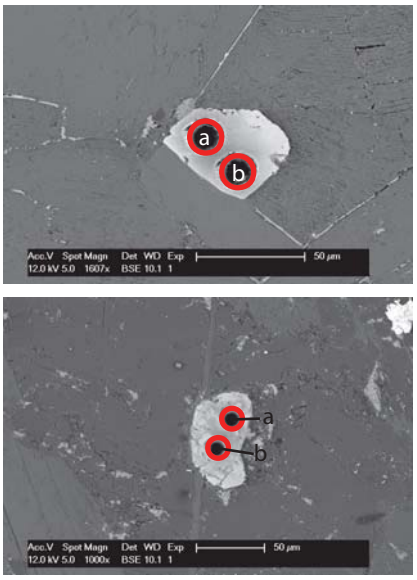

Mnz-9a
1083.4 ± 20.17Ma

Mnz-9b
1076.4 ± 20.31 Ma

Mnz-10a
1615.3 ± 18.15 Ma

Mnz-10b
1623.1 ± 18.34 Ma

(c) AS2010-65J Concordia plot of all data

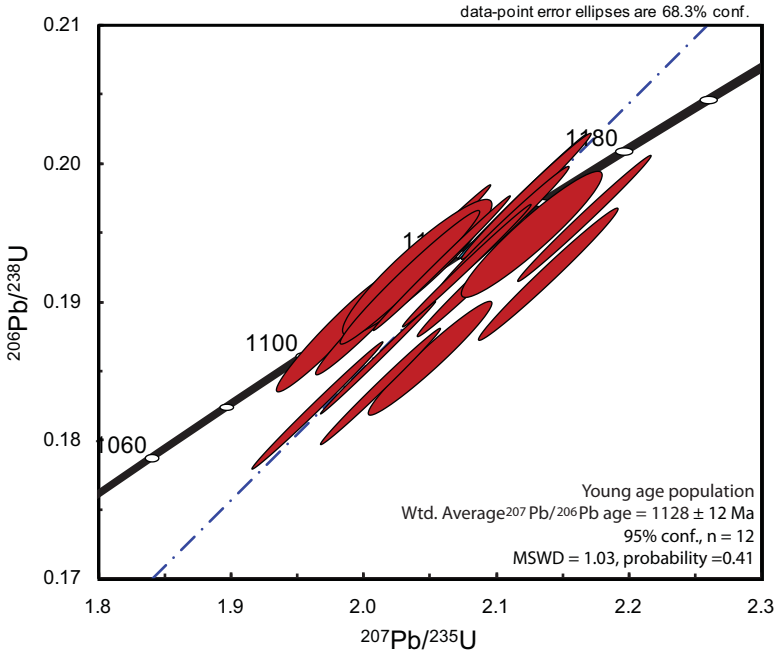

(d) AS2010-65J: Monazite backscatter electron images

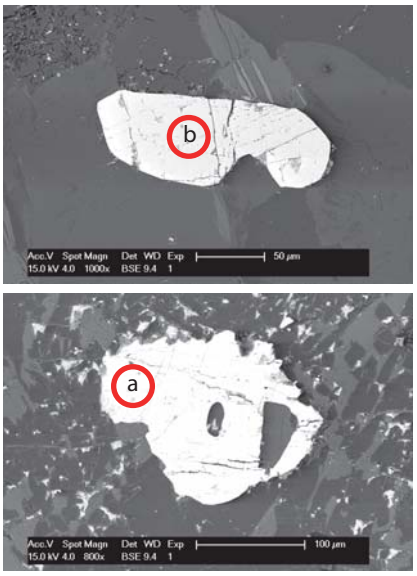

Mnz-1.8b
1141.1 ± 21.01 Ma

Mnz-1.9a
1191.9 ± 20.62 Ma

(e) AS2010-66D: Concordia plot of all data

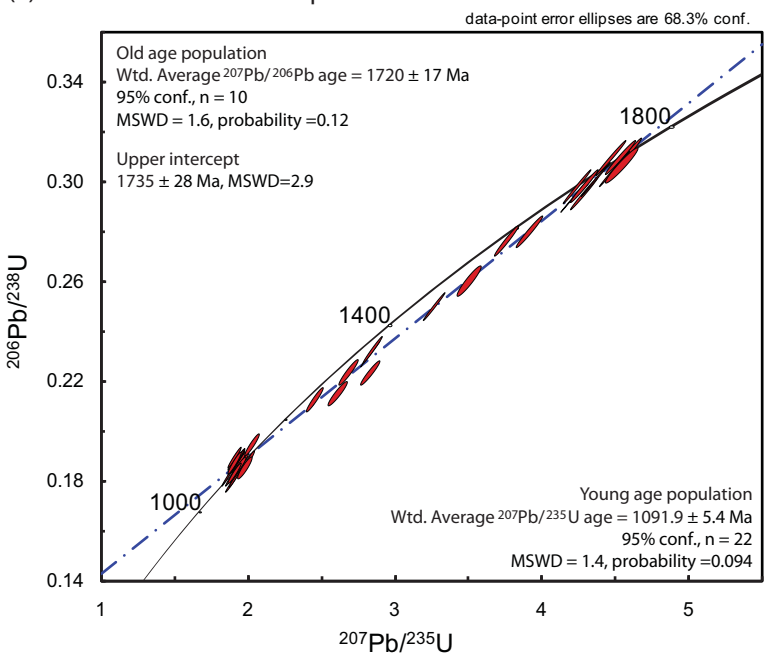

(f) AS2010-66D: Monazite backscatter electron images

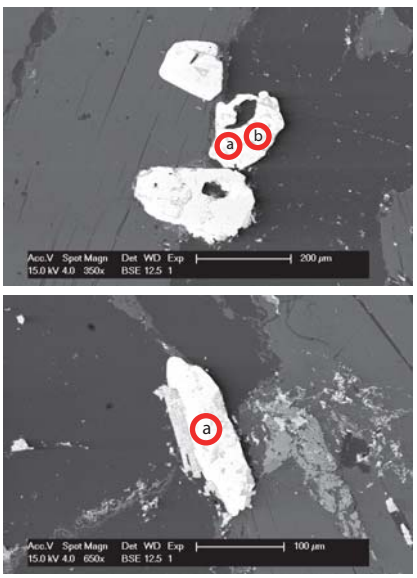

Mnz-9a
1055.9 ± 22.01 Ma

Mnz-9b
1043.1 ± 21.63 Ma

Mnz-5a
1745 ± 18.61 Ma

Figure 9.

(a) AS2010-66J: Concordia plot of all data

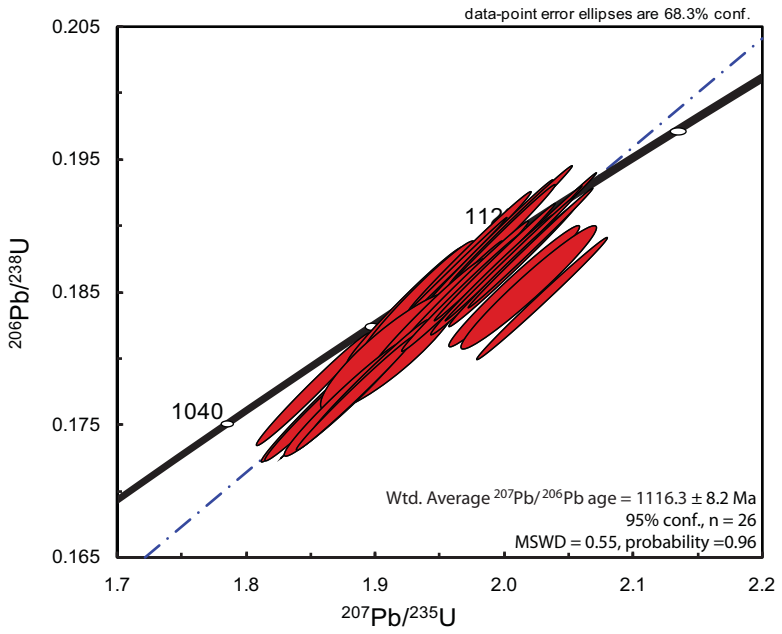

(b) AS2010-66J: Monazite backscatter electron images

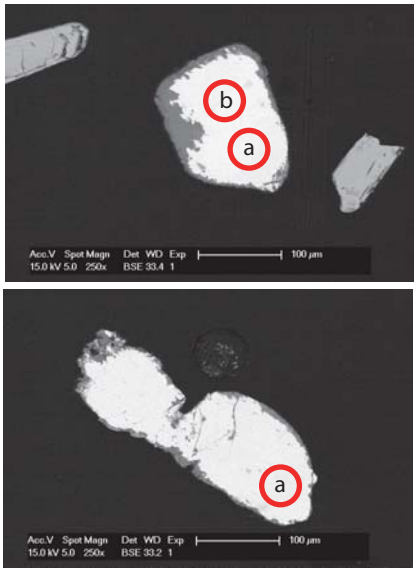

Mnz-10a
1112.4 ± 20.86 Ma

Mnz-10b
1098.8 ± 20.88 Ma

Mnz-16a
1135.5 ± 20.88 Ma

(c) AS2010-67A2: Concordia plot of all data

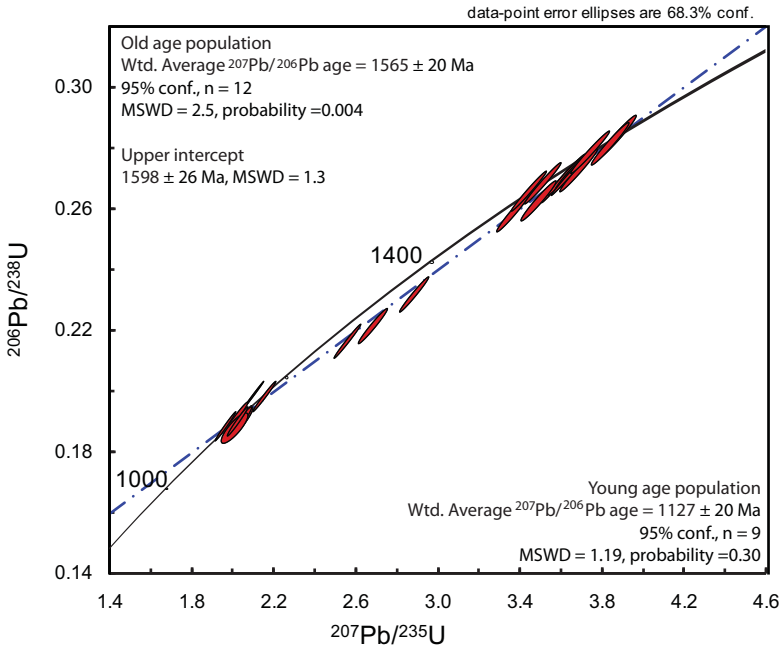

(d) AS2010-67A2: Monazite backscatter electron images

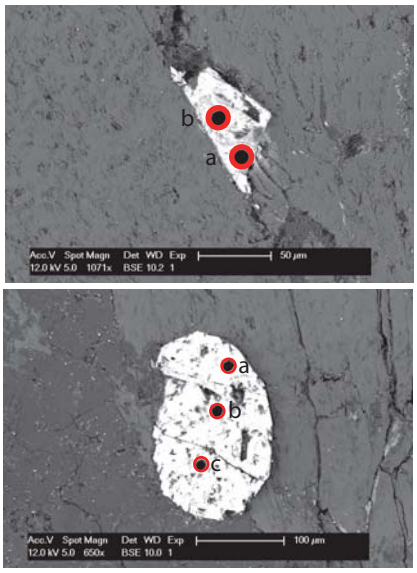

Mnz0-1a
1379.4 ± 22.4 Ma

Mnz0-1b
1112.6 ± 22.1 Ma

Mnz8a
1576 ± 19.6 Ma

Mnz8b
1587.3 ± 19.7 Ma

Mnz8c
1574.6 ± 20.7 Ma

(e) AS2010-72D: Concordia plot of all data

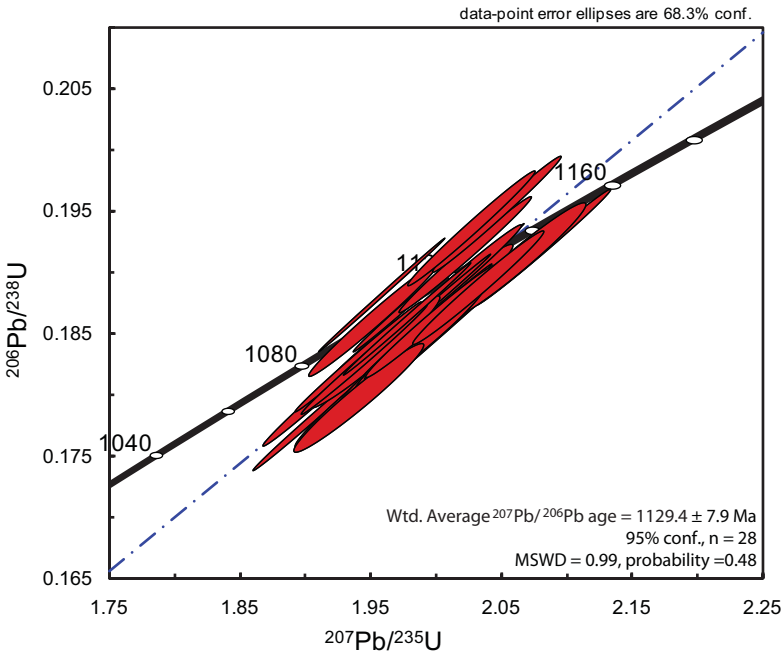

(f) AS2010-72D: Monazite backscatter electron images

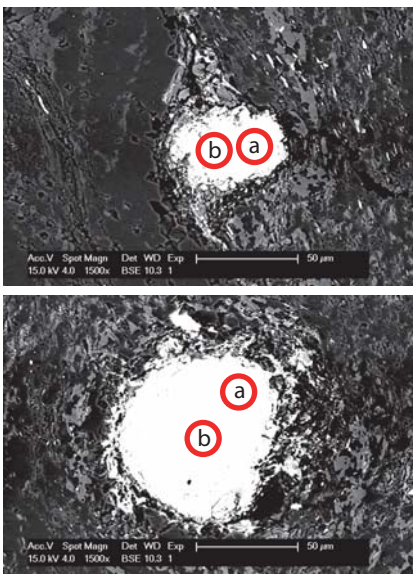

Mnz-1a
1136.2 ± 21.07 Ma

Mnz-1b
1122.1 ± 20.45 Ma

Mnz-12a
1126.8 ± 21.42 Ma

Mnz-12b
1129 ± 20.89 Ma

Figure 10.

(a) RED2011-01: Concordia plot of all data

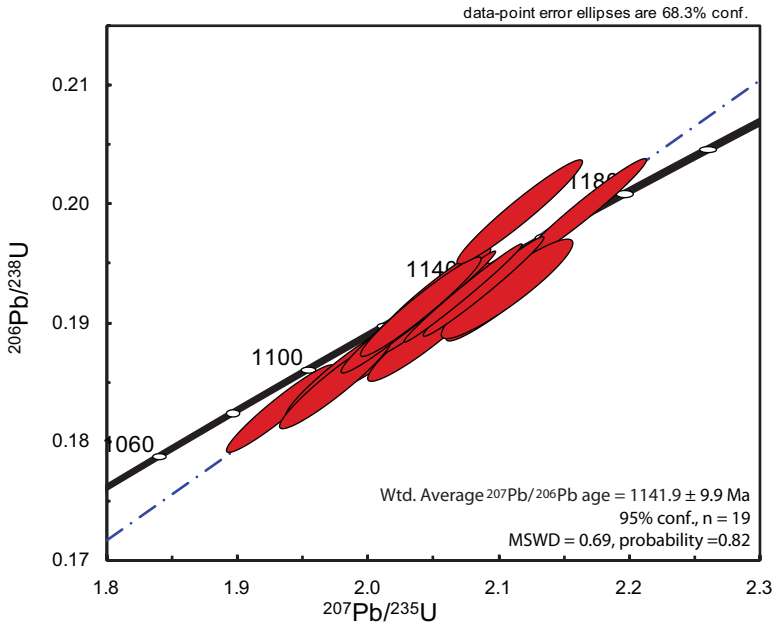

(b) RED2011-01: Monazite backscatter electron images

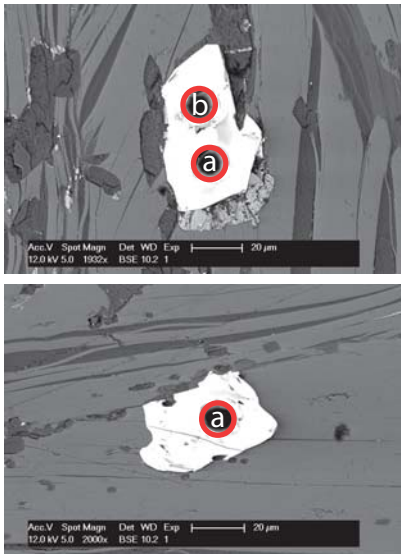

Mnz-10a
1130.3 ± 21.9 Ma

Mnz-10b
1130.2 ± 22.2 Ma

Mnz-7a
1165.8 ± 21.3 Ma

(c) AS2010-64J: Concordia plot of all data

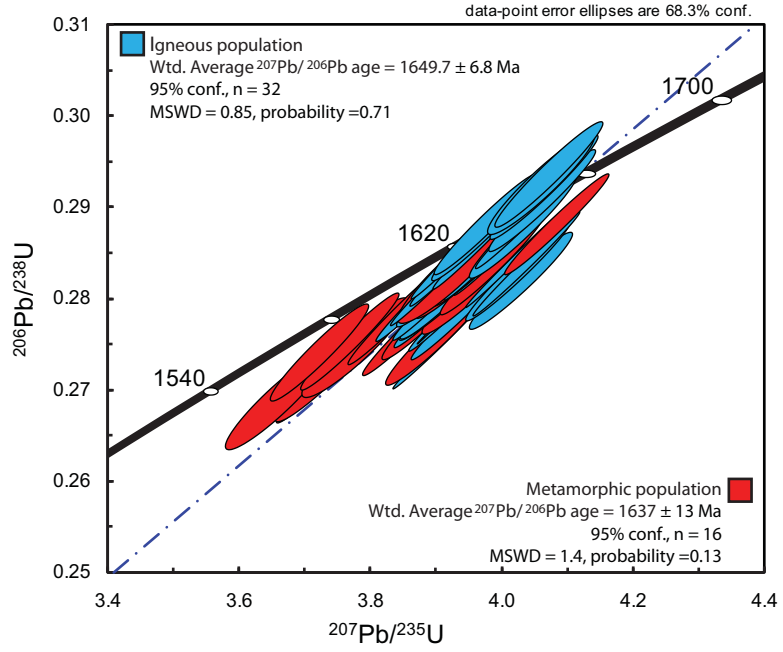

(d) AS2010-64J: Zircon cathodoluminescence images

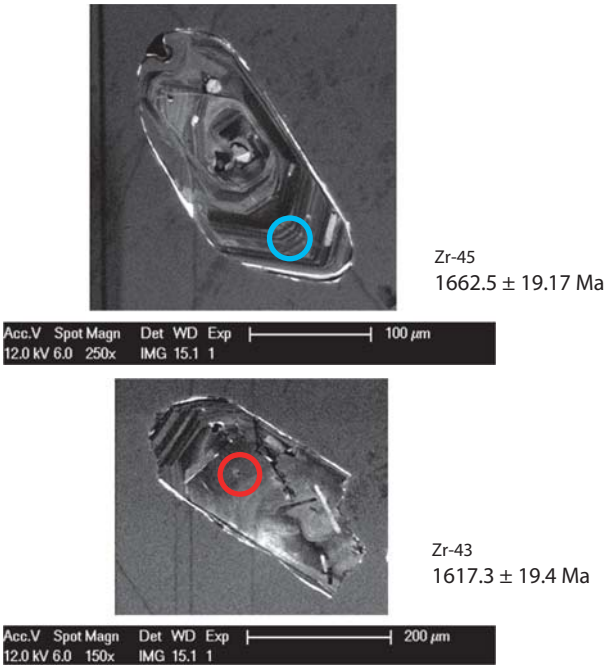

Zr-45
1662.5 ± 19.17 Ma

Zr-43
1617.3 ± 19.4 Ma

(e) COL2011-01: Concordia plot of all data

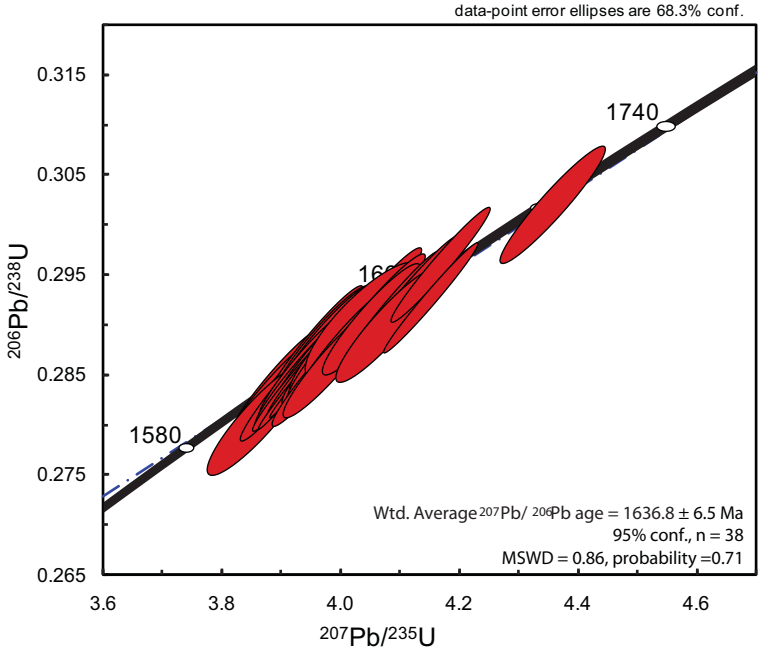

(f) COL2011-01: Zircon cathodoluminescence images

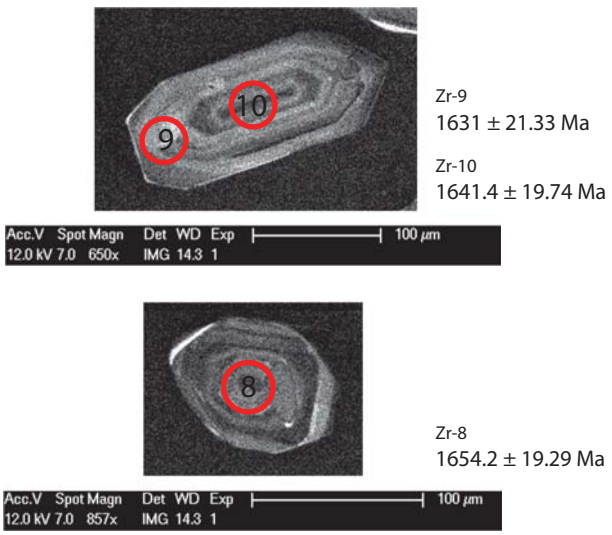

Zr-9
1631 ± 21.33 Ma

Zr-10
1641.4 ± 19.74 Ma

Zr-8
1654.2 ± 19.29 Ma

Figure 11.

(a) HAM2011-02: Concordia plot of all data

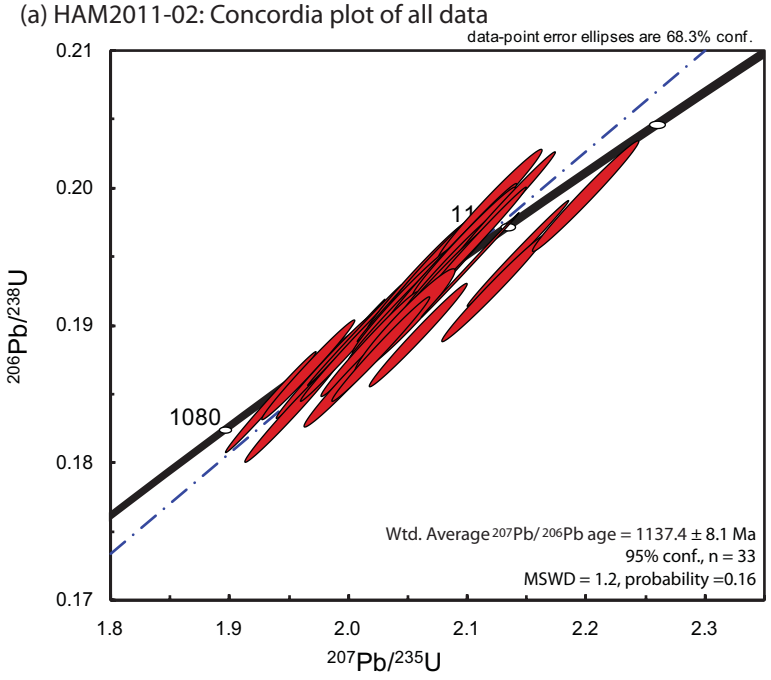

(b) HAM2011-02: Zircon cathodoluminescence images

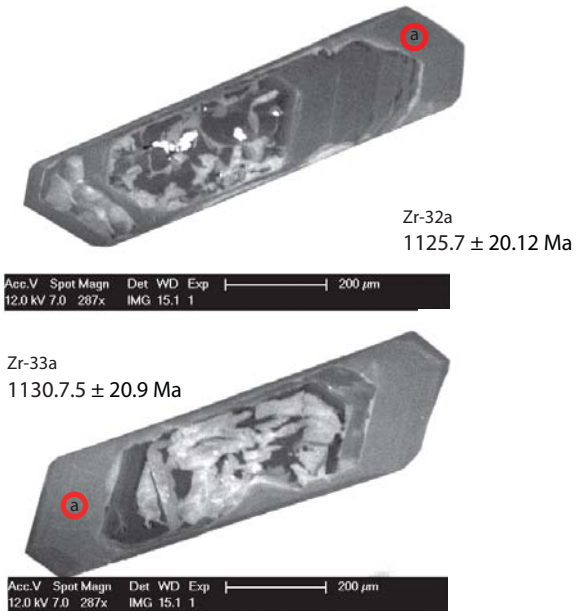

(c) HAM2011-08: Concordia plot of all data

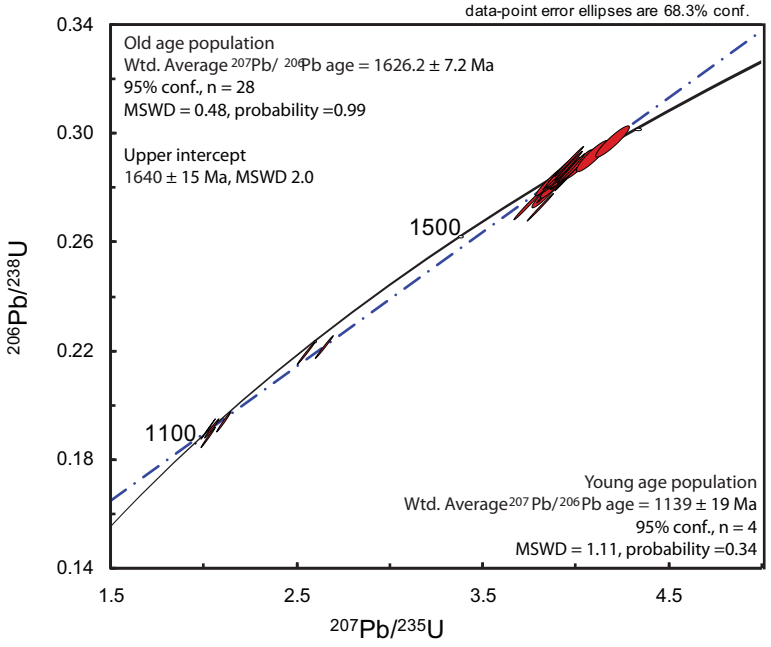

(d)HAM2011-08: Zircon cathodoluminescence images

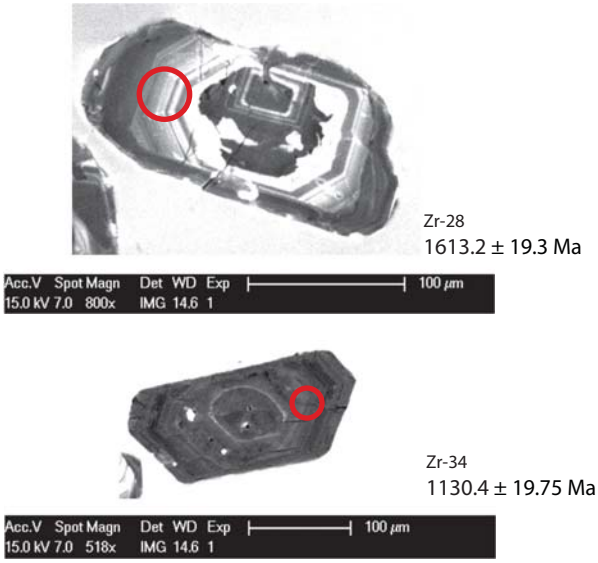

(e) AS09-4: Concordia plot of all data (Cutts *et al.* (personal communication, April 2011))

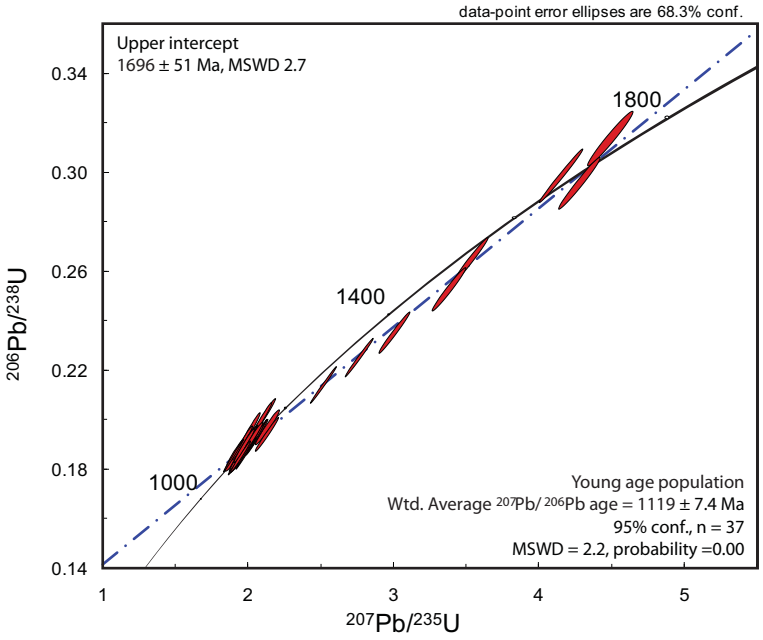

Figure 12.

(a) AS2010-62D: Concordia plot of 95-105% concordant data

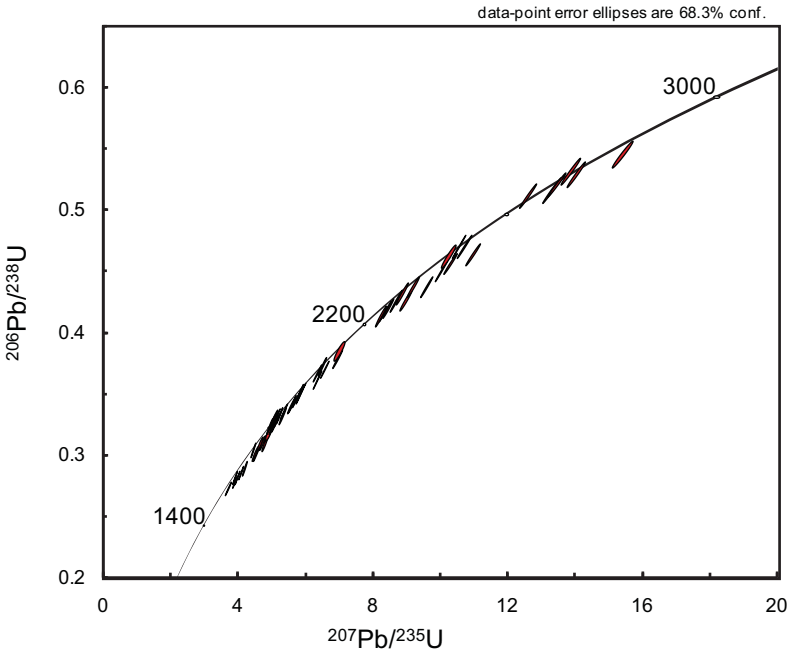

(b) AS2010-62D: Age spectra of detrital zircons, 95-105% concordancy, (n=61/75)

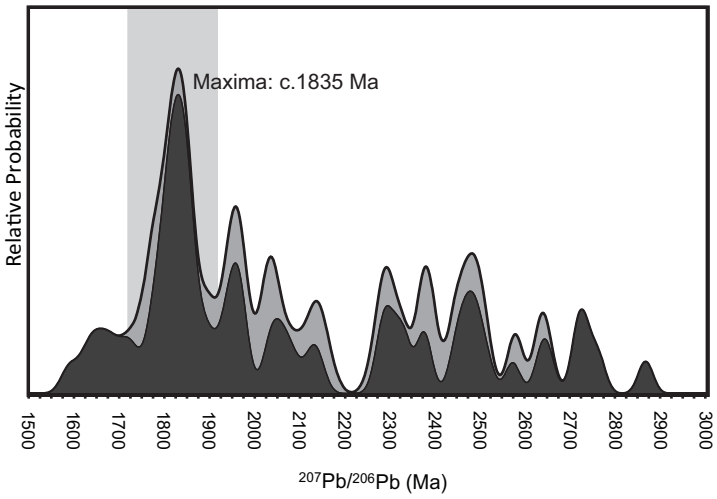

(c) AS2010-62D: Zircon cathodoluminescence images

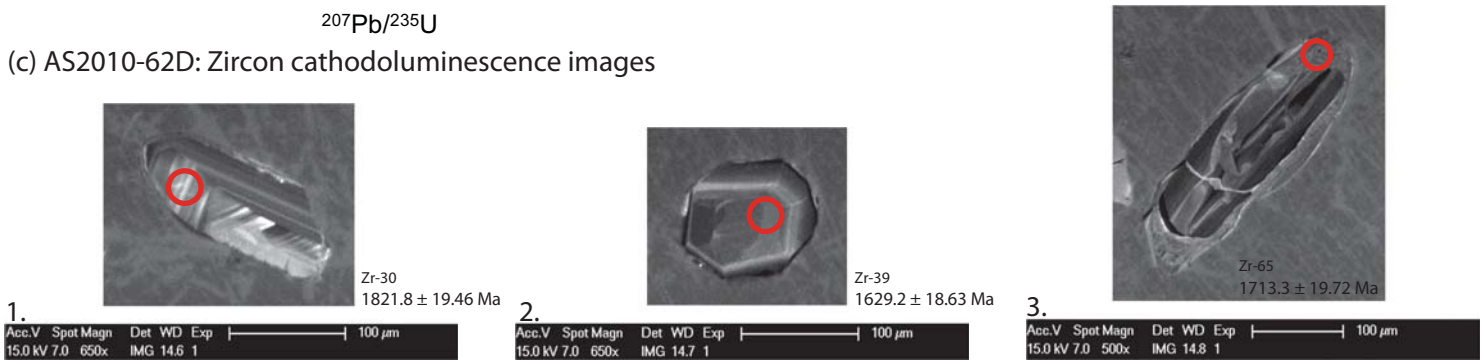

(d) AS2010-59J: Concordia plot of 95-105% concordant data

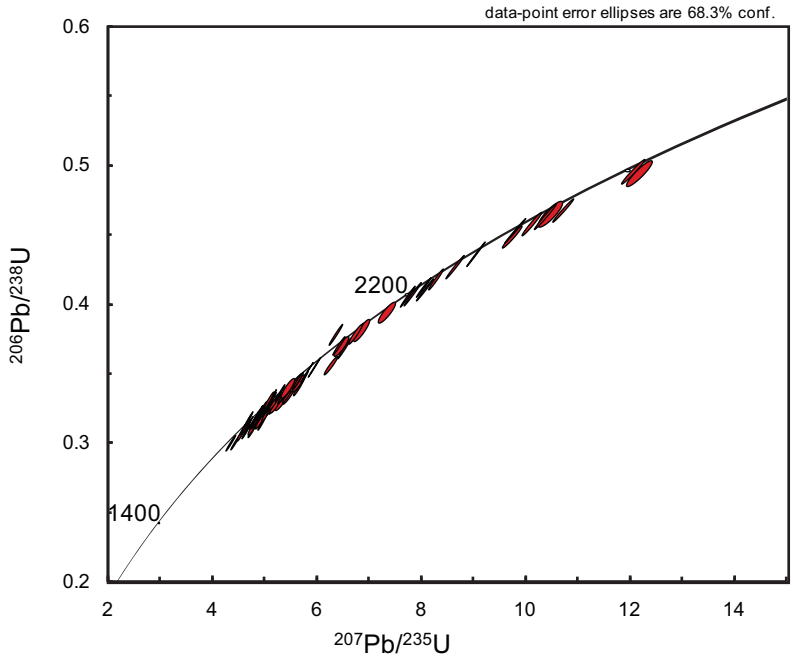

(e) AS2010-59J: Age spectra of detrital zircons, 95-105% concordancy, (n=81/101)

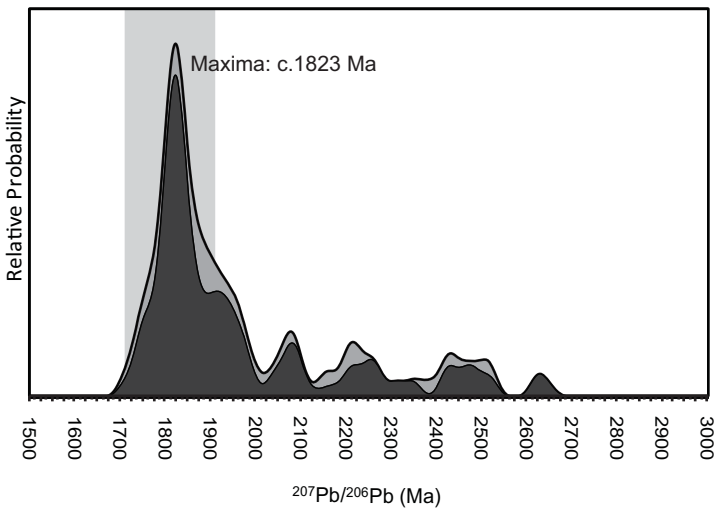

(f) AS2010-59J: Zircon cathodoluminescence images

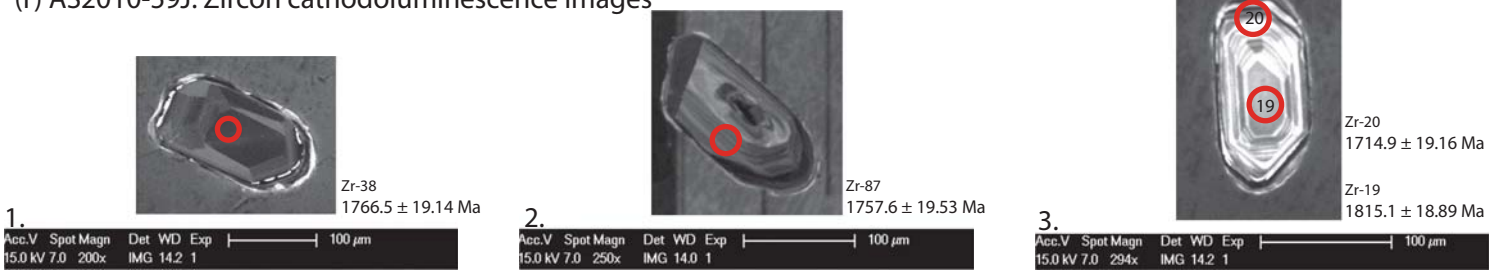

Figure 13.

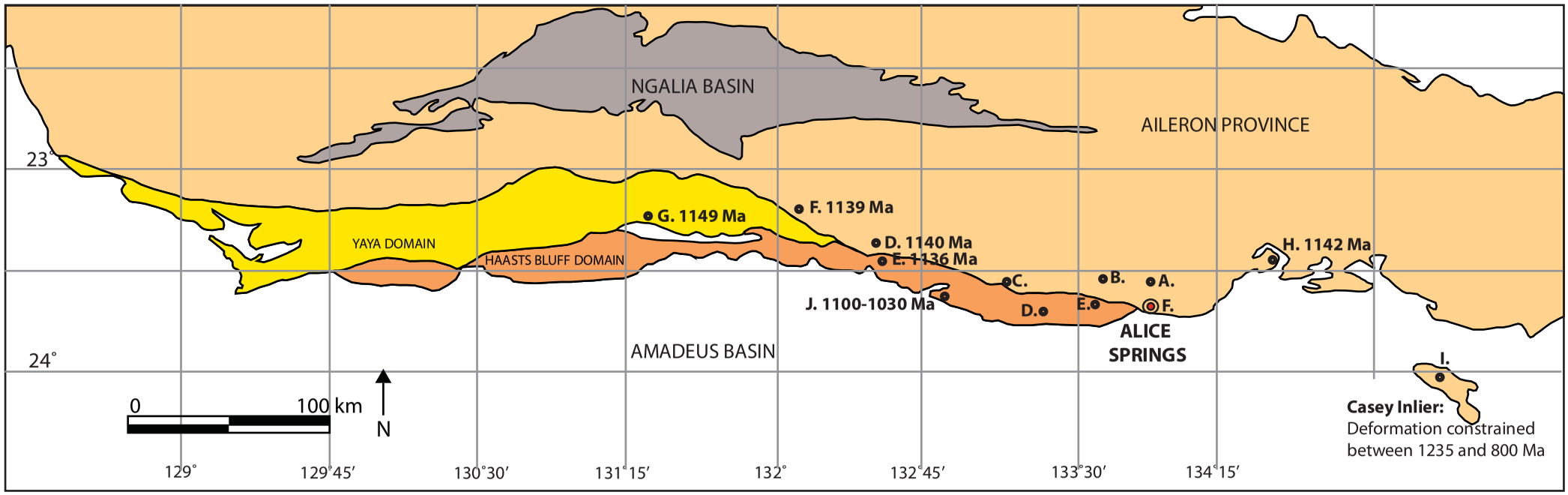

References listed in Table 4.

A. 1090 Ma
1128 Ma
1091 Ma
1127 Ma
1129 Ma
1116 Ma

B. 1137 Ma
1139 Ma

C. 1141 Ma

D. 1129 Ma
1121 Ma
1159 Ma
1100 Ma
1141 Ma

E. 1139 Ma

F. 1146 Ma
1120 Ma

Figure 14.

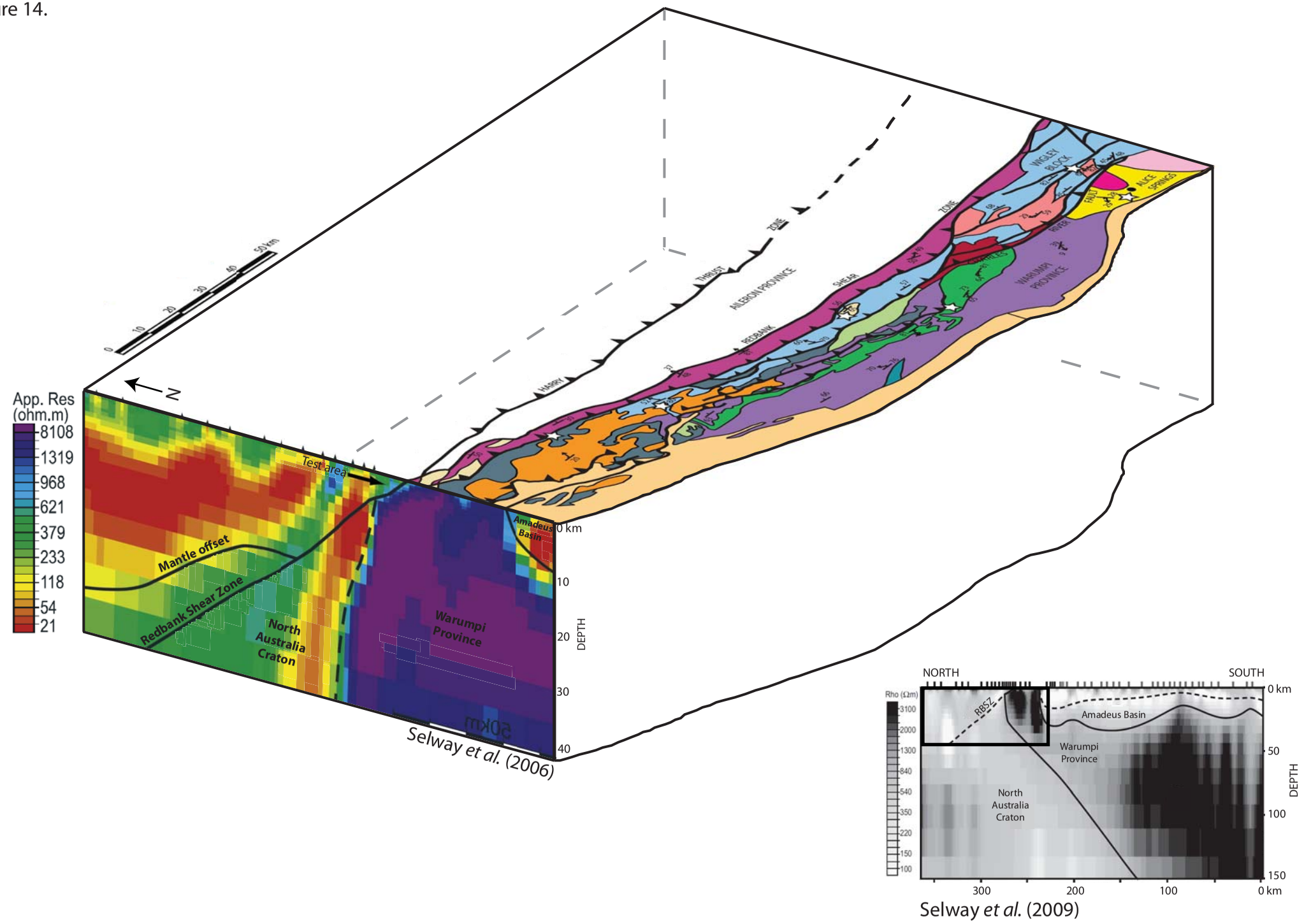
App. Res (ohm.m)
8108
1319
968
621
379
233
118
54
21
N
Test area
Mantle offset
Redbank Shear Zone
North Australia Craton
Warumpi Province
Amadeus Basin
50km
0 km
10
20
30
40
DEPTH
Selway et al. (2006)
NORTH
SOUTH
Rho (Ωm)
3100
2000
1300
840
540
350
220
150
100
RBSZ
Amadeus Basin
Warumpi Province
North Australia Craton
300
200
100
0 km
50
100
150
DEPTH
Selway et al. (2009)

Appendix 1- Whole rock geochrmical analyses

	AS2010-59J	AS2010-62D	AS2010-63D	AS2010-66D	AS2010-65J	AS2010-67A2	AS09-4
Major elements (wt%)							
SiO2	73.1	36.8	54.0	68.7	62.3	58.0	44.9
TiO2	0.6	1.3	0.7	0.9	0.8	1.1	1.7
Al2O3	12.6	29.6	25.3	14.5	14.4	15.7	21.1
Cr (ppm)	65.0	190.0	100.0	105.0	70.0	115.0	155.0
Fe2O3	5.9	17.4	8.9	7.6	11.5	11.3	15.0
MnO	0.1	0.3	0.1	0.1	0.1	0.1	0.2
MgO	1.8	5.6	2.8	2.6	2.4	3.4	4.9
Zn (ppm)	75.0	115.0	140.0	130.0	105.0	135.0	195.0
CaO	0.4	0.4	0.3	0.1	1.5	1.3	3.1
Na2O	0.6	0.4	1.1	0.1	1.3	1.6	3.0
K2O	3.0	5.0	6.5	2.7	3.3	5.5	4.4
LOI	0.8	1.4	1.6	0.9	0.8	1.6	0.7
Trace and REE (ppm)							
Sc	15	65	10	15	20	25	25
V	70	210	130	130	110	175	215
Ba	925	630	1305	495	885	1525	690
Be	1	1.5	9	0.5	1	1	1.5
Ce	140	275	145	180	130	105	445
Hf	7	6	3	9	7	10	12
La	70	135	75	90	65	50	220
Mo	<2	3	<2	<2	<2	2	<2
Nb	<10	30	15	15	<10	25	40
Rb	155	375	270	180	145	320	325
Sn	<10	<10	10	<10	<10	<10	10
Sr	60	20	115	20	85	165	195
Ta	<2	2	<2	<2	<2	<2	3
Th	32.5	60	27.5	38	26	25.5	120
U	3	7	3.5	3	1	1.5	6.5
Y	34	95	46	32	29	30	39
Zr	265	225	120	335	275	370	425
Dy	6	16	7.5	7	6	6	10
Er	4	12	4	3	3	3	3
Eu	1	1	2	1	2	1	2.5
Gd	8	19	8	10	8	7	23
Ho	1	3.5	1.5	1	1	1	1.5
Lu	0.5	2.5	0.5	<0.5	<0.5	<0.5	<0.5
Nd	50	110	55	70	55	40	165
Pr	14	30	16	19	15	11	47
Sm	9	20.5	9	12.5	9.5	7	29.5
Tb	1	2.5	1	1.5	1	1	2.5
Tm	<1	2	<1	<1	<1	<1	<1
Yb	4	14	3	2	2	2	2
Cs	1.7	7	4.6	2.1	4	3.7	4.2
Ga	14	42.5	26	23	18.5	19	32.5
Ag	0.4	0.7	0.3	0.4	0.3	0.4	0.8
As	<0.5	<0.5	<0.5	<0.5	<0.5	<0.5	<0.5
Cu	18	70	65	36.5	9	18.5	28.5
Ni	22	85	48	44	40	47	65
Pb	14	13	36.5	11	15.5	26	24

Appendix 2- Garnet profiles

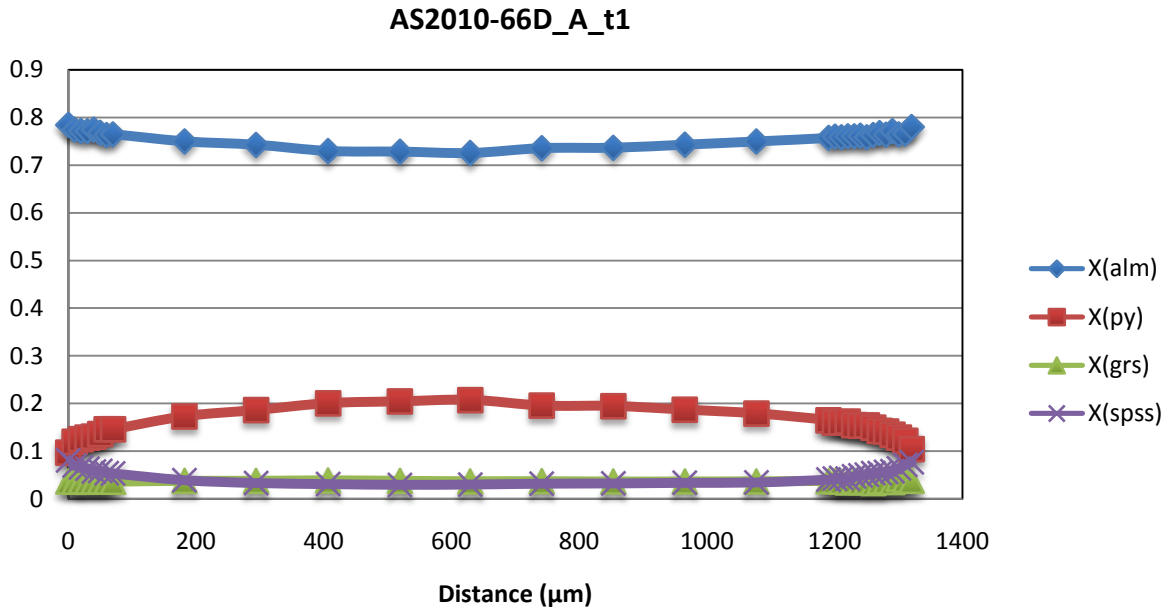

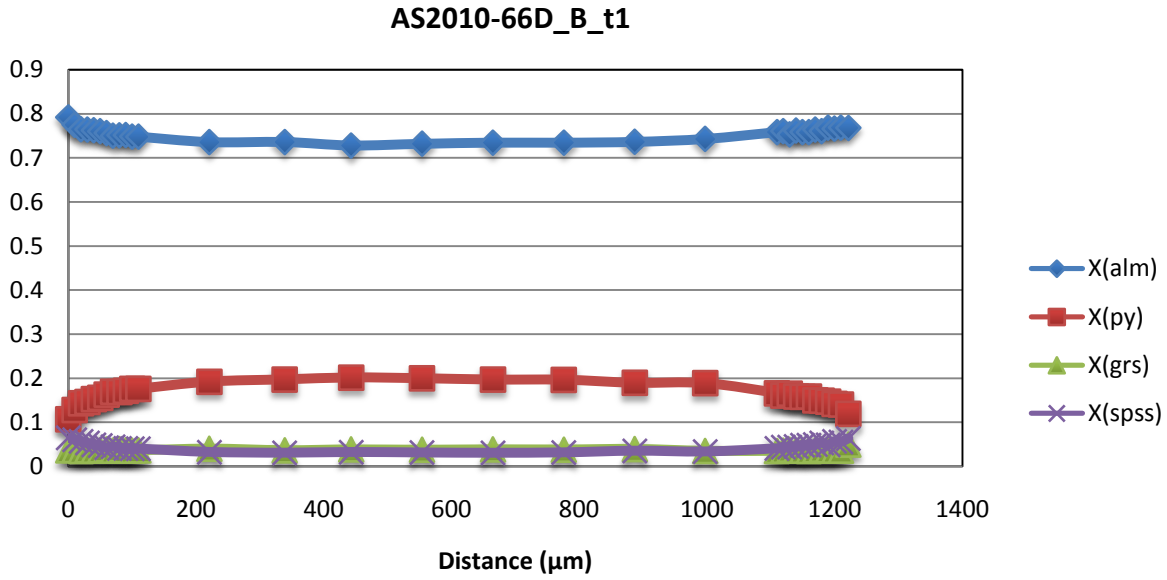

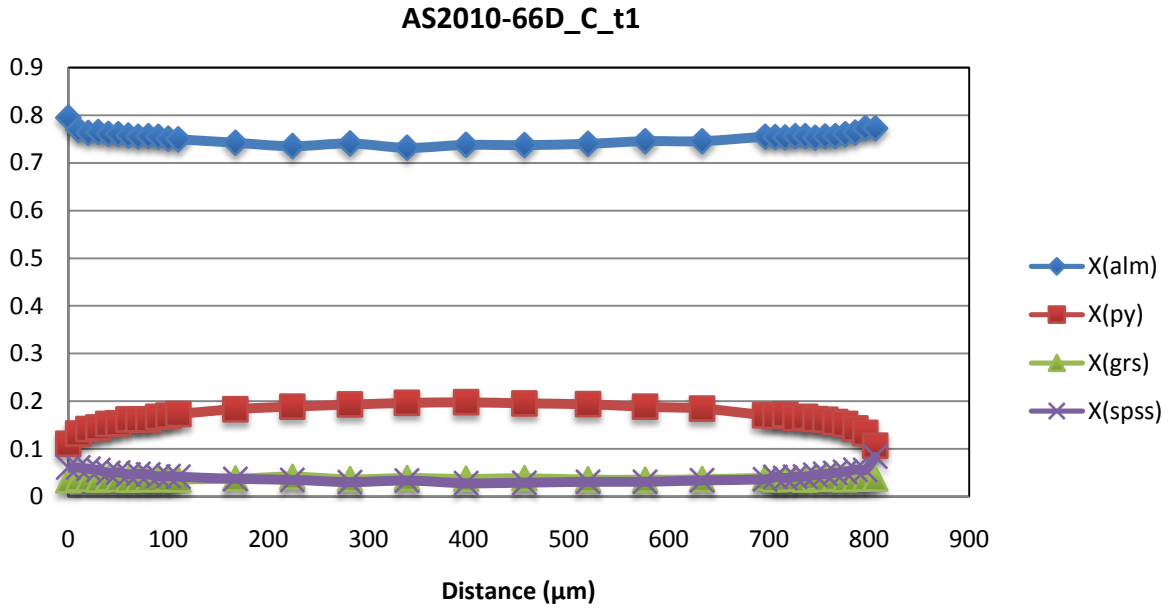

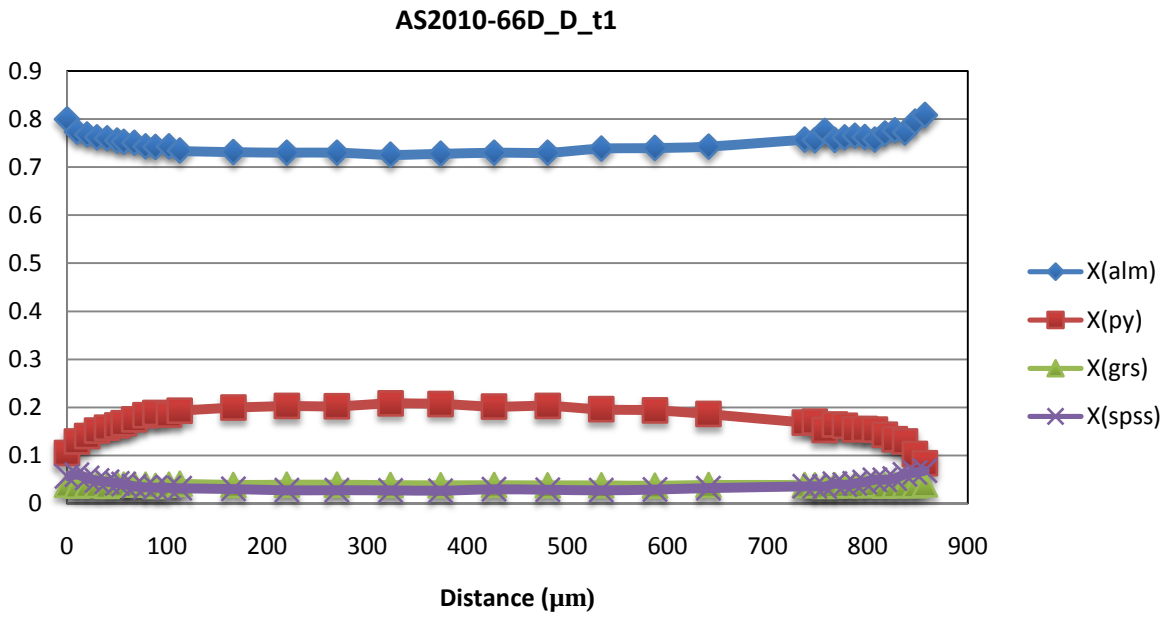
AS2010-66D_D_t1
0.9
0.8
0.7
0.6
0.5
0.4
0.3
0.2
0.1
0
0
100
200
300
400
500
600
700
800
900
Distance (µm)
X(alm)
X(py)
X(grs)
X(spss)

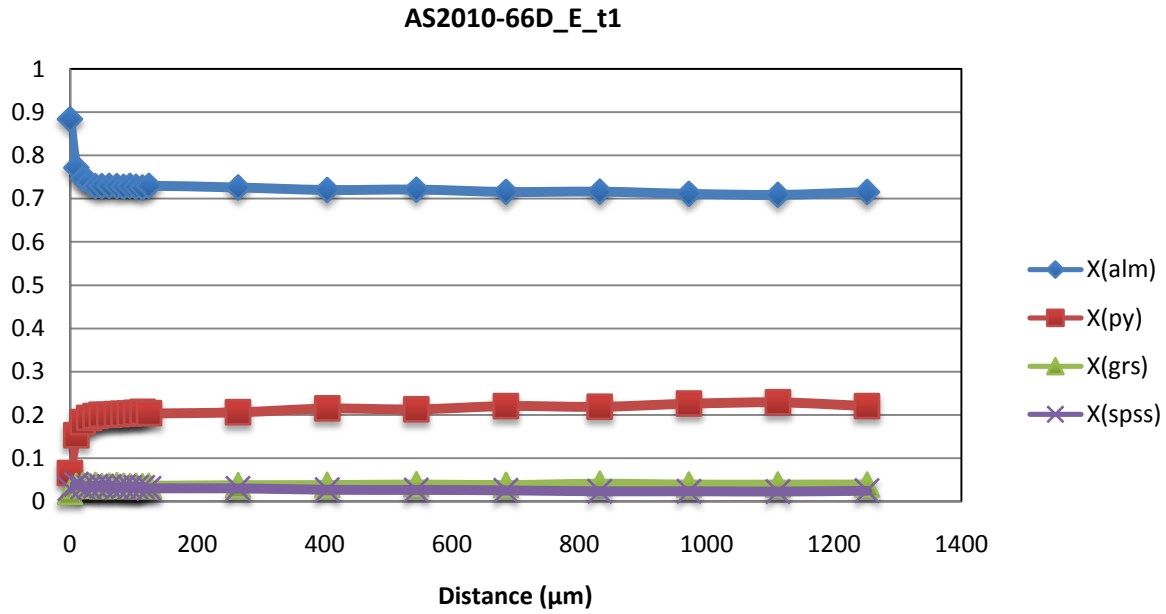
AS2010-66D_E_t1
1
0.9
0.8
0.7
0.6
0.5
0.4
0.3
0.2
0.1
0
0
200
400
600
800
1000
1200
1400
Distance (µm)
X(alm)
X(py)
X(grs)
X(spss)

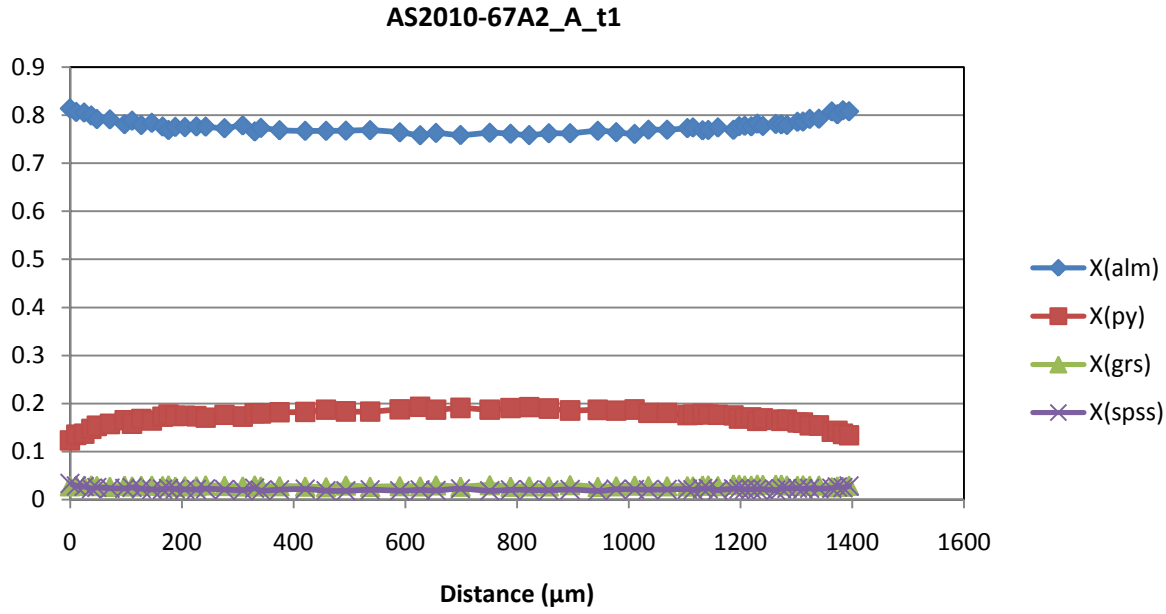
AS2010-67A2_A_t1
0.9
0.8
0.7
0.6
0.5
0.4
0.3
0.2
0.1
0
0
200
400
600
800
1000
1200
1400
1600
Distance (µm)
X(alm)
X(py)
X(grs)
X(spss)

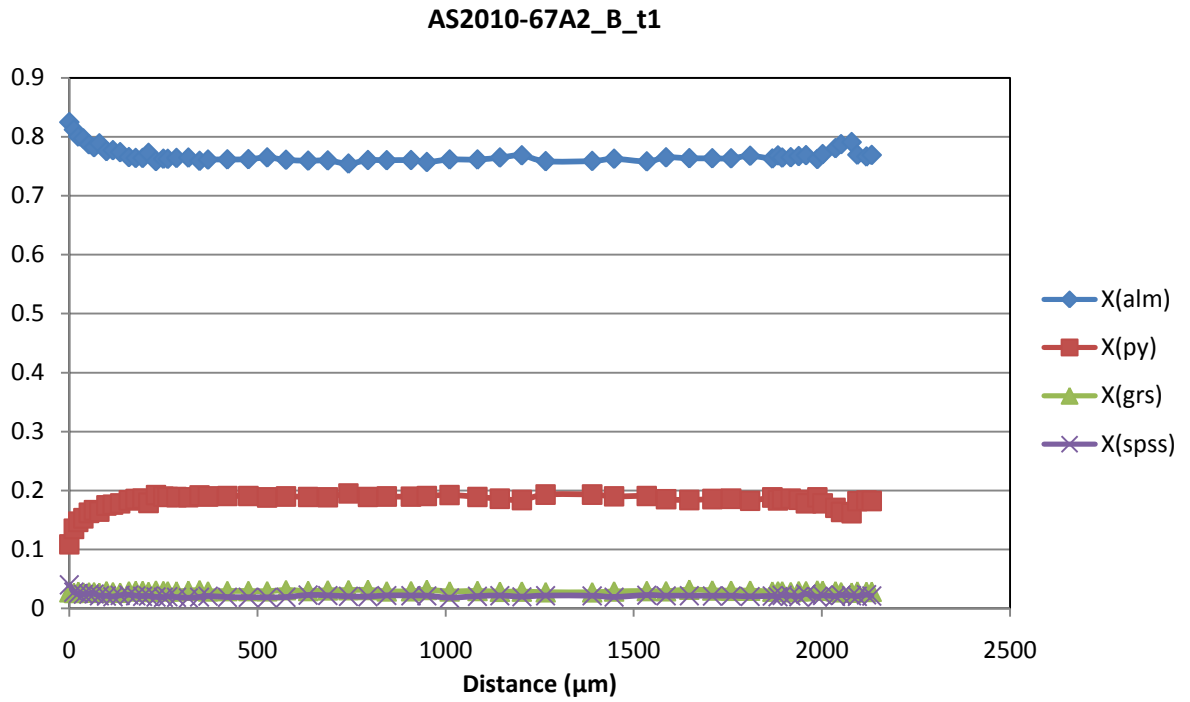
AS2010-67A2_B_t1
0.9
0.8
0.7
0.6
0.5
0.4
0.3
0.2
0.1
0
0
500
1000
1500
2000
2500
Distance (µm)
X(alm)
X(py)
X(grs)
X(spss)

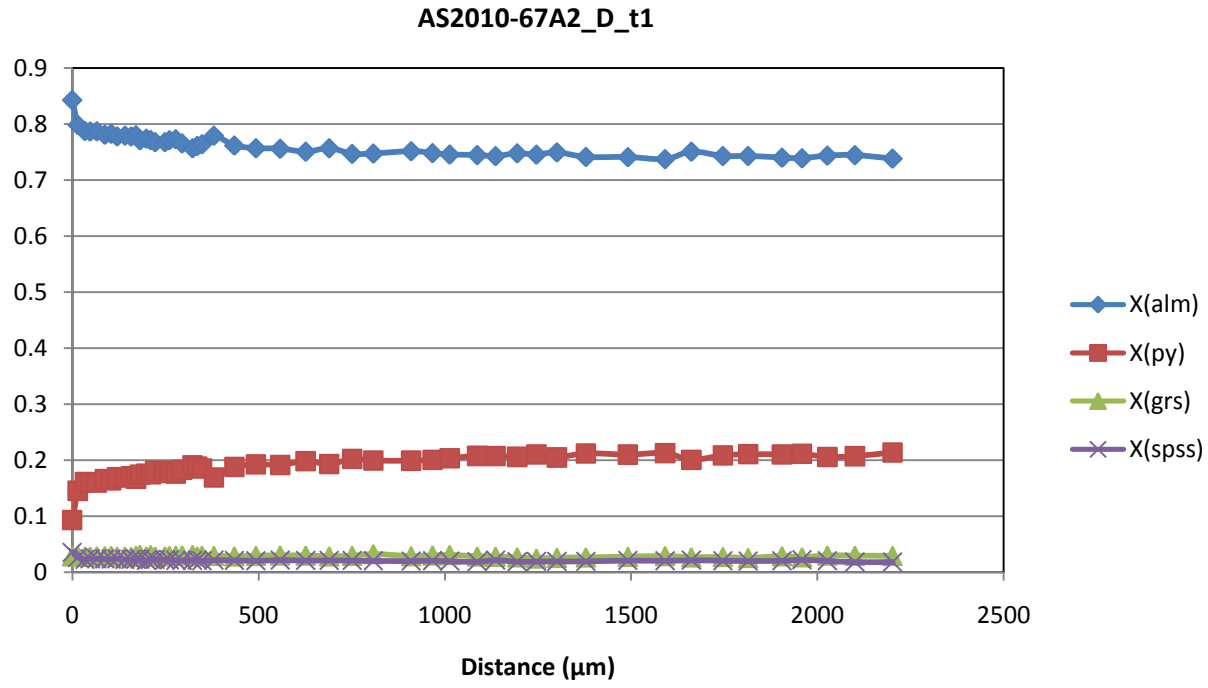
AS2010-67A2_D_t1
0.9
0.8
0.7
0.6
0.5
0.4
0.3
0.2
0.1
0
0
500
1000
1500
2000
2500
Distance (µm)
X(alm)
X(py)
X(grs)
X(spss)

Appendix 3- In situ U-Pb LA-ICPMS monazite data

Analysis	Ratios						Concordancy	Apparent ages					
	$^{207}Pb/^{206}Pb$	1σ	$^{206}Pb/^{238}U$	1σ	$^{207}Pb/^{235}U$	1σ		$^{207}Pb/^{206}Pb$	1σ	$^{206}Pb/^{238}U$	1σ	$^{207}Pb/^{235}U$	1σ
Monazite data													
AS2010-63D													
mnz12a	0.07522	0.00076	0.18179	0.00269	1.8847	0.02737	100	1074.3	20.23	1076.7	14.65	1075.7	9.63
mnz9b	0.07529	0.00077	0.18934	0.00278	1.96503	0.02854	104	1076.4	20.31	1117.8	15.09	1103.6	9.77
mnz14b	0.07536	0.00076	0.18337	0.00268	1.90464	0.02706	101	1078	20.01	1085.3	14.59	1082.7	9.46
mnz9a	0.07556	0.00076	0.19006	0.0028	1.97937	0.02859	104	1083.4	20.17	1121.7	15.15	1108.5	9.74
mnz14a	0.07616	0.00077	0.18336	0.00271	1.92523	0.02781	99	1099.3	20.09	1085.3	14.74	1089.9	9.65
mnz11a	0.07621	0.00077	0.18004	0.00264	1.89176	0.02725	97	1100.6	20.09	1067.2	14.4	1078.2	9.57
mnz11b	0.07711	0.00091	0.17875	0.00256	1.89613	0.02841	94	1124.1	23.37	1060.2	14	1079.7	9.96
mnz1a	0.08559	0.00086	0.21059	0.00308	2.48368	0.03584	93	1328.9	19.31	1232	16.42	1267.3	10.45
mnz13c	0.09035	0.00091	0.23413	0.00352	2.91616	0.0432	95	1432.9	19.17	1356.1	18.39	1386.1	11.2
mnz2b	0.09539	0.00102	0.25174	0.00369	3.30907	0.04857	94	1535.9	19.96	1447.4	18.98	1483.2	11.45
mnz5a	0.09639	0.00097	0.25161	0.0037	3.34193	0.04851	93	1555.4	18.76	1446.8	19.05	1490.9	11.34
mnz13a	0.09876	0.00098	0.26734	0.00393	3.6398	0.05206	95	1600.8	18.35	1527.3	20	1558.3	11.39
mnz1b	0.09928	0.001	0.2621	0.00383	3.58546	0.05137	93	1610.7	18.57	1500.6	19.55	1546.3	11.38
mnz10b	0.09953	0.00098	0.26378	0.00387	3.61852	0.05156	93	1615.3	18.15	1509.1	19.75	1553.6	11.34
mnz10a	0.09995	0.00099	0.26897	0.00393	3.70568	0.05251	95	1623.1	18.34	1535.6	19.98	1572.6	11.33
mnz2a	0.10027	0.00105	0.2725	0.004	3.76496	0.05519	95	1629.1	19.33	1553.5	20.29	1585.3	11.76
mnz5b	0.10041	0.00101	0.27673	0.00408	3.82876	0.05555	97	1631.6	18.54	1574.9	20.59	1598.8	11.68
mnz7a	0.10122	0.00101	0.28016	0.00416	3.90803	0.05731	97	1646.7	18.46	1592.2	20.93	1615.3	11.86
mnz4a	0.10154	0.00107	0.27255	0.00408	3.81301	0.05743	94	1652.5	19.33	1553.7	20.67	1595.5	12.12
mnz13b	0.10243	0.00101	0.29253	0.00432	4.12996	0.05953	99	1668.6	18.17	1654.2	21.53	1660.3	11.78
mnz8a	0.1029	0.00102	0.27564	0.00406	3.90782	0.05642	94	1677.2	18.23	1569.3	20.5	1615.3	11.67
mnz6a	0.10578	0.00105	0.29189	0.00429	4.25489	0.06144	96	1728	18.1	1651	21.42	1684.7	11.87
AS2010-65J													
mnz1.1a	0.07544	0.00075	0.18775	0.0028	1.97788	0.02851	103	1080.2	19.79	1109.2	15.2	1108	9.72
mnz2.7c	0.07664	0.00085	0.19358	0.00322	2.04444	0.03417	103	1111.7	22.1	1140.7	17.38	1130.4	11.39
mnz1.9a	0.07668	0.00078	0.1891	0.00287	2.00945	0.02988	100	1112.9	20.15	1116.5	15.54	1118.7	10.08
mnz2.4a	0.07691	0.00104	0.19251	0.00324	2.04013	0.03715	101	1118.8	26.79	1135	17.53	1129	12.41
mnz2.7b	0.07699	0.0009	0.19182	0.0032	2.03499	0.03469	101	1120.8	23.04	1131.2	17.3	1127.3	11.6
mnz1.2a	0.07741	0.0008	0.186	0.00267	2.0111	0.0288	97	1131.7	20.36	1099.7	14.53	1119.3	9.71
mnz2.7a	0.07749	0.00085	0.19282	0.0032	2.05887	0.0343	100	1133.9	21.59	1136.6	17.29	1135.2	11.39
mnz1.4a	0.07777	0.00083	0.19761	0.00298	2.11938	0.03205	102	1141.1	21.01	1162.5	16.05	1155.1	10.43
mnz1.4b	0.07789	0.00084	0.19766	0.00299	2.123	0.03239	102	1144	21.28	1162.7	16.12	1156.3	10.53
mnz1.6b	0.07801	0.0009	0.19532	0.00299	2.10532	0.03254	100	1147.2	22.8	1150.1	16.1	1150.5	10.64
mnz2.1b	0.07814	0.00086	0.18254	0.00302	1.9654	0.03266	94	1150.5	21.75	1080.8	16.44	1103.7	11.18
mnz1.9b	0.07821	0.00084	0.19264	0.00294	2.07773	0.03185	99	1152.2	21.21	1135.7	15.87	1141.5	10.51
mnz1.3a *	0.07759	0.00082	0.1495	0.00216	1.61777	0.02341	79	1136.5	20.77	898.1	12.11	977.1	9.08
mnz2.2b *	0.07764	0.00083	0.17076	0.00282	1.82672	0.03001	89	1137.6	21.1	1016.3	15.52	1055.1	10.78
mnz2.6a *	0.07897	0.00084	0.19229	0.00318	2.09249	0.03436	97	1171.4	20.83	1133.7	17.2	1146.3	11.28
mnz1.2b *	0.07901	0.0009	0.18595	0.0027	2.05047	0.03081	94	1172.3	22.34	1099.4	14.68	1132.5	10.26
mnz1.3b *	0.07912	0.00082	0.1658	0.0024	1.82813	0.02634	84	1175.2	20.45	988.9	13.26	1055.6	9.46
mnz1.5c *	0.07913	0.00099	0.1949	0.00302	2.12709	0.03506	98	1175.3	24.44	1147.8	16.28	1157.6	11.38
mnz1.8b *	0.07972	0.0009	0.18389	0.00276	2.01297	0.03003	91	1190	22.02	1088.2	15.02	1119.9	10.12

mnz1.10a *	0.07979	0.00084	0.19607	0.00302	2.16637	0.03315	97	1191.9	20.62	1154.2	16.29	1170.3	10.63
mnz1.5b *	0.08022	0.00091	0.17838	0.00258	2.00026	0.02995	88	1202.4	22.14	1058.1	14.11	1115.6	10.14
mnz1.8a *	0.08034	0.00089	0.14108	0.00211	1.5909	0.02408	71	1205.4	21.77	850.7	11.89	966.6	9.44
mnz2.2a *	0.08084	0.00085	0.19204	0.00317	2.13921	0.03488	93	1217.7	20.46	1132.4	17.12	1161.6	11.28
mnz2.3b *	0.0847	0.00112	0.17656	0.00297	2.06067	0.03703	80	1308.6	25.51	1048.2	16.27	1135.8	12.29
AS2010-66D													
mnz1b	0.07279	0.00085	0.18956	0.00281	1.91039	0.02902	111	1008	23.62	1119	15.25	1084.7	10.12
mnz12c	0.07306	0.00088	0.1886	0.00281	1.90707	0.02942	110	1015.7	24.11	1113.8	15.23	1083.6	10.28
mnz12a	0.07386	0.00084	0.18871	0.0028	1.92824	0.02903	107	1037.6	22.77	1114.4	15.19	1090.9	10.07
mnz10a	0.07398	0.00081	0.18692	0.00277	1.91092	0.02844	106	1040.8	21.94	1104.6	15.06	1084.9	9.92
mnz12b	0.07399	0.00084	0.18922	0.00281	1.93754	0.02917	107	1041.2	22.85	1117.1	15.22	1094.1	10.08
mnz9b	0.07406	0.0008	0.18753	0.00278	1.91868	0.02834	106	1043.1	21.63	1108	15.08	1087.6	9.86
mnz16a	0.07415	0.00089	0.18741	0.00278	1.91534	0.02992	106	1045.4	23.99	1107.3	15.07	1086.4	10.42
mnz10b	0.07432	0.00083	0.18841	0.0028	1.93524	0.029	106	1050.1	22.33	1112.8	15.17	1093.4	10.03
mnz10c	0.07432	0.00082	0.18724	0.00278	1.92516	0.02874	105	1050.2	22.11	1106.4	15.08	1089.9	9.97
mnz15b	0.07447	0.00081	0.18212	0.00266	1.8696	0.02755	102	1053.9	21.99	1078.5	14.51	1070.4	9.75
mnz9a	0.07454	0.00081	0.18825	0.00279	1.93843	0.02881	105	1055.9	22.01	1111.9	15.15	1094.5	9.95
mnz8c	0.07511	0.00087	0.18766	0.00278	1.94461	0.02986	103	1071.4	23.04	1108.7	15.08	1096.6	10.3
mnz8a	0.07512	0.00086	0.18644	0.00274	1.93227	0.02934	103	1071.6	22.81	1102.1	14.91	1092.3	10.16
mnz2b	0.07524	0.00096	0.1948	0.00293	2.03204	0.03234	107	1074.8	25.3	1147.3	15.78	1126.3	10.83
mnz14a	0.07546	0.00084	0.1822	0.00265	1.89508	0.02804	100	1080.9	22.14	1079	14.43	1079.4	9.83
mnz21a	0.07548	0.0009	0.18338	0.00273	1.90862	0.02965	100	1081.3	23.66	1085.4	14.87	1084.1	10.35
mnz8b	0.07578	0.00089	0.18733	0.00277	1.95869	0.03025	102	1089.3	23.46	1106.9	15.02	1101.4	10.38
mnz19a	0.0758	0.00093	0.18574	0.00277	1.94128	0.03086	101	1089.9	24.48	1098.2	15.07	1095.4	10.65
mnz15c	0.07617	0.00083	0.18356	0.00269	1.92775	0.02862	99	1099.6	21.77	1086.4	14.67	1090.8	9.92
mnz14b	0.07651	0.00083	0.17956	0.00264	1.89598	0.02827	96	1108.4	21.62	1064.5	14.42	1079.7	9.91
mnz15a	0.07661	0.00085	0.18151	0.00265	1.91655	0.0285	97	1111	21.99	1075.2	14.47	1086.9	9.92
mnz4a	0.07733	0.00088	0.18789	0.00276	2.00406	0.03046	98	1129.7	22.62	1109.9	14.97	1116.9	10.3
mnz26a	0.07741	0.001	0.1854	0.0028	1.97838	0.03279	97	1131.9	25.58	1096.4	15.24	1108.2	11.18
mnz27a	0.10158	0.0011	0.28003	0.00421	3.91921	0.0602	96	1653.2	19.88	1591.5	21.22	1617.7	12.43
mnz23a	0.10306	0.00108	0.29832	0.00444	4.24284	0.06278	100	1679.9	19.19	1683	22.03	1682.4	12.16
mnz6a	0.10386	0.00113	0.29454	0.00429	4.22643	0.06153	98	1694.2	20	1664.2	21.36	1679.2	11.95
mnz22a	0.10432	0.00107	0.29841	0.00446	4.29344	0.06332	99	1702.3	18.69	1683.4	22.13	1692.1	12.15
mnz24a	0.10474	0.00112	0.30977	0.0046	4.47465	0.06696	102	1709.7	19.57	1739.6	22.66	1726.3	12.42
mnz22c	0.10533	0.0011	0.30094	0.00447	4.36992	0.0648	99	1720	19.09	1696	22.17	1706.7	12.25
mnz22b	0.10534	0.00109	0.29548	0.00439	4.29185	0.0633	97	1720.2	18.85	1668.9	21.87	1691.8	12.15
mnz19b	0.1062	0.00108	0.30999	0.00455	4.53857	0.06559	100	1735.1	18.46	1740.7	22.41	1738.1	12.02
mnz24c	0.10669	0.00111	0.30534	0.00461	4.49363	0.06765	99	1743.7	18.87	1717.7	22.75	1729.8	12.5
mnz5a	0.10677	0.00109	0.31101	0.00453	4.58115	0.06592	100	1745	18.61	1745.7	22.27	1745.8	11.99
mnz25a	0.10745	0.00127	0.30683	0.00463	4.54712	0.07148	98	1756.7	21.48	1725.1	22.82	1739.6	13.08
mnz2a *	0.08366	0.00097	0.2129	0.00313	2.45654	0.03773	97	1284.4	22.58	1244.3	16.65	1259.3	11.08
mnz18a *	0.08707	0.00105	0.22364	0.00336	2.68463	0.04235	96	1362	22.95	1301.1	17.72	1324.2	11.67
mnz24b *	0.08803	0.00109	0.21524	0.00326	2.61207	0.04223	91	1383.1	23.6	1256.7	17.27	1304	11.87
mnz20a *	0.08877	0.00098	0.23277	0.0035	2.85246	0.04339	96	1399.2	21.03	1349	18.28	1369.5	11.44
mnz3a *	0.08892	0.00093	0.23109	0.00337	2.83408	0.04137	96	1402.5	19.84	1340.2	17.66	1364.6	10.96
mnz1a *	0.09191	0.00109	0.22366	0.00329	2.83598	0.0436	89	1465.5	22.39	1301.2	17.35	1365.1	11.54
mnz17a *	0.09482	0.00099	0.25013	0.00364	3.26964	0.04725	94	1524.5	19.52	1439.1	18.79	1473.9	11.24
mnz25b *	0.09774	0.00121	0.26034	0.00394	3.50843	0.05639	94	1581.5	22.92	1491.6	20.13	1529.1	12.7
mnz7a *	0.0986	0.001	0.27627	0.00402	3.75952	0.05361	98	1597.8	18.88	1572.5	20.3	1584.1	11.44

AS2010-66J													
mnz2a	0.07561	0.00084	0.17771	0.00279	1.85142	0.02942	97	1084.6	22.05	1054.4	15.25	1063.9	10.48
mnz5a	0.07583	0.00077	0.18402	0.0029	1.92286	0.02989	100	1090.7	20.28	1088.9	15.81	1089.1	10.38
mnz1	0.07597	0.00075	0.18455	0.00286	1.93203	0.02918	100	1094.3	19.63	1091.8	15.55	1092.2	10.1
mnz10b	0.07614	0.0008	0.18802	0.00301	1.97254	0.0314	101	1098.8	20.88	1110.6	16.34	1106.2	10.73
mnz3b	0.07619	0.00082	0.18596	0.00307	1.95257	0.03228	100	1100.1	21.43	1099.5	16.67	1099.3	11.1
mnz5b	0.07629	0.00078	0.17648	0.00279	1.85512	0.029	95	1102.6	20.42	1047.7	15.3	1065.3	10.31
mnz29b	0.07642	0.00082	0.18877	0.00312	1.98797	0.03274	101	1106	21.21	1114.7	16.91	1111.4	11.13
mnz14a	0.07642	0.00085	0.17659	0.00284	1.85937	0.03031	95	1106.1	22.18	1048.3	15.54	1066.8	10.76
mnz4a	0.07655	0.00082	0.19003	0.00299	2.0045	0.03166	101	1109.5	21.31	1121.5	16.22	1117	10.7
mnz10a	0.07666	0.00081	0.18854	0.00302	1.99143	0.03173	100	1112.4	20.86	1113.4	16.38	1112.6	10.77
mnz15a	0.07675	0.00081	0.18444	0.00295	1.95043	0.03109	98	1114.8	20.98	1091.2	16.06	1098.6	10.7
mnz6a	0.07683	0.00077	0.18317	0.0029	1.93908	0.03015	97	1116.8	19.96	1084.3	15.81	1094.7	10.42
mnz8a	0.07683	0.00114	0.18052	0.00299	1.91097	0.03586	96	1116.8	29.44	1069.8	16.31	1084.9	12.51
mnz21b	0.07685	0.00083	0.17687	0.0029	1.87306	0.03071	94	1117.4	21.41	1049.8	15.88	1071.6	10.85
mnz21a	0.07692	0.00089	0.17705	0.00291	1.87654	0.03164	94	1119	23.03	1050.8	15.95	1072.8	11.17
mnz26b	0.07694	0.00084	0.18572	0.00307	1.96919	0.03273	98	1119.5	21.68	1098.2	16.7	1105	11.19
mnz6b	0.07701	0.0008	0.17864	0.00286	1.89544	0.03007	94	1121.4	20.52	1059.5	15.65	1079.5	10.55
mnz7a	0.07711	0.00084	0.17742	0.00285	1.88502	0.03055	94	1124.1	21.68	1052.9	15.62	1075.8	10.75
mnz30a	0.07716	0.00081	0.18514	0.00305	1.96871	0.03222	97	1125.4	20.79	1095	16.59	1104.9	11.02
mnz1b	0.07721	0.00083	0.18728	0.00292	1.99256	0.03116	98	1126.6	21.21	1106.6	15.87	1113	10.57
mnz20a	0.07745	0.00083	0.18938	0.00309	2.0212	0.03292	99	1132.9	21.28	1118	16.73	1122.7	11.06
mnz29c	0.07746	0.00083	0.18829	0.00311	2.0101	0.03314	98	1133.1	21.17	1112.1	16.87	1118.9	11.18
mnz16a	0.07756	0.00082	0.18633	0.00301	1.99115	0.03193	97	1135.5	20.88	1101.5	16.33	1112.5	10.84
mnz29a	0.07755	0.00084	0.18754	0.0031	2.00439	0.03318	98	1135.5	21.41	1108	16.84	1117	11.21
mnz31a	0.07783	0.00085	0.18713	0.00309	2.00704	0.03336	97	1142.5	21.61	1105.8	16.78	1117.9	11.26
mnz4b	0.07784	0.00083	0.18837	0.00297	2.02049	0.03194	97	1142.9	21.13	1112.5	16.14	1122.4	10.74
mnz16b *	0.07855	0.0009	0.18545	0.00302	2.00721	0.03334	94	1160.9	22.61	1096.7	16.4	1118	11.26
mnz26a *	0.07904	0.00094	0.18536	0.00308	2.01901	0.03468	93	1173.1	23.36	1096.2	16.78	1121.9	11.67
mnz28a *	0.07977	0.00084	0.18457	0.00304	2.02899	0.03324	92	1191.3	20.65	1091.9	16.56	1125.3	11.14
AS2010-67A2													
mnz10a	0.0755	0.00084	0.18869	0.00317	1.96308	0.03266	103	1081.9	22.04	1114.3	17.16	1102.9	11.19
mnz2d	0.07647	0.00091	0.19179	0.00324	2.02149	0.03505	102	1107.5	23.48	1131.1	17.51	1122.8	11.78
mza0-1b	0.07667	0.00087	0.19857	0.00327	2.09615	0.03461	105	1112.6	22.1	1167.6	17.57	1147.5	11.35
mnz9b	0.07722	0.00082	0.19021	0.00317	2.02389	0.03309	100	1127	20.9	1122.5	17.17	1123.6	11.11
mnz9a	0.07743	0.00134	0.1881	0.00329	2.00708	0.04182	98	1132.4	34.06	1111.1	17.87	1117.9	14.12
mza0-1a	0.07765	0.00082	0.19068	0.00315	2.04035	0.03331	99	1138	20.94	1125	17.03	1129.1	11.12
mnz2b	0.0778	0.00097	0.18991	0.0032	2.03627	0.03585	98	1141.8	24.56	1120.9	17.33	1127.7	11.99
mnz2a	0.07783	0.00111	0.18985	0.00323	2.03608	0.03818	98	1142.4	28.19	1120.6	17.51	1127.7	12.77
mnz2c	0.07882	0.0009	0.19827	0.00333	2.15399	0.03662	100	1167.6	22.37	1166	17.89	1166.3	11.79
mnz6a	0.09403	0.00113	0.26593	0.00446	3.44189	0.05844	101	1508.7	22.43	1520.1	22.72	1514	13.36
mnz4a	0.09434	0.001	0.25907	0.00429	3.36675	0.05449	98	1514.9	19.78	1485.1	21.98	1496.7	12.67
mnz6b	0.09495	0.00104	0.2685	0.00447	3.51116	0.05757	100	1527.1	20.49	1533.2	22.69	1529.7	12.96
mnz4b	0.09643	0.00099	0.26282	0.00437	3.49109	0.05643	97	1556.2	19.08	1504.2	22.3	1525.2	12.76
mza1-1a	0.09687	0.00103	0.26913	0.00449	3.59305	0.05945	98	1564.7	19.73	1536.4	22.81	1548	13.14
mza1-2b	0.09703	0.00103	0.2712	0.00448	3.62494	0.05908	99	1567.8	19.77	1546.9	22.72	1555	12.97
mnz9c	0.09735	0.00105	0.27873	0.00467	3.73901	0.06169	101	1573.9	20.08	1585	23.55	1579.8	13.22
mnz8c	0.09738	0.00109	0.27158	0.00454	3.64173	0.06053	98	1574.6	20.73	1548.8	23.02	1558.7	13.24
mnz8a	0.09746	0.00103	0.27286	0.00454	3.66264	0.05979	99	1576	19.58	1555.3	22.99	1563.3	13.02

mnz8b	0.09805	0.00104	0.27264	0.00454	3.68221	0.06027	98	1587.3	19.7	1554.2	22.97	1567.5	13.07
mnz5a	0.09895	0.00102	0.28156	0.00468	3.83796	0.06231	100	1604.4	19.12	1599.2	23.56	1600.7	13.08
mza1-2a	0.09898	0.001	0.28377	0.00471	3.87089	0.06266	100	1605	18.74	1610.3	23.63	1607.6	13.06
mza0-2b *	0.08577	0.00091	0.21651	0.00358	2.55898	0.04185	95	1333	20.44	1263.4	18.96	1289	11.94
mza1-1b *	0.08786	0.00104	0.22154	0.0037	2.68155	0.04584	94	1379.4	22.44	1290	19.53	1323.4	12.64
mza0-2a *	0.09028	0.00094	0.23197	0.00382	2.88558	0.04674	94	1431.4	19.76	1344.8	19.97	1378.2	12.22
AS2010-72D													
mnz-4a	0.07549	0.00079	0.18819	0.00308	1.95753	0.03201	103	1081.6	20.92	1111.5	16.69	1101	10.99
mnz-19a	0.07595	0.00078	0.19364	0.0031	2.02655	0.03213	104	1093.6	20.52	1141.1	16.73	1124.5	10.78
mnz-2b	0.07605	0.00084	0.18624	0.00306	1.95161	0.03253	100	1096.4	21.98	1101	16.61	1099	11.19
mnz-18b	0.07621	0.00078	0.19483	0.00312	2.04601	0.03248	104	1100.5	20.46	1147.5	16.84	1131	10.83
mnz-4b	0.07654	0.00079	0.18823	0.00307	1.98519	0.03228	100	1109.3	20.51	1111.8	16.68	1110.5	10.98
mnz-5b	0.0766	0.00082	0.19152	0.00312	2.02155	0.03322	102	1110.9	21.33	1129.6	16.89	1122.8	11.16
mnz-17a	0.07685	0.00083	0.18315	0.00298	1.9397	0.03169	97	1117.3	21.28	1084.2	16.22	1094.9	10.95
mnz-17c	0.07703	0.00082	0.18625	0.00301	1.97709	0.03202	98	1122	21.02	1101	16.38	1107.7	10.92
mnz-1b	0.07704	0.0008	0.18034	0.00295	1.91425	0.03109	95	1122.1	20.45	1068.8	16.1	1086.1	10.83
mnz-17b	0.07711	0.00083	0.18299	0.00297	1.9444	0.03172	96	1124	21.29	1083.3	16.18	1096.5	10.94
mnz-2a	0.07718	0.00082	0.18603	0.00305	1.97844	0.0325	98	1125.8	21.09	1099.9	16.56	1108.2	11.08
mnz-13a	0.07719	0.0009	0.18356	0.00301	1.95224	0.03315	96	1126	23.06	1086.4	16.41	1099.2	11.4
mnz-12a	0.07722	0.00084	0.18929	0.00309	2.01401	0.03322	99	1126.8	21.42	1117.5	16.76	1120.2	11.19
mnz-3a	0.07729	0.00081	0.18934	0.0031	2.01643	0.03298	99	1128.7	20.8	1117.8	16.79	1121.1	11.1
mnz-12b	0.0773	0.00082	0.18695	0.00305	1.99132	0.03254	98	1129	20.89	1104.8	16.55	1112.6	11.04
mnz-1a2	0.07758	0.00083	0.17834	0.00292	1.90651	0.03132	93	1136.2	21.07	1057.9	15.98	1083.4	10.94
mnz-7b	0.07761	0.00088	0.18766	0.00306	2.00683	0.03359	98	1136.9	22.43	1108.7	16.61	1117.8	11.34
mnz-13c	0.07769	0.00082	0.18614	0.00304	1.99249	0.03261	97	1138.9	20.95	1100.4	16.5	1113	11.06
mnz-13b	0.07781	0.00082	0.18596	0.00303	1.99357	0.03251	96	1141.9	20.75	1099.4	16.47	1113.3	11.03
mnz-14b	0.07783	0.00085	0.18606	0.00304	1.99527	0.03298	96	1142.5	21.5	1100	16.52	1113.9	11.18
mnz-6b	0.07794	0.00085	0.18384	0.003	1.97431	0.03262	95	1145.3	21.61	1087.9	16.31	1106.8	11.14
mnz-9a	0.07809	0.00091	0.18463	0.00301	1.98658	0.03356	95	1149.2	22.97	1092.2	16.39	1111	11.41
mnz-20a	0.07809	0.00086	0.18878	0.00306	2.03149	0.03336	97	1149.2	21.81	1114.8	16.58	1126.1	11.17
mnz-6a	0.07814	0.00088	0.18018	0.00294	1.94001	0.03237	93	1150.4	22.1	1068	16.08	1095	11.18
mnz-7a	0.07831	0.0009	0.19102	0.00312	2.06103	0.03472	98	1154.7	22.68	1126.9	16.89	1136	11.52
mnz-14a	0.07833	0.00091	0.1798	0.00295	1.94054	0.03285	92	1155.3	22.78	1065.9	16.12	1095.2	11.34
mnz-3b	0.07861	0.00083	0.18322	0.003	1.98474	0.03249	93	1162.4	20.74	1084.6	16.33	1110.3	11.05
mnz-5a	0.07862	0.00084	0.19213	0.00313	2.08133	0.03411	97	1162.5	20.99	1132.9	16.95	1142.7	11.24
RED2011-01													
MNZ-4a	0.07673	0.00086	0.18281	0.00245	1.93286	0.02716	97	1114.2	22.25	1082.3	13.34	1092.5	9.4
MNZ-12a	0.07702	0.00087	0.19937	0.00287	2.11639	0.03167	104	1121.6	22.27	1171.9	15.43	1154.2	10.32
MNZ-9b	0.07726	0.00083	0.19073	0.00271	2.03103	0.02952	100	1127.9	21.34	1125.3	14.65	1126	9.89
MNZ-6a	0.07732	0.00086	0.1924	0.00262	2.05	0.02916	100	1129.4	21.97	1134.4	14.18	1132.3	9.71
MNZ-5a	0.07734	0.00088	0.18583	0.00252	1.98037	0.02835	97	1129.9	22.59	1098.7	13.68	1108.8	9.66
MNZ-10b	0.07735	0.00087	0.19139	0.00274	2.04047	0.03036	100	1130.2	22.22	1128.9	14.81	1129.1	10.14
MNZ-10a	0.07735	0.00086	0.18989	0.00271	2.02451	0.02985	99	1130.3	21.89	1120.8	14.66	1123.8	10.02
MNZ-2b	0.07742	0.00086	0.18745	0.00247	1.99979	0.02748	98	1132	21.85	1107.5	13.41	1115.4	9.3
MNZ-5b	0.07752	0.00089	0.18493	0.00252	1.97556	0.0285	96	1134.5	22.86	1093.9	13.7	1107.2	9.72
MNZ-9a	0.07761	0.00081	0.19191	0.00271	2.05291	0.02937	100	1137	20.72	1131.7	14.65	1133.3	9.77
MNZ-2a	0.07762	0.00084	0.18498	0.00242	1.97851	0.02668	96	1137.1	21.3	1094.1	13.17	1108.2	9.1
MNZ-4b	0.0778	0.00085	0.1912	0.00257	2.04984	0.02853	99	1141.8	21.61	1127.9	13.88	1132.2	9.5
MNZ-3a	0.07781	0.00088	0.1885	0.0025	2.02115	0.02823	97	1142.1	22.28	1113.2	13.57	1122.6	9.49

MNZ-11b	0.07811	0.00082	0.19254	0.00275	2.07296	0.02995	99	1149.7	20.71	1135.1	14.86	1139.9	9.9
MNZ-11a	0.07848	0.00083	0.19309	0.00275	2.08873	0.03031	98	1159.1	20.95	1138.1	14.88	1145.1	9.96
MNZ-3b	0.07852	0.00092	0.1889	0.00253	2.04392	0.02923	96	1160.1	22.97	1115.4	13.71	1130.3	9.75
MNZ-7a	0.07875	0.00085	0.19958	0.00281	2.166	0.03132	101	1165.8	21.32	1173.1	15.08	1170.2	10.05
MNZ-8b	0.07923	0.00099	0.1929	0.00277	2.10651	0.03295	97	1178	24.52	1137	14.95	1150.9	10.77
MNZ-8a	0.0794	0.00091	0.1926	0.00273	2.10755	0.03149	96	1182.1	22.59	1135.4	14.76	1151.3	10.29

Concordance= ($^{206}Pb/^{238}U$) / ($^{207}Pb/^{206}Pb$)

*- discounted from weighted average age calculations

Appendix 4- U-Pb zircon data

Analysis	Ratios								Concordancy	Apparent ages							
	$^{207}Pb/^{206}Pb$	1σ	$^{206}Pb/^{238}U$	1σ	$^{207}Pb/^{235}U$	1σ	$^{208}Pb/^{232}Th$	1σ		$^{207}Pb/^{206}Pb$	1σ	$^{206}Pb/^{238}U$	1σ	$^{207}Pb/^{235}U$	1σ	$^{208}Pb/^{232}Th$	1σ
Zircon Data																	
AS2010-64J																	
ZR-1	0.10255	0.00105	0.28448	0.00358	4.02161	0.05081	0.07832	0.00072	97	1670.8	18.9	1613.9	17.97	1638.6	10.27	1524.1	13.48
ZR-10	0.10297	0.00104	0.27517	0.00335	3.90561	0.04728	0.07724	0.00069	93	1678.4	18.46	1567	16.91	1614.8	9.79	1503.9	12.98
ZR-11	0.10201	0.00115	0.28146	0.00351	3.95755	0.05173	0.07357	0.00084	96	1661.1	20.68	1598.7	17.64	1625.5	10.59	1434.8	15.88
ZR-13	0.10162	0.00113	0.28785	0.00371	4.03214	0.05401	0.08264	0.00088	99	1653.9	20.38	1630.8	18.59	1640.7	10.9	1604.8	16.42
ZR-14	0.10067	0.00116	0.29256	0.00361	4.05961	0.05338	0.08109	0.00088	101	1636.5	21.27	1654.3	17.99	1646.2	10.71	1576	16.37
ZR-15	0.10138	0.00111	0.27874	0.00353	3.89525	0.05106	0.07754	0.0008	96	1649.6	20.19	1585	17.8	1612.7	10.59	1509.5	14.99
ZR-17	0.10064	0.00111	0.28247	0.00368	3.91876	0.05288	0.07677	0.00082	98	1635.9	20.32	1603.8	18.51	1617.6	10.92	1495	15.37
ZR-18	0.10089	0.0011	0.29223	0.0038	4.06404	0.0545	0.07711	0.00081	101	1640.5	20.14	1652.7	18.96	1647.1	10.93	1501.3	15.26
ZR-19	0.10166	0.00106	0.28766	0.00359	4.0315	0.05099	0.0795	0.00074	98	1654.7	19.16	1629.8	17.97	1640.6	10.29	1546.1	13.94
ZR-2	0.10024	0.00105	0.28752	0.00359	3.97312	0.05032	0.08309	0.00082	100	1628.6	19.37	1629.1	17.96	1628.7	10.27	1613.4	15.26
ZR-21	0.10133	0.0011	0.29072	0.00369	4.06119	0.05318	0.07784	0.00078	100	1648.7	19.99	1645.1	18.43	1646.5	10.67	1515.2	14.7
ZR-22	0.10161	0.00105	0.28584	0.00358	4.00373	0.05072	0.07859	0.00074	98	1653.7	19.06	1620.7	17.96	1635	10.29	1529.2	13.88
ZR-23	0.10149	0.00106	0.28564	0.00357	3.99653	0.05061	0.07565	0.00071	98	1651.6	19.19	1619.7	17.89	1633.5	10.28	1474	13.33
ZR-24	0.10137	0.00107	0.27998	0.00353	3.91244	0.05022	0.06935	0.00065	96	1649.3	19.4	1591.2	17.78	1616.3	10.38	1355.2	12.34
ZR-26	0.10364	0.00114	0.28201	0.00351	4.02908	0.05217	0.08185	0.00085	95	1690.3	20.15	1601.5	17.65	1640.1	10.53	1590.1	15.85
ZR-27	0.10138	0.00105	0.28873	0.00356	4.03542	0.05042	0.08087	0.00076	99	1649.6	19.09	1635.2	17.83	1641.4	10.17	1571.8	14.22
ZR-3	0.0985	0.0011	0.2741	0.00349	3.72188	0.0495	0.07789	0.00088	98	1595.8	20.76	1561.6	17.65	1576.1	10.64	1515.9	16.46
ZR-30	0.10064	0.00122	0.28292	0.00367	3.92477	0.05528	0.08026	0.00094	98	1636	22.35	1606.1	18.46	1618.8	11.4	1560.4	17.61
ZR-31	0.10007	0.00108	0.28814	0.00366	3.97479	0.0519	0.08239	0.0009	100	1625.4	19.91	1632.2	18.34	1629.1	10.59	1600.2	16.72
ZR-33	0.09979	0.00122	0.27462	0.0036	3.77652	0.05372	0.07563	0.0011	97	1620.3	22.58	1564.2	18.22	1587.8	11.42	1473.6	20.64
ZR-34	0.1019	0.00111	0.28368	0.00359	3.98478	0.0519	0.07826	0.00083	97	1658.9	19.95	1609.9	18.01	1631.1	10.57	1522.9	15.52
ZR-35	0.10007	0.00104	0.28541	0.0036	3.93706	0.0501	0.0787	0.00083	100	1625.3	19.12	1618.6	18.05	1621.3	10.3	1531.2	15.5
ZR-37	0.10023	0.00109	0.28772	0.00379	3.97424	0.05375	0.07365	0.00083	100	1628.3	20.04	1630.1	19	1629	10.97	1436.3	15.57
ZR-38	0.10258	0.00115	0.27591	0.00355	3.90156	0.05233	0.08006	0.00095	94	1671.4	20.56	1570.7	17.91	1614	10.84	1556.6	17.81
ZR-39	0.10321	0.00108	0.28387	0.00378	4.03735	0.05421	0.07171	0.00076	96	1682.6	19.18	1610.8	18.98	1641.8	10.93	1399.9	14.28
ZR-40a	0.10256	0.00109	0.27877	0.0036	3.94059	0.05174	0.07863	0.00087	95	1671	19.46	1585.2	18.14	1622.1	10.63	1529.9	16.27
ZR-40b	0.10107	0.00106	0.28067	0.00348	3.90888	0.04915	0.07338	0.00067	97	1643.9	19.38	1594.8	17.5	1615.5	10.17	1431.2	12.69
ZR-41	0.10145	0.00112	0.28142	0.00352	3.93399	0.051	0.07267	0.00074	97	1650.8	20.26	1598.5	17.71	1620.7	10.5	1417.9	13.92
ZR-42	0.10039	0.00105	0.28058	0.00349	3.88149	0.04894	0.07316	0.00068	98	1631.4	19.34	1594.3	17.58	1609.8	10.18	1427.1	12.78
ZR-43	0.09964	0.00107	0.27154	0.0034	3.72835	0.04786	0.07245	0.00069	96	1617.3	19.89	1548.6	17.24	1577.5	10.28	1413.7	12.95
ZR-44	0.10037	0.00104	0.28236	0.00353	3.90577	0.04925	0.07419	0.00068	98	1631	19.2	1603.2	17.73	1614.9	10.19	1446.5	12.79
ZR-45	0.10209	0.00106	0.27956	0.0035	3.93335	0.04978	0.07541	0.00069	96	1662.5	19.17	1589.1	17.65	1620.6	10.25	1469.5	12.94
ZR-46	0.10211	0.00104	0.28035	0.00351	3.94539	0.04936	0.07633	0.00069	96	1662.9	18.72	1593.1	17.67	1623	10.14	1486.7	13.04
ZR-48	0.0993	0.00108	0.27536	0.0035	3.7688	0.04931	0.07194	0.00073	97	1611	20.16	1568	17.68	1586.1	10.5	1404.1	13.69
ZR-49	0.10127	0.00111	0.28093	0.00358	3.92138	0.05161	0.0753	0.00073	97	1647.5	20.19	1596	18.02	1618.1	10.65	1467.4	13.64
ZR-5	0.10281	0.00109	0.28816	0.00363	4.08418	0.05246	0.08536	0.0009	97	1675.4	19.44	1632.3	18.18	1651.1	10.48	1655.7	16.79
ZR-52	0.10014	0.00107	0.27823	0.00357	3.84068	0.05017	0.07945	0.00079	97	1626.6	19.71	1582.4	18	1601.3	10.52	1545.3	14.83
ZR-53	0.09871	0.00119	0.26879	0.00351	3.65759	0.05144	0.07407	0.00097	96	1599.9	22.3	1534.7	17.85	1562.2	11.21	1444.2	18.23
ZR-54	0.10129	0.00112	0.2811	0.00363	3.9253	0.05242	0.07952	0.00084	97	1647.9	20.39	1596.9	18.26	1618.9	10.81	1546.6	15.74
ZR-55	0.10119	0.00109	0.277	0.00356	3.86402	0.05079	0.07489	0.00077	96	1646	19.86	1576.2	17.98	1606.2	10.6	1459.7	14.42
ZR-57	0.10137	0.00107	0.28545	0.00366	3.9893	0.05172	0.0792	0.00079	98	1649.4	19.37	1618.7	18.36	1632	10.53	1540.6	14.77
ZR-58	0.10054	0.00105	0.28666	0.00367	3.97306	0.05134	0.07835	0.00079	99	1634	19.29	1624.8	18.41	1628.7	10.48	1524.7	14.79

ZR-59	0.10123	0.00112	0.2847	0.00368	3.97304	0.05318	0.0774	0.00087	98	1646.7	20.45	1615	18.47	1628.7	10.86	1506.9	16.33
ZR-6-1	0.10027	0.00104	0.28473	0.00362	3.93617	0.05062	0.07489	0.00071	99	1629.2	19.24	1615.1	18.19	1621.2	10.41	1459.7	13.33
ZR-6-2	0.10313	0.00111	0.28306	0.00359	4.02459	0.0524	0.08181	0.00084	96	1681.2	19.77	1606.8	18.02	1639.2	10.59	1589.4	15.68
ZR-7-1	0.10103	0.00113	0.28335	0.0036	3.94684	0.05242	0.08215	0.00092	98	1643.1	20.62	1608.2	18.07	1623.3	10.76	1595.8	17.21
ZR-7-2	0.09956	0.00113	0.27176	0.00345	3.73051	0.04992	0.06875	0.00081	96	1615.9	20.94	1549.7	17.51	1577.9	10.72	1343.9	15.33
ZR-9	0.10059	0.00111	0.29359	0.00381	4.0713	0.05466	0.08326	0.0009	101	1635.1	20.42	1659.4	18.97	1648.6	10.95	1616.4	16.73
COL2011-01																	
ZR-17	0.09929	0.00112	0.28434	0.00357	3.89176	0.05128	0.08071	0.00099	100	1610.8	20.78	1613.2	17.92	1612	10.64	1568.9	18.44
ZR-10	0.09938	0.00111	0.28299	0.00353	3.87658	0.05069	0.0801	0.00089	100	1612.5	20.75	1606.4	17.73	1608.8	10.55	1557.4	16.57
ZR-52	0.09941	0.00106	0.28487	0.00363	3.90434	0.05061	0.0779	0.00132	100	1613.1	19.7	1615.9	18.22	1614.6	10.48	1516.2	24.8
ZR-48	0.09954	0.00111	0.28834	0.00369	3.95767	0.05271	0.07968	0.00112	101	1615.5	20.59	1633.2	18.47	1625.6	10.8	1549.5	20.88
ZR-50	0.09975	0.00128	0.28056	0.00368	3.85881	0.05626	0.07886	0.00129	98	1619.3	23.65	1594.2	18.55	1605.1	11.76	1534.3	24.14
ZR-12	0.09982	0.00117	0.2884	0.00364	3.96846	0.05353	0.08445	0.00114	101	1620.8	21.6	1633.5	18.2	1627.8	10.94	1638.7	21.18
ZR-55	0.09985	0.00111	0.28401	0.00365	3.90903	0.052	0.07854	0.0014	99	1621.3	20.6	1611.5	18.31	1615.6	10.76	1528.1	26.25
ZR-19	0.09992	0.00116	0.2886	0.00365	3.97521	0.05351	0.08424	0.00108	101	1622.5	21.41	1634.5	18.24	1629.1	10.92	1634.7	20.14
ZR-20	0.09992	0.00114	0.28616	0.00361	3.94173	0.0525	0.08245	0.00102	100	1622.6	21.05	1622.3	18.07	1622.3	10.79	1601.4	19
ZR-31	0.09997	0.0011	0.28538	0.0036	3.93299	0.05156	0.08112	0.00106	100	1623.4	20.33	1618.4	18.07	1620.5	10.61	1576.5	19.85
ZR-56	0.10005	0.00109	0.28494	0.00365	3.92946	0.0515	0.08057	0.00141	99	1625	20.11	1616.2	18.29	1619.8	10.61	1566.2	26.33
ZR-14	0.10005	0.0011	0.28747	0.00359	3.96469	0.05145	0.08515	0.001	100	1625	20.31	1628.9	17.99	1627	10.52	1651.7	18.68
ZR-27	0.10013	0.00106	0.28629	0.00358	3.95202	0.05063	0.08331	0.00101	100	1626.5	19.65	1623	17.96	1624.4	10.38	1617.5	18.88
ZR-60	0.1002	0.00106	0.28521	0.00364	3.93814	0.05073	0.08087	0.00139	99	1627.8	19.6	1617.6	18.24	1621.6	10.43	1571.8	26.03
ZR-51	0.10022	0.00104	0.28628	0.00364	3.95599	0.05065	0.07872	0.00133	100	1628.3	19.24	1622.9	18.24	1625.2	10.38	1531.5	25.01
ZR-29	0.10037	0.00111	0.28765	0.00362	3.98032	0.05229	0.08226	0.00104	100	1630.9	20.44	1629.8	18.14	1630.2	10.66	1597.8	19.42
ZR-9	0.10037	0.00116	0.28868	0.00362	3.9944	0.05328	0.08195	0.00102	100	1631	21.33	1634.9	18.1	1633.1	10.83	1592	19.05
ZR-25	0.10043	0.00109	0.28775	0.00361	3.98417	0.05154	0.0849	0.00103	100	1632.1	19.96	1630.3	18.07	1631	10.5	1647	19.16
ZR-5	0.10046	0.00107	0.28814	0.00356	3.99087	0.05054	0.08022	0.00084	100	1632.6	19.65	1632.2	17.84	1632.3	10.28	1559.7	15.77
ZR-38	0.10057	0.00118	0.28784	0.00369	3.99053	0.05453	0.085	0.00122	100	1634.6	21.58	1630.7	18.47	1632.3	11.1	1649	22.65
ZR-43	0.1007	0.00112	0.2921	0.00373	4.05531	0.05392	0.08433	0.00118	101	1637	20.55	1652	18.62	1645.4	10.83	1636.3	22.08
ZR-23	0.10072	0.00111	0.28537	0.00359	3.96255	0.05181	0.08269	0.00099	99	1637.4	20.3	1618.4	18	1626.6	10.6	1605.9	18.5
ZR-28	0.10077	0.00106	0.28685	0.00358	3.985	0.05064	0.08236	0.00097	99	1638.3	19.35	1625.8	17.96	1631.1	10.31	1599.7	18.1
ZR-13	0.10081	0.00147	0.29049	0.00383	4.03674	0.06383	0.08344	0.00112	100	1639.1	26.89	1644	19.13	1641.6	12.87	1619.8	20.83
ZR-24	0.10082	0.00114	0.28807	0.00364	4.00383	0.05333	0.0852	0.00107	100	1639.2	20.9	1631.9	18.21	1635	10.82	1652.6	19.86
ZR-57	0.10082	0.0011	0.28846	0.00369	4.0083	0.05255	0.07704	0.0014	100	1639.2	20.1	1633.8	18.47	1635.9	10.65	1500.1	26.19
ZR-1	0.10094	0.00108	0.29102	0.0036	4.05072	0.05151	0.0841	0.00099	100	1641.4	19.74	1646.6	17.99	1644.4	10.36	1632.1	18.52
ZR-36	0.10095	0.00104	0.28771	0.00361	4.00395	0.05069	0.08519	0.00104	99	1641.6	19.07	1630.1	18.09	1635	10.29	1652.5	19.46
ZR-37	0.10095	0.00118	0.28632	0.00367	3.9848	0.05444	0.08518	0.00121	99	1641.7	21.57	1623.1	18.38	1631.1	11.09	1652.3	22.53
ZR-11	0.10105	0.00113	0.29166	0.00365	4.06241	0.05328	0.08343	0.00105	100	1643.4	20.66	1649.8	18.23	1646.8	10.69	1619.6	19.67
ZR-4	0.10111	0.00119	0.29062	0.00366	4.0514	0.05475	0.08418	0.00109	100	1644.5	21.7	1644.6	18.26	1644.6	11.01	1633.7	20.39
ZR-40	0.10155	0.00109	0.29183	0.00369	4.08553	0.05284	0.08664	0.00115	100	1652.7	19.68	1650.7	18.43	1651.4	10.55	1679.4	21.3
ZR-8	0.10163	0.00106	0.29154	0.0036	4.08473	0.05119	0.08262	0.00084	100	1654.2	19.29	1649.2	17.96	1651.3	10.22	1604.5	15.73
ZR-3	0.10182	0.0011	0.29344	0.00364	4.11983	0.0527	0.08664	0.00098	100	1657.6	19.89	1658.7	18.14	1658.2	10.45	1679.4	18.24
ZR-47	0.10198	0.00125	0.29004	0.00377	4.07845	0.05768	0.08391	0.00126	99	1660.5	22.51	1641.7	18.85	1650	11.53	1628.7	23.43
ZR-54	0.10214	0.00112	0.29603	0.00379	4.16826	0.05479	0.08066	0.00142	100	1663.4	20.08	1671.6	18.85	1667.8	10.76	1568	26.57
ZR-18	0.10287	0.00108	0.29272	0.00364	4.15128	0.05247	0.08639	0.00095	99	1676.6	19.26	1655.1	18.15	1664.5	10.34	1674.8	17.59
ZR-41	0.10463	0.0012	0.3021	0.00387	4.35784	0.05881	0.0916	0.00132	100	1707.8	20.9	1701.7	19.18	1704.4	11.14	1771.5	24.39
HAM2011-02																	
ZR-23b	0.07612	0.00077	0.18441	0.00242	1.93527	0.02524	0.0629	0.00111	99	1098.2	20.11	1091	13.18	1093.4	8.73	1232.9	21.04
ZR-2b	0.07638	0.00079	0.18679	0.00242	1.96698	0.02577	0.06083	0.00087	100	1105	20.57	1104	13.17	1104.3	8.82	1193.5	16.51
ZR-23a	0.07678	0.00078	0.18814	0.00247	1.99149	0.02613	0.06652	0.00118	100	1115.4	20.24	1111.3	13.41	1112.6	8.87	1301.7	22.36
ZR-31a	0.07679	0.00079	0.18695	0.00247	1.97947	0.02635	0.06015	0.00078	99	1115.8	20.27	1104.8	13.43	1108.5	8.98	1180.7	14.88

ZR-2	0.07684	0.00078	0.18931	0.00245	2.00542	0.02599	0.06104	0.00076	100	1116.9	20.18	1117.6	13.29	1117.3	8.78	1197.5	14.51
ZR-51b	0.07706	0.0008	0.18382	0.00246	1.95314	0.02643	0.06179	0.00177	97	1122.8	20.68	1087.8	13.41	1099.5	9.09	1211.8	33.73
ZR-51a	0.07706	0.00079	0.1938	0.00259	2.05933	0.02765	0.06126	0.00171	102	1122.9	20.37	1142	13.99	1135.4	9.18	1201.8	32.51
ZR-18a	0.07707	0.00079	0.18825	0.00247	2.00041	0.02641	0.05908	0.00075	99	1123.1	20.35	1111.9	13.37	1115.7	8.94	1160.2	14.38
ZR-44a	0.07709	0.0008	0.19358	0.00258	2.05773	0.0278	0.058	0.00079	102	1123.5	20.43	1140.7	13.93	1134.9	9.23	1139.6	15.13
ZR-8b	0.07709	0.00078	0.19268	0.00252	2.04792	0.02686	0.06119	0.00074	101	1123.6	20.13	1135.9	13.62	1131.6	8.95	1200.3	14.18
ZR-32a	0.07718	0.00078	0.1934	0.00256	2.0579	0.02735	0.06105	0.00077	101	1125.7	20.12	1139.8	13.83	1134.9	9.08	1197.7	14.74
ZR-8a	0.07723	0.00078	0.19499	0.00255	2.0761	0.02722	0.06288	0.00076	102	1127.1	20.12	1148.3	13.75	1140.9	8.99	1232.6	14.5
ZR-47b	0.07723	0.0008	0.19463	0.00259	2.07282	0.02802	0.05877	0.0008	102	1127.2	20.41	1146.4	13.99	1139.9	9.26	1154.4	15.19
ZR-43a	0.0773	0.0008	0.19887	0.00265	2.11974	0.02871	0.06158	0.00086	104	1129	20.52	1169.2	14.26	1155.3	9.34	1207.8	16.28
ZR-33a	0.07737	0.00081	0.19179	0.00255	2.04589	0.02771	0.05834	0.00083	100	1130.7	20.78	1131.1	13.8	1130.9	9.24	1146.1	15.86
ZR-31b	0.07742	0.00079	0.19132	0.00253	2.04218	0.02721	0.0619	0.0008	100	1131.9	20.22	1128.5	13.71	1129.7	9.08	1213.9	15.25
ZR-50a	0.07751	0.00081	0.19445	0.0026	2.07828	0.02808	0.06172	0.00169	101	1134.2	20.6	1145.4	14.01	1141.7	9.26	1210.6	32.1
ZR-43b	0.07753	0.0008	0.19383	0.00258	2.07205	0.02798	0.06049	0.00082	101	1134.6	20.61	1142.1	13.95	1139.6	9.25	1187	15.64
ZR-35b	0.07753	0.0008	0.19636	0.00262	2.09898	0.02827	0.06265	0.00085	102	1134.6	20.54	1155.7	14.1	1148.5	9.26	1228.2	16.09
ZR-35a	0.07756	0.0008	0.19613	0.00261	2.09744	0.02827	0.06304	0.00086	102	1135.7	20.34	1154.5	14.09	1148	9.27	1235.7	16.44
ZR-30a	0.07757	0.0008	0.18865	0.00249	2.01763	0.02694	0.06014	0.00082	98	1135.8	20.38	1114.1	13.53	1121.5	9.07	1180.5	15.71
ZR-44b	0.07779	0.0008	0.19439	0.00259	2.08503	0.02817	0.05755	0.00078	100	1141.4	20.37	1145.1	13.98	1143.9	9.27	1131	14.96
ZR-34b	0.07782	0.00079	0.19862	0.00264	2.13095	0.02853	0.06431	0.00085	102	1142.2	20.06	1167.9	14.22	1158.9	9.25	1259.8	16.1
ZR-47a	0.0779	0.0008	0.19344	0.00258	2.07792	0.02807	0.0593	0.0008	100	1144.4	20.34	1140	13.92	1141.5	9.26	1164.5	15.32
ZR-34a	0.07792	0.00079	0.19611	0.00261	2.10687	0.02819	0.06769	0.00089	101	1144.9	20.03	1154.4	14.07	1151.1	9.21	1323.8	16.8
ZR-25a	0.07799	0.00081	0.18633	0.00246	2.00366	0.0269	0.06416	0.00087	96	1146.6	20.61	1101.5	13.39	1116.8	9.09	1256.9	16.47
ZR-6b	0.07803	0.00085	0.19034	0.00249	2.04765	0.02778	0.08204	0.00149	98	1147.7	21.6	1123.2	13.5	1131.5	9.26	1593.6	27.89
ZR-30b	0.07808	0.00081	0.1883	0.00249	2.02723	0.0271	0.06388	0.00087	97	1149	20.36	1112.2	13.52	1124.7	9.09	1251.6	16.47
ZR-1b	0.07845	0.00079	0.19442	0.00251	2.10287	0.02713	0.08989	0.00104	99	1158.3	19.91	1145.3	13.57	1149.7	8.88	1739.8	19.29
ZR-18b *	0.0789	0.00082	0.18929	0.00248	2.05908	0.02729	0.07147	0.00092	96	1169.5	20.36	1117.5	13.45	1135.3	9.06	1395.3	17.4
ZR-19b *	0.07958	0.00081	0.19527	0.00256	2.14262	0.02821	0.07809	0.00095	97	1186.7	20.04	1149.8	13.79	1162.7	9.11	1519.7	17.88
ZR-50b *	0.07985	0.00084	0.19274	0.00258	2.12215	0.02875	0.07834	0.00218	95	1193.2	20.5	1136.2	13.93	1156	9.35	1524.4	40.87
ZR-33b *	0.07998	0.00083	0.19945	0.00265	2.19948	0.0296	0.05923	0.00078	98	1196.5	20.3	1172.4	14.25	1180.9	9.39	1163.1	14.9
HAM2011-08																	
ZR-30	0.07676	0.00078	0.1913	0.00242	2.02407	0.02557	0.06469	0.00086	101	1114.9	19.83	1128.4	13.09	1123.6	8.59	1266.9	16.26
ZR-34	0.07736	0.00077	0.19156	0.00243	2.04289	0.02564	0.06976	0.00094	100	1130.4	19.75	1129.8	13.12	1129.9	8.56	1363	17.83
ZR-42	0.07795	0.0008	0.18819	0.00238	2.02266	0.02577	0.05427	0.00094	97	1145.6	20.35	1111.6	12.92	1123.2	8.66	1068.1	18.05
ZR-50	0.07866	0.00078	0.19406	0.00244	2.10441	0.02619	0.07907	0.00126	98	1163.6	19.62	1143.3	13.15	1150.2	8.56	1538.2	23.62
ZR-41	0.09905	0.00109	0.28252	0.00362	3.85855	0.05111	0.07307	0.00121	100	1606.3	20.39	1604	18.18	1605.1	10.68	1425.5	22.71
ZR-45	0.09913	0.00103	0.27365	0.00347	3.7403	0.04784	0.07241	0.00116	97	1607.9	19.28	1559.3	17.55	1580	10.25	1413	21.79
ZR-15	0.09918	0.001	0.28479	0.00357	3.89377	0.04875	0.06665	0.00069	100	1608.7	18.71	1615.4	17.92	1612.4	10.11	1304.1	13.12
ZR-25	0.09923	0.001	0.28966	0.00364	3.96243	0.04958	0.07631	0.00086	102	1609.7	18.61	1639.8	18.19	1626.5	10.14	1486.5	16.16
ZR-33	0.09926	0.00099	0.28562	0.00362	3.90853	0.04902	0.07636	0.00101	101	1610.3	18.46	1619.6	18.14	1615.4	10.14	1487.4	18.96
ZR-18	0.09937	0.00111	0.28579	0.00363	3.91541	0.0519	0.07372	0.0009	101	1612.4	20.57	1620.5	18.22	1616.9	10.72	1437.7	16.89
ZR-28	0.09941	0.00104	0.28581	0.00362	3.91686	0.05018	0.07657	0.00093	100	1613.2	19.3	1620.6	18.16	1617.2	10.36	1491.3	17.52
ZR-16	0.09968	0.001	0.28807	0.00361	3.95863	0.04939	0.07719	0.0008	101	1618.1	18.57	1631.9	18.07	1625.8	10.11	1502.8	14.96
ZR-5	0.09972	0.00108	0.28364	0.00351	3.89871	0.04967	0.05274	0.00057	99	1618.8	19.95	1609.7	17.62	1613.4	10.3	1038.8	10.92
ZR-31	0.09977	0.00107	0.28539	0.00365	3.92538	0.05136	0.08217	0.00117	100	1619.9	19.85	1618.5	18.32	1618.9	10.59	1596.2	21.94
ZR-7	0.10003	0.00123	0.28574	0.00364	3.94011	0.05505	0.07563	0.00093	100	1624.7	22.77	1620.2	18.23	1622	11.32	1473.5	17.41
ZR-36	0.10004	0.00101	0.28	0.00355	3.8618	0.04875	0.07743	0.00103	98	1624.8	18.66	1591.4	17.89	1605.7	10.18	1507.4	19.32
ZR-44	0.10013	0.00115	0.27834	0.00358	3.84253	0.05204	0.07237	0.00123	97	1626.5	21.13	1583	18.04	1601.7	10.91	1412.2	23.24
ZR-8	0.10017	0.00114	0.28154	0.00354	3.88787	0.05165	0.07223	0.00083	98	1627.3	21.04	1599.1	17.82	1611.2	10.73	1409.7	15.62
ZR-3	0.10023	0.00103	0.28469	0.00348	3.93308	0.04832	0.07242	0.00068	99	1628.3	18.95	1615	17.45	1620.5	9.95	1413.1	12.9
ZR-26	0.10025	0.00102	0.28536	0.00359	3.94389	0.04966	0.07958	0.00091	99	1628.8	18.75	1618.3	18.03	1622.7	10.2	1547.6	17.05

ZR-9	0.10025	0.00102	0.28507	0.00354	3.9397	0.04884	0.07604	0.00074	99	1628.8	18.74	1616.8	17.73	1621.9	10.04	1481.3	13.89
ZR-24	0.10027	0.00101	0.28721	0.00361	3.97031	0.04963	0.07469	0.00083	100	1629.2	18.56	1627.6	18.05	1628.1	10.14	1456	15.64
ZR-22	0.10031	0.00102	0.28647	0.00359	3.9615	0.04974	0.06924	0.00077	100	1629.8	18.76	1623.9	18	1626.3	10.18	1353.2	14.48
ZR-48	0.10031	0.00104	0.28505	0.0036	3.94196	0.05011	0.07178	0.00116	99	1629.8	19.08	1616.8	18.07	1622.3	10.3	1401.1	21.87
ZR-4	0.10047	0.00101	0.28672	0.0035	3.97056	0.04834	0.07677	0.00071	100	1632.7	18.57	1625.1	17.54	1628.2	9.88	1495.1	13.41
ZR-19	0.10053	0.00103	0.28607	0.0036	3.96504	0.05012	0.08306	0.00089	99	1634	18.95	1621.9	18.03	1627.1	10.25	1612.7	16.59
ZR-13	0.10067	0.00107	0.28847	0.00364	4.0035	0.05155	0.07626	0.00085	100	1636.5	19.57	1633.9	18.22	1634.9	10.46	1485.4	15.94
ZR-12	0.10085	0.00102	0.2891	0.00363	4.01924	0.05041	0.0745	0.00078	100	1639.8	18.71	1637	18.14	1638.1	10.2	1452.4	14.64
ZR-1	0.10093	0.00118	0.28906	0.00359	4.02118	0.05361	0.0764	0.00085	100	1641.3	21.6	1636.8	17.94	1638.5	10.84	1488.1	15.92
ZR-6	0.10103	0.00102	0.28445	0.00349	3.96121	0.04855	0.07795	0.00073	98	1643	18.59	1613.7	17.54	1626.3	9.94	1517.1	13.78
ZR-10	0.10152	0.00127	0.292	0.00376	4.08651	0.05808	0.07865	0.00098	100	1652.1	23.05	1651.5	18.74	1651.6	11.59	1530.3	18.34
ZR-21	0.1024	0.00123	0.29715	0.00382	4.19498	0.05845	0.09359	0.00122	101	1668.1	22.12	1677.1	19	1673	11.42	1808.3	22.6
ZR-38 *	0.08434	0.00085	0.21937	0.00278	2.55077	0.03212	0.07629	0.00108	98	1300.3	19.41	1278.5	14.69	1286.7	9.18	1486.1	20.36
ZR-39*	0.08655	0.00087	0.22165	0.00281	2.64505	0.03331	0.07725	0.00107	96	1350.5	19.13	1290.6	14.82	1313.3	9.28	1504	19.99
ZR-43 *	0.09388	0.00094	0.23833	0.00301	3.08506	0.03869	0.0683	0.00108	92	1505.7	18.84	1378	15.66	1429	9.62	1335.4	20.34
ZR-20 *	0.10724	0.00123	0.28468	0.00364	4.20883	0.05693	0.06096	0.00074	92	1753	20.82	1614.9	18.29	1675.7	11.1	1196.1	14.11
AS2010-62D																	
Zr-32	0.09827	0.00102	0.27258	0.00371	3.69273	0.05059	0.07562	0.00101	98	1591.5	19.27	1553.9	18.77	1569.8	10.95	1473.4	18.95
Zr-39	0.10027	0.00101	0.28168	0.00349	3.89372	0.04798	0.07405	0.00073	98	1629.2	18.63	1599.8	17.56	1612.4	9.96	1443.9	13.82
Zr-41	0.10128	0.00105	0.27821	0.00348	3.88439	0.04888	0.09958	0.00242	96	1647.7	19.08	1582.3	17.55	1610.4	10.16	1918.6	44.41
Zr-5	0.10234	0.00106	0.28118	0.0036	3.96722	0.05088	0.08051	0.00081	96	1667.1	19	1597.3	18.11	1627.5	10.4	1565.1	15.14
Zr-9	0.10346	0.00106	0.28561	0.00373	4.07412	0.05291	0.08997	0.00198	96	1687	18.7	1619.5	18.7	1649.1	10.59	1741.4	36.62
Zr-65	0.10494	0.00113	0.28884	0.0038	4.17958	0.05613	0.10352	0.00208	95	1713.3	19.72	1635.7	18.99	1670	11	1991	38.09
Zr-80	0.10589	0.00111	0.30419	0.00398	4.43988	0.05868	0.10969	0.00198	99	1729.9	19.09	1712	19.66	1719.8	10.95	2103.6	36.04
Zr-36	0.10742	0.0011	0.28345	0.0035	4.19727	0.05191	0.11545	0.00214	92	1756.1	18.63	1608.7	17.56	1673.5	10.14	2208.4	38.77
Zr-31	0.10844	0.00122	0.30115	0.00412	4.50115	0.06383	0.07892	0.00096	96	1773.4	20.48	1697	20.41	1731.2	11.78	1535.4	18.02
Zr-78	0.10897	0.00115	0.30056	0.00393	4.51441	0.05981	0.10771	0.00155	95	1782.2	19.1	1694.1	19.49	1733.6	11.01	2067.6	28.25
Zr-73	0.10899	0.00126	0.30895	0.00411	4.6426	0.06489	0.08093	0.00096	97	1782.6	20.98	1735.5	20.22	1757	11.68	1573	17.9
Zr-72	0.11029	0.00124	0.31013	0.0041	4.71613	0.06484	0.08009	0.00124	97	1804.3	20.31	1741.3	20.19	1770.1	11.52	1557.2	23.22
Zr-70	0.11058	0.00121	0.32345	0.00426	4.9316	0.06662	0.08401	0.00102	100	1809	19.67	1806.5	20.75	1807.7	11.4	1630.4	19.08
Zr-58	0.11086	0.00121	0.33037	0.00434	5.04983	0.06785	0.0914	0.00101	101	1813.6	19.67	1840.2	21.01	1827.7	11.39	1767.8	18.78
Zr-46	0.11096	0.00115	0.31669	0.00405	4.84477	0.06217	0.08305	0.00081	98	1815.3	18.65	1773.5	19.84	1792.7	10.8	1612.6	15.17
Zr-15	0.11105	0.00123	0.32754	0.00443	5.01516	0.06956	0.08581	0.00091	101	1816.7	20.01	1826.5	21.53	1821.9	11.74	1664	16.98
Zr-61	0.11126	0.00129	0.3274	0.00434	5.02262	0.07001	0.08708	0.00099	100	1820.1	20.84	1825.8	21.1	1823.1	11.8	1687.6	18.46
Zr-81	0.11151	0.00159	0.31895	0.00441	4.90247	0.07846	0.08506	0.00131	98	1824.2	25.63	1784.6	21.55	1802.7	13.5	1650	24.36
Zr-30	0.11155	0.0012	0.31757	0.00432	4.88257	0.0676	0.08092	0.00087	97	1824.8	19.46	1777.9	21.12	1799.3	11.67	1572.8	16.27
Zr-33	0.11214	0.00128	0.30953	0.00427	4.78536	0.06892	0.08715	0.00127	95	1834.3	20.55	1738.4	21.04	1782.3	12.1	1688.9	23.58
Zr-83	0.11222	0.00116	0.33177	0.00434	5.13171	0.06751	0.08537	0.00094	101	1835.6	18.66	1847	21	1841.4	11.18	1655.8	17.46
Zr-85	0.11237	0.00121	0.32566	0.00429	5.04382	0.06781	0.08365	0.00094	99	1838	19.4	1817.3	20.84	1826.7	11.39	1623.7	17.46
Zr-84	0.11247	0.00116	0.32327	0.00423	5.0115	0.0659	0.08247	0.0009	98	1839.7	18.63	1805.7	20.6	1821.3	11.13	1601.7	16.74
Zr-6	0.1125	0.00114	0.32365	0.00416	5.02007	0.06399	0.08646	0.00079	98	1840.3	18.23	1807.5	20.24	1822.7	10.79	1676.1	14.67
Zr-55	0.11309	0.00116	0.32664	0.00422	5.0931	0.06559	0.09061	0.00089	99	1849.6	18.37	1822.1	20.5	1835	10.93	1753.1	16.42
Zr-37	0.11349	0.00115	0.32546	0.00401	5.09184	0.06243	0.08609	0.00075	98	1856.1	18.12	1816.3	19.52	1834.7	10.41	1669.3	13.9
Zr-63	0.11362	0.00119	0.32907	0.0043	5.15505	0.06784	0.09331	0.00115	99	1858	18.73	1833.9	20.87	1845.2	11.19	1803	21.34
Zr-51	0.1138	0.00118	0.3326	0.00428	5.21848	0.06739	0.08427	0.0008	99	1861	18.58	1851	20.72	1855.6	11	1635.4	14.91
Zr-64	0.11574	0.0012	0.33557	0.00439	5.35522	0.07037	0.08997	0.00103	99	1891.4	18.58	1865.3	21.18	1877.7	11.24	1741.2	19.17
Zr-59	0.11617	0.00124	0.29679	0.00389	4.75388	0.06312	0.09661	0.00158	88	1898.1	19.07	1675.4	19.32	1776.8	11.14	1864.1	29.05
Zr-52	0.11621	0.00124	0.33197	0.0043	5.31905	0.07	0.09132	0.00092	97	1898.8	19.1	1847.9	20.82	1871.9	11.25	1766.4	17.04
Zr-12	0.11845	0.00124	0.34225	0.00459	5.58944	0.07491	0.0866	0.00113	98	1932.9	18.56	1897.5	22.04	1914.5	11.54	1678.7	20.99
Zr-21	0.11896	0.00132	0.34061	0.00463	5.58655	0.07764	0.08558	0.00093	97	1940.7	19.74	1889.6	22.24	1914	11.97	1659.7	17.33

Zr-35	0.11913	0.00146	0.32278	0.00453	5.30208	0.07953	0.08621	0.00121	93	1943.2	21.75	1803.3	22.06	1869.2	12.81	1671.4	22.5
Zr-75	0.11998	0.00124	0.34613	0.00452	5.72555	0.07503	0.09088	0.00101	98	1955.9	18.33	1916.1	21.66	1935.2	11.33	1758.2	18.64
Zr-26	0.12005	0.00124	0.35033	0.00472	5.79697	0.07803	0.08629	0.00089	99	1956.9	18.3	1936.2	22.55	1946	11.66	1672.9	16.59
Zr-74	0.12089	0.00123	0.35219	0.00459	5.87008	0.07646	0.09181	0.00099	99	1969.4	18.07	1945.1	21.9	1956.8	11.3	1775.3	18.4
Zr-60	0.12105	0.00124	0.34842	0.00453	5.81493	0.07542	0.09682	0.00101	98	1971.7	18.06	1927	21.68	1948.6	11.24	1868	18.55
Zr-69	0.12192	0.00153	0.32113	0.00435	5.39813	0.0791	0.09158	0.00139	90	1984.5	22.14	1795.2	21.21	1884.6	12.55	1771.1	25.79
Zr-43	0.12407	0.00145	0.33343	0.00429	5.70305	0.07741	0.09046	0.00126	92	2015.5	20.54	1855	20.76	1931.8	11.73	1750.4	23.28
Zr-56	0.12518	0.00127	0.36713	0.00476	6.33668	0.08168	0.10169	0.00104	99	2031.4	17.85	2015.9	22.47	2023.5	11.3	1957.5	19.1
Zr-29	0.12523	0.00146	0.29743	0.0041	5.13358	0.07386	0.09526	0.00108	83	2032	20.47	1678.5	20.35	1841.7	12.23	1839.1	19.86
Zr-57	0.12617	0.00135	0.37253	0.00488	6.48025	0.08611	0.10343	0.00127	100	2045.2	18.81	2041.3	22.92	2043.2	11.69	1989.4	23.25
Zr-22	0.12715	0.00134	0.36168	0.00488	6.33934	0.08574	0.08957	0.00085	97	2058.9	18.41	1990.1	23.1	2023.9	11.86	1733.9	15.85
Zr-40	0.12875	0.00131	0.37019	0.00461	6.57062	0.08152	0.0949	0.00086	98	2081	17.77	2030.3	21.7	2055.4	10.93	1832.4	15.87
Zr-68	0.13184	0.00169	0.38517	0.00527	7.00147	0.10426	0.10451	0.00156	99	2122.6	22.32	2100.4	24.5	2111.6	13.23	2009.2	28.58
Zr-27	0.13288	0.00141	0.37829	0.00513	6.92884	0.09481	0.09021	0.00103	97	2136.4	18.48	2068.3	24	2102.4	12.14	1745.7	19.17
Zr-45	0.13324	0.00141	0.34869	0.00444	6.40538	0.08228	0.09583	0.00097	90	2141.2	18.34	1928.4	21.2	2033	11.28	1849.7	17.9
Zr-24	0.14457	0.0016	0.41288	0.00564	8.22775	0.11454	0.10664	0.00122	98	2282.6	18.92	2228.1	25.73	2256.4	12.6	2048	22.33
Zr-19	0.1449	0.00154	0.41758	0.00564	8.34259	0.11307	0.10856	0.0011	98	2286.6	18.16	2249.5	25.66	2269	12.29	2083	20.1
Zr-38	0.14574	0.00155	0.37715	0.00472	7.57717	0.09603	0.10923	0.00111	90	2296.5	18.17	2062.9	22.09	2182.2	11.37	2095.4	20.29
Zr-77	0.14575	0.00155	0.41972	0.00552	8.43198	0.11227	0.10241	0.00125	98	2296.7	18.16	2259.2	25.04	2278.6	12.09	1970.7	22.93
Zr-28	0.14811	0.00158	0.42564	0.00579	8.68941	0.11914	0.1037	0.00108	98	2324.2	18.15	2286	26.18	2306	12.48	1994.3	19.73
Zr-20	0.14854	0.00149	0.43185	0.00578	8.84435	0.11639	0.10994	0.00103	99	2329.2	17.07	2314.1	26.01	2322.1	12.01	2108.3	18.8
Zr-47	0.15186	0.00157	0.4096	0.00526	8.57542	0.11027	0.10384	0.00097	94	2366.9	17.58	2213.1	24.07	2294	11.69	1996.9	17.85
Zr-23	0.15222	0.00151	0.43726	0.00586	9.17541	0.12083	0.11037	0.00099	99	2371.1	16.84	2338.4	26.27	2355.7	12.06	2116	18
Zr-18	0.15284	0.00151	0.42614	0.00569	8.98015	0.11749	0.11263	0.00127	96	2378	16.79	2288.3	25.71	2336	11.95	2157.1	23
Zr-71	0.15373	0.00169	0.39343	0.00522	8.33905	0.11291	0.10778	0.00129	90	2387.8	18.58	2138.7	24.13	2268.6	12.28	2068.8	23.56
Zr-11	0.15436	0.00155	0.40965	0.00547	8.71875	0.11436	0.10482	0.00107	92	2394.8	16.94	2213.3	24.99	2309	11.95	2014.8	19.5
Zr-17	0.15823	0.00175	0.40463	0.00551	8.82735	0.12203	0.10474	0.00121	90	2436.8	18.62	2190.3	25.31	2320.3	12.61	2013.4	22.08
Zr-44	0.1589	0.00161	0.43744	0.00551	9.58272	0.11987	0.10113	0.00091	96	2444	17.03	2339.2	24.72	2395.5	11.5	1947.2	16.62
Zr-66	0.16044	0.00186	0.46209	0.00621	10.22247	0.14272	0.11868	0.00171	100	2460.3	19.42	2448.8	27.4	2455.1	12.91	2266.8	30.81
Zr-2	0.16126	0.00165	0.45037	0.00568	10.0109	0.12574	0.121	0.00107	97	2468.9	17.18	2396.9	25.26	2435.8	11.6	2308.6	19.26
Zr-67	0.16265	0.00167	0.47008	0.00616	10.54219	0.13792	0.1184	0.00125	100	2483.4	17.23	2483.9	27	2483.6	12.13	2261.7	22.62
Zr-42	0.16347	0.00174	0.4563	0.00579	10.28334	0.13185	0.11733	0.00121	97	2491.9	17.86	2423.2	25.62	2460.6	11.87	2242.5	21.82
Zr-16	0.16428	0.00184	0.43682	0.00597	9.89386	0.13748	0.10942	0.00132	93	2500.2	18.69	2336.4	26.79	2424.9	12.81	2098.7	23.99
Zr-82	0.16539	0.00173	0.47017	0.00618	10.7187	0.14158	0.11802	0.00125	99	2511.6	17.49	2484.3	27.09	2499	12.27	2254.9	22.6
Zr-48	0.17132	0.00173	0.46374	0.00594	10.95351	0.13882	0.12253	0.00124	96	2570.6	16.74	2456	26.14	2519.2	11.79	2336.3	22.25
Zr-49	0.17241	0.00173	0.44322	0.00567	10.53502	0.13321	0.12106	0.00116	92	2581.1	16.62	2365	25.34	2483	11.73	2309.8	20.95
Zr-50	0.17818	0.00191	0.51178	0.00667	12.57215	0.16534	0.12158	0.00133	101	2636	17.72	2664.2	28.44	2648.1	12.37	2319.2	24.02
Zr-14	0.18693	0.00195	0.51586	0.00696	13.29552	0.17808	0.12537	0.00157	99	2715.3	17.08	2681.6	29.59	2700.9	12.65	2387.2	28.23
Zr-76	0.18738	0.00187	0.52048	0.00676	13.44285	0.1731	0.13095	0.00132	99	2719.3	16.35	2701.2	28.66	2711.3	12.17	2487.3	23.66
Zr-79	0.18913	0.00204	0.53167	0.00705	13.85998	0.18612	0.12995	0.00148	101	2734.6	17.67	2748.5	29.66	2740.2	12.72	2469.4	26.52
Zr-53	0.19212	0.00193	0.52932	0.00681	14.02062	0.1782	0.13828	0.00133	99	2760.4	16.36	2738.6	28.72	2751.1	12.05	2617.9	23.55
Zr-13	0.20475	0.00205	0.54515	0.00729	15.38995	0.20187	0.13145	0.0013	98	2864.4	16.18	2805	30.4	2839.7	12.51	2496.3	23.18
AS2010-59J																	
ZR-20	0.10503	0.0011	0.30005	0.00382	4.34435	0.05592	0.0885	0.00103	99	1714.9	19.16	1691.5	18.96	1701.8	10.62	1714.1	19.2
ZR-43	0.10569	0.00116	0.28228	0.00373	4.11274	0.05599	0.08027	0.00097	93	1726.3	20.01	1602.8	18.76	1656.8	11.12	1560.6	18.17
ZR-57	0.10684	0.00112	0.31659	0.00419	4.66275	0.06211	0.08155	0.00099	102	1746.2	19	1773	20.52	1760.6	11.14	1584.5	18.56
ZR-11	0.10704	0.00112	0.30076	0.00375	4.43823	0.05604	0.08439	0.0011	97	1749.6	18.97	1695.1	18.59	1719.5	10.46	1637.5	20.58
ZR-37	0.10736	0.00111	0.31437	0.00409	4.65296	0.06093	0.0851	0.00111	100	1755	18.68	1762.2	20.08	1758.8	10.94	1650.7	20.71
ZR-87	0.10751	0.00116	0.31114	0.00371	4.60984	0.05694	0.08655	0.00132	99	1757.6	19.53	1746.3	18.26	1751.1	10.31	1677.8	24.49
ZR-30	0.10755	0.00121	0.30779	0.00402	4.5636	0.06224	0.0842	0.00103	98	1758.3	20.35	1729.8	19.84	1742.6	11.36	1634.1	19.23

ZR-38	0.10803	0.00114	0.29167	0.00381	4.3442	0.05754	0.08416	0.00094	93	1766.5	19.14	1649.9	19.03	1701.8	10.93	1633.3	17.6
ZR-1	0.10856	0.0011	0.31335	0.00378	4.68992	0.05648	0.10068	0.00127	99	1775.3	18.35	1757.2	18.56	1765.4	10.08	1939	23.23
ZR-107	0.1088	0.0012	0.29251	0.00353	4.38685	0.05521	0.08103	0.00131	93	1779.3	20.02	1654.1	17.62	1709.9	10.41	1574.9	24.4
ZR-86	0.10921	0.00113	0.30855	0.00366	4.64404	0.05591	0.09415	0.00279	97	1786.3	18.81	1733.6	18.03	1757.2	10.06	1818.6	51.55
ZR-60	0.10974	0.00114	0.32099	0.00425	4.85597	0.06463	0.08724	0.00114	100	1795.1	18.86	1794.6	20.75	1794.6	11.21	1690.7	21.2
ZR-27	0.10976	0.00112	0.31785	0.00409	4.80951	0.06196	0.08356	0.00103	99	1795.4	18.49	1779.2	20.01	1786.6	10.83	1622.1	19.22
ZR-106	0.10984	0.00118	0.31605	0.0038	4.78521	0.05912	0.08757	0.0014	99	1796.8	19.4	1770.4	18.6	1782.3	10.38	1696.8	26.05
ZR-74	0.10994	0.00124	0.26388	0.00316	3.99843	0.0507	0.07169	0.00099	84	1798.3	20.44	1509.7	16.12	1633.9	10.3	1399.5	18.71
ZR-42	0.11	0.00117	0.31691	0.00417	4.80573	0.06443	0.08423	0.00101	99	1799.3	19.32	1774.6	20.43	1785.9	11.27	1634.5	18.76
ZR-12	0.11012	0.00112	0.31972	0.00398	4.85339	0.06035	0.08472	0.00095	99	1801.3	18.39	1788.3	19.44	1794.2	10.47	1643.7	17.75
ZR-56	0.11049	0.00118	0.32351	0.0043	4.92726	0.06642	0.08519	0.00127	100	1807.4	19.29	1806.8	20.92	1806.9	11.38	1652.4	23.72
ZR-66	0.1106	0.00127	0.3187	0.00378	4.85956	0.06157	0.08664	0.00115	99	1809.4	20.75	1783.4	18.49	1795.3	10.67	1679.4	21.38
ZR-53	0.11081	0.00118	0.31705	0.0042	4.84325	0.06528	0.07794	0.00091	98	1812.8	19.29	1775.3	20.58	1792.4	11.34	1516.9	16.97
ZR-19	0.11096	0.00116	0.31628	0.00402	4.83776	0.06207	0.08153	0.00082	98	1815.1	18.89	1771.6	19.69	1791.5	10.8	1584.1	15.32
ZR-26	0.11101	0.00115	0.32354	0.00417	4.95106	0.06414	0.08265	0.001	100	1815.9	18.64	1807	20.3	1811	10.94	1605.1	18.62
ZR-10	0.11106	0.00114	0.32244	0.00396	4.93621	0.06088	0.0997	0.00115	99	1816.8	18.52	1801.6	19.31	1808.5	10.41	1920.9	21.12
ZR-55	0.11108	0.00115	0.32396	0.00428	4.96075	0.06569	0.08279	0.00099	100	1817.1	18.65	1809.1	20.84	1812.7	11.19	1607.7	18.57
ZR-82	0.11113	0.00124	0.32406	0.0039	4.96251	0.06276	0.08727	0.00118	100	1818	20.16	1809.5	18.98	1813	10.69	1691.2	22
ZR-89	0.11115	0.0012	0.33072	0.00395	5.0666	0.06249	0.08854	0.00117	101	1818.4	19.39	1841.9	19.12	1830.5	10.46	1714.8	21.75
ZR-93	0.11133	0.00129	0.31139	0.00377	4.7781	0.06195	0.08372	0.00139	96	1821.2	20.8	1747.5	18.55	1781.1	10.89	1625	26
ZR-48	0.11145	0.00117	0.32219	0.00425	4.95046	0.06595	0.08517	0.00098	99	1823.2	18.94	1800.4	20.7	1810.9	11.25	1652	18.29
ZR-104	0.11147	0.00115	0.3177	0.00379	4.88117	0.05885	0.086	0.00128	98	1823.5	18.61	1778.5	18.53	1799	10.16	1667.5	23.73
ZR-31	0.11159	0.00115	0.32742	0.00425	5.03738	0.06581	0.0907	0.00102	100	1825.5	18.61	1825.9	20.64	1825.6	11.07	1754.8	18.87
ZR-36	0.11161	0.00114	0.32745	0.00426	5.03851	0.06567	0.08745	0.00091	100	1825.8	18.44	1826	20.68	1825.8	11.04	1694.4	16.92
ZR-15	0.11167	0.00122	0.31029	0.00393	4.77663	0.06223	0.08117	0.0009	95	1826.7	19.62	1742.2	19.35	1780.8	10.94	1577.4	16.89
ZR-47	0.11171	0.00117	0.32393	0.00426	4.98865	0.06627	0.08559	0.00092	99	1827.4	18.85	1808.9	20.76	1817.4	11.24	1659.8	17.12
ZR-70	0.11176	0.00122	0.2894	0.00342	4.45893	0.05478	0.07608	0.00083	90	1828.3	19.67	1638.5	17.09	1723.4	10.19	1482.1	15.6
ZR-59	0.11185	0.00115	0.33211	0.00439	5.12058	0.06764	0.0874	0.00104	101	1829.6	18.5	1848.6	21.25	1839.5	11.22	1693.7	19.32
ZR-101	0.11205	0.00118	0.3312	0.00395	5.11442	0.06233	0.08761	0.00129	101	1832.9	18.89	1844.2	19.15	1838.5	10.35	1697.4	24.06
ZR-71	0.11219	0.00147	0.28556	0.00353	4.41595	0.06216	0.07787	0.00151	88	1835.2	23.52	1619.3	17.69	1715.3	11.65	1515.6	28.32
ZR-108	0.11225	0.00118	0.32623	0.00391	5.04782	0.06154	0.08509	0.00146	99	1836.1	18.92	1820.1	19.01	1827.4	10.33	1650.5	27.24
ZR-14	0.11229	0.0012	0.32592	0.00411	5.04541	0.06483	0.08429	0.00085	99	1836.9	19.21	1818.6	19.98	1827	10.89	1635.7	15.92
ZR-84	0.11232	0.00125	0.32478	0.0039	5.02715	0.06323	0.08631	0.00128	99	1837.3	19.95	1813	18.99	1823.9	10.65	1673.2	23.75
ZR-90	0.11242	0.00121	0.32552	0.00389	5.04394	0.06222	0.08953	0.00124	99	1839	19.35	1816.6	18.9	1826.7	10.45	1733.2	23.09
ZR-25	0.1125	0.0012	0.32866	0.00425	5.09716	0.06726	0.08353	0.00094	100	1840.2	19.24	1831.9	20.64	1835.6	11.2	1621.6	17.59
ZR-94	0.11267	0.00128	0.31632	0.00382	4.91214	0.06314	0.08189	0.00108	96	1842.9	20.48	1771.7	18.72	1804.3	10.84	1591	20.22
ZR-16	0.11335	0.00123	0.31818	0.00404	4.97209	0.06477	0.08196	0.00091	96	1853.9	19.49	1780.8	19.76	1814.6	11.01	1592.3	17.04
ZR-98	0.11366	0.00125	0.32101	0.00385	5.02834	0.06313	0.08718	0.0012	97	1858.7	19.73	1794.7	18.81	1824.1	10.63	1689.5	22.22
ZR-44	0.11383	0.00123	0.32651	0.00431	5.12387	0.06908	0.089	0.001	98	1861.5	19.33	1821.4	20.95	1840.1	11.45	1723.2	18.55
ZR-78	0.11397	0.00121	0.31491	0.00374	4.9462	0.06015	0.07612	0.0008	95	1863.7	19	1764.8	18.31	1810.2	10.27	1482.8	15.04
ZR-29	0.11399	0.00127	0.33033	0.00432	5.19073	0.07041	0.08922	0.00112	99	1863.9	20	1840	20.92	1851.1	11.55	1727.4	20.84
ZR-4	0.11413	0.00119	0.33565	0.0041	5.28102	0.06522	0.08874	0.00087	100	1866.2	18.74	1865.7	19.77	1865.8	10.54	1718.5	16.1
ZR-75	0.11496	0.0015	0.32797	0.00406	5.19672	0.07317	0.08536	0.00144	97	1879.3	23.34	1828.6	19.73	1852.1	11.99	1655.6	26.77
ZR-97	0.115	0.00134	0.31431	0.00382	4.98159	0.06501	0.07758	0.00123	94	1879.9	20.83	1761.9	18.72	1816.2	11.03	1510.3	23.11
ZR-58	0.11507	0.00128	0.32732	0.00438	5.19192	0.07159	0.09196	0.00111	97	1880.9	19.92	1825.4	21.27	1851.3	11.74	1778.1	20.48
ZR-72	0.11514	0.0013	0.29315	0.00351	4.65249	0.05892	0.07961	0.00108	88	1882.1	20.22	1657.3	17.51	1758.7	10.58	1548.2	20.31
ZR-105	0.11548	0.00129	0.31783	0.00385	5.05876	0.06426	0.08465	0.00132	94	1887.3	20	1779.1	18.83	1829.2	10.77	1642.4	24.63
ZR-91	0.11593	0.00123	0.3336	0.00398	5.33039	0.06527	0.08856	0.00132	98	1894.4	18.96	1855.8	19.23	1873.7	10.47	1715.2	24.51
ZR-100	0.11631	0.00124	0.33447	0.004	5.36159	0.06607	0.08829	0.00112	98	1900.3	19.07	1860	19.3	1878.7	10.55	1710.1	20.89
ZR-28	0.11636	0.00158	0.33934	0.00461	5.44321	0.08339	0.09168	0.00156	99	1901	24.15	1883.5	22.17	1891.7	13.14	1773	28.97

ZR-99	0.1168	0.00152	0.32997	0.00412	5.31139	0.0752	0.08524	0.0013	96	1907.8	23.25	1838.2	19.97	1870.7	12.1	1653.4	24.2
ZR-39	0.11706	0.00124	0.3391	0.00444	5.47268	0.0728	0.0898	0.00093	98	1911.9	18.91	1882.3	21.39	1896.3	11.42	1738.2	17.21
ZR-111	0.11724	0.00141	0.29409	0.00363	4.75308	0.06344	0.08601	0.00161	87	1914.5	21.45	1661.9	18.07	1776.7	11.2	1667.7	29.9
ZR-5	0.11779	0.0013	0.33537	0.00414	5.44576	0.06985	0.08875	0.00128	97	1922.9	19.71	1864.3	20.01	1892.1	11	1718.7	23.81
ZR-81	0.11814	0.00138	0.34355	0.00418	5.59231	0.07289	0.09348	0.00121	99	1928.2	20.79	1903.7	20.05	1914.9	11.23	1806.3	22.41
ZR-109	0.11828	0.0014	0.33422	0.0041	5.44957	0.0721	0.08068	0.00159	96	1930.4	21.1	1858.8	19.83	1892.7	11.35	1568.2	29.67
ZR-61	0.11834	0.00125	0.34494	0.004	5.62799	0.06656	0.10138	0.00103	99	1931.3	18.75	1910.4	19.16	1920.4	10.2	1951.7	18.87
ZR-6	0.11925	0.00149	0.34304	0.00436	5.63958	0.07852	0.0968	0.00112	98	1945.1	22.16	1901.3	20.92	1922.2	12.01	1867.5	20.58
ZR-35	0.11989	0.00127	0.34489	0.00451	5.70059	0.07557	0.0929	0.00102	98	1954.6	18.76	1910.2	21.6	1931.5	11.45	1795.6	18.9
ZR-46	0.12004	0.00123	0.35105	0.00461	5.80957	0.07631	0.09045	0.00098	99	1956.9	18.19	1939.6	21.98	1947.8	11.38	1750.2	18.14
ZR-68	0.12005	0.00128	0.29397	0.00345	4.86501	0.05846	0.07097	0.00111	85	1956.9	18.85	1661.3	17.17	1796.2	10.12	1385.9	20.92
ZR-110	0.12018	0.00131	0.34075	0.00412	5.64524	0.07061	0.0908	0.00152	96	1958.9	19.34	1890.3	19.82	1923	10.79	1756.6	28.26
ZR-13	0.12161	0.00124	0.3545	0.00443	5.94323	0.07414	0.09537	0.00101	99	1980	18.08	1956	21.07	1967.6	10.84	1841.2	18.6
ZR-33	0.12193	0.00128	0.37839	0.00493	6.36068	0.08389	0.10359	0.00127	104	1984.6	18.58	2068.8	23.07	2026.9	11.57	1992.2	23.3
ZR-73	0.12339	0.00156	0.33517	0.00413	5.70024	0.07834	0.08609	0.00151	93	2005.8	22.31	1863.4	19.95	1931.4	11.87	1669.2	28.03
ZR-7	0.12581	0.00133	0.37002	0.00456	6.41757	0.08037	0.10977	0.00115	99	2040.3	18.64	2029.5	21.44	2034.7	11	2105.2	20.87
ZR-88	0.12692	0.00166	0.3695	0.00463	6.46336	0.09122	0.09801	0.00163	99	2055.7	22.85	2027.1	21.8	2040.9	12.41	1889.8	30.03
ZR-8	0.12782	0.00143	0.35566	0.00444	6.26686	0.0813	0.11429	0.00183	95	2068.2	19.61	1961.6	21.09	2013.8	11.36	2187.3	33.14
ZR-49	0.12852	0.00135	0.36819	0.00486	6.52343	0.08707	0.09865	0.00111	97	2077.8	18.44	2020.9	22.91	2049.1	11.75	1901.6	20.49
ZR-83	0.12882	0.00146	0.37872	0.00458	6.7229	0.08563	0.10416	0.00138	99	2081.9	19.76	2070.3	21.43	2075.6	11.26	2002.7	25.18
ZR-50	0.12913	0.00134	0.37893	0.00499	6.74542	0.08929	0.09546	0.00103	99	2086.1	18.13	2071.3	23.35	2078.6	11.71	1842.8	18.95
ZR-21	0.13025	0.00174	0.38131	0.00518	6.84613	0.10324	0.09781	0.0015	99	2101.3	23.25	2082.4	24.15	2091.7	13.36	1886.2	27.58
ZR-18	0.13435	0.0014	0.36447	0.00463	6.75024	0.08605	0.09693	0.00106	93	2155.6	18.03	2003.3	21.85	2079.2	11.27	1869.9	19.44
ZR-96	0.13507	0.0018	0.39404	0.00498	7.33562	0.10531	0.09371	0.00179	99	2165	23.01	2141.5	23.04	2153.2	12.83	1810.5	33.09
ZR-69	0.13785	0.00141	0.32041	0.00374	6.08905	0.07137	0.07935	0.00079	81	2200.3	17.63	1791.8	18.24	1988.7	10.22	1543.3	14.75
ZR-17	0.13827	0.00139	0.40566	0.00511	7.73252	0.09666	0.09724	0.00097	100	2205.7	17.38	2195	23.42	2200.4	11.24	1875.6	17.82
ZR-52	0.13938	0.00141	0.40747	0.00537	7.82938	0.10247	0.1041	0.00115	99	2219.5	17.43	2203.3	24.57	2211.6	11.78	2001.6	21.01
ZR-9	0.13965	0.00144	0.36333	0.00446	6.99436	0.0862	0.09686	0.0011	90	2222.9	17.71	1997.9	21.11	2110.7	10.95	1868.7	20.33
ZR-63	0.14141	0.00146	0.41224	0.00478	8.0371	0.09382	0.11489	0.00118	99	2244.6	17.68	2225.2	21.8	2235.2	10.54	2198.2	21.31
ZR-23	0.14257	0.00149	0.4105	0.0053	8.06742	0.10478	0.10469	0.00111	98	2258.6	17.91	2217.2	24.22	2238.6	11.73	2012.4	20.35
ZR-62	0.14352	0.00151	0.41797	0.00486	8.27006	0.09795	0.12317	0.00143	99	2270.1	18.05	2251.3	22.11	2261	10.73	2347.7	25.75
ZR-32	0.14704	0.00154	0.42651	0.00557	8.64606	0.114	0.11922	0.0014	99	2311.8	17.92	2290	25.16	2301.4	12	2276.5	25.33
ZR-34	0.15025	0.00154	0.43631	0.00568	9.03801	0.11792	0.11781	0.00136	99	2348.8	17.47	2334.1	25.5	2341.9	11.93	2251.1	24.56
ZR-95	0.15335	0.00172	0.39618	0.00481	8.37307	0.10636	0.10244	0.00169	90	2383.6	18.99	2151.4	22.2	2272.3	11.52	1971.2	30.93
ZR-24	0.15686	0.00163	0.4529	0.00585	9.79337	0.12693	0.11024	0.00118	99	2422.1	17.52	2408.1	25.95	2415.5	11.94	2113.7	21.53
ZR-85	0.15746	0.00171	0.44865	0.0054	9.73509	0.12051	0.12009	0.00147	98	2428.5	18.29	2389.2	24.03	2410	11.4	2292.3	26.44
ZR-92	0.15792	0.00205	0.38801	0.00492	8.44525	0.11846	0.12246	0.00196	87	2433.5	21.83	2113.6	22.85	2280.1	12.74	2334.9	35.22
ZR-80	0.1602	0.0017	0.45815	0.00546	10.11461	0.12309	0.11958	0.00137	99	2457.8	17.8	2431.4	24.16	2445.3	11.25	2283.1	24.79
ZR-41	0.16228	0.00173	0.46318	0.00613	10.36211	0.13859	0.11824	0.00136	99	2479.5	17.87	2453.6	26.99	2467.7	12.38	2258.9	24.57
ZR-67	0.16335	0.00237	0.46468	0.00609	10.46456	0.15798	0.12082	0.00213	99	2490.7	24.28	2460.2	26.81	2476.8	13.99	2305.5	38.34
ZR-45	0.16529	0.00183	0.40355	0.00539	9.19559	0.12549	0.11709	0.00151	87	2510.5	18.46	2185.4	24.74	2357.7	12.5	2238	27.27
ZR-79	0.16614	0.00173	0.46769	0.00555	10.70803	0.12859	0.12041	0.00125	98	2519.1	17.35	2473.4	24.37	2498.1	11.15	2298.1	22.54
ZR-102	0.17669	0.00188	0.49537	0.00597	12.06322	0.1482	0.12385	0.00186	99	2622.1	17.58	2593.9	25.74	2609.3	11.52	2360	33.44
ZR-65	0.17865	0.00233	0.494	0.00624	12.16672	0.1684	0.13496	0.0018	98	2640.4	21.49	2588	26.93	2617.3	12.99	2558.8	31.98

Concordance= ($^{206}Pb/^{238}U$) / ($^{207}Pb/^{206}Pb$)

*- discounted from weighted average age calculations